

2015-01-01

# Molecular Dynamics Study On Defect Reduction Strategies Towards The Fabrication Of High Performance Cd<sub>1-x</sub>Zn<sub>x</sub>Te/CdS SOLAR CELLS

Jose Juan Chavez

University of Texas at El Paso, jjchavez5@gmail.com

Follow this and additional works at: [https://digitalcommons.utep.edu/open\\_etd](https://digitalcommons.utep.edu/open_etd)



Part of the [Atomic, Molecular and Optical Physics Commons](#), [Electrical and Electronics Commons](#), and the [Nanoscience and Nanotechnology Commons](#)

---

## Recommended Citation

Chavez, Jose Juan, "Molecular Dynamics Study On Defect Reduction Strategies Towards The Fabrication Of High Performance Cd<sub>1-x</sub>Zn<sub>x</sub>Te/CdS SOLAR CELLS" (2015). *Open Access Theses & Dissertations*. 1017.  
[https://digitalcommons.utep.edu/open\\_etd/1017](https://digitalcommons.utep.edu/open_etd/1017)

MOLECULAR DYNAMICS STUDY ON DEFECT REDUCTION  
STRATEGIES TOWARDS THE FABRICATION OF HIGH PERFORMANCE  
 $\text{Cd}_{1-x}\text{Zn}_x\text{Te/CdS}$  SOLAR CELLS

JOSE J. CHAVEZ

Department of Electrical and Computer Engineering

APPROVED:

---

David Zubia, Ph.D., Chair

---

Xiaowang Zhou, Ph.D., Co-Chair

---

José L. Cruz-Campa, Ph.D.

---

Stella Quiñones, Ph.D.

---

John McClure, Ph.D.

---

Charles Ambler, Ph.D.  
Dean of the Graduate School

Copyright ©

by

Jose J. Chavez

2015

## **Dedication**

To my family and friends  
For the relentless support  
That inspired me  
Throughout this journey

MOLECULAR DYNAMICS STUDY ON DEFECT REDUCTION STRATEGIES  
TOWARDS THE FABRICATION OF HIGH PERFORMANCE  
 $\text{Cd}_{1-x}\text{Zn}_x\text{Te}/\text{CdS}$  SOLAR CELLS

by

JOSE J. CHAVEZ, B.S.E.E.

DISSERTATION

Presented to the Faculty of the Graduate School of  
The University of Texas at El Paso  
in Partial Fulfillment  
of the Requirements  
for the Degree of

DOCTOR OF PHILOSOPHY

Department of Electrical and Computer Engineering

THE UNIVERSITY OF TEXAS AT EL PASO

May 2015

## **Acknowledgements**

I would like to thank Dr. David Zubia for serving as my dissertation advisor. I am grateful to Dr. Jose Luis Cruz-Campa, Dr. Xiaowang Zhou, Dr. Stella Quiñones, and Dr. John McClure for their mentoring, guidance, and for serving in my dissertation committee. I thank all my colleagues from the Nanomaterials Integration Laboratory for their unwavering support and for making my doctoral experience fun, enjoyable, and exciting.

I acknowledge the University of Texas System Louis Stokes Alliance for Minority Participation (LSAMP) and the UTEP LSAMP office staff for their financial and professional support in the early years of my doctoral journey. I recognize the financial support provided by the Solar Economy Integrative Graduate Education and Research Traineeship Fellowship and the Department of Energy during the last semesters of my PhD tenure.

I would like to acknowledge the Sandia National Laboratories staff for granting me access to the high performance computing clusters to carry out this work. I also would like to recognize Nito Gumataotao and Dr. Michael McGarry for allowing the use of the Virgo2 cluster. Finally I thank the Extreme Science and Engineering Discovery Environment (XSEDE) and Dr. Patricia Teller for granting me access to computing resources, trainings, and workshops.

## Abstract

Cadmium Telluride is a material widely used in terrestrial thin film photovoltaic applications due to its nearly ideal band gap ( $\sim 1.5$  eV) and high absorption coefficient. Due to its low manufacturing cost, this technology has the potential to become a significant energy resource if higher energy conversion efficiencies are achieved. However, the module efficiencies ( $\sim 14\%$ ) are still far from the theoretical maximum ( $\sim 30\%$ ) for this material in a single junction configuration. The reason behind this low performance is attributed to the high number of defects that are present within the device materials. The physics behind the formation mechanisms of these imperfections and their effect in the electrical the operation of a device is not well understood, and the topic is a focus of a wide variety of studies.

In this work we perform molecular dynamics simulations of epitaxial growth of CdTe on CdS (0001) single crystal substrates in order to exploit the powerful structure prediction capability of high fidelity modelling to capture defect formation mechanisms. In addition, advanced visualization and defect detection software tools are employed to characterize 3-D simulation data and identify, quantify, and index defects within the simulated epilayer with atomic resolution. The combination of accurate modelling and advance characterization software tools creates an analysis capability that provides defect insight beyond the limits offered achievable by means of the experimental characterization equipment in existence. The analysis capability was used to evaluate three CdTe film defect reduction strategies. These approaches were selective area growth, the incorporation of Zn alloying in a buffer layer, and a nano-structure that combined the two previously mentioned methods.

The capability of the defect analysis software was expanded by adding code that enables it to detect defects inside a hexagonal lattice. Previously, the software was only able to detect defects within a diamond lattice. The simulated dislocation density trends observed are in good agreement with experimental data reported in literature and validated the simulation approach. The analysis results showed that selective area growth is an effective strategy in reducing

epilayer defects. The incorporation of the Zn buffer layer was only beneficial at low concentrations ( $<4\%$ ), and detrimental otherwise. The combination of both strategies produced the lowest defect density films in this study.



## Table of Contents

Acknowledgements.....	v
Abstract.....	vi
Table of Contents.....	viii
List of Tables .....	x
List of Figures.....	xi
Chapter 1: Introduction.....	1
1.1 CdTe PV Technology .....	1
1.2 Selective Area Epitaxy.....	5
1.3 Cd <sub>(1-x)</sub> Zn <sub>x</sub> Te Alloying .....	10
1.4 Molecular Dynamics.....	12
1.4 Stillinger-Webber Potential .....	17
1.5 Research Objectives.....	20
Chapter 2: Methodologies.....	22
2.1 Simulation Configuration.....	22
2.2 Post-Processing Analysis Tools.....	31
2.3 Design of Experimental Procedures.....	49
Chapter 3: Results .....	53
3.1 Effect of Deposition Temperature on Defect Density .....	53
3.2 Effect of Island Size on Defect Density.....	71
3.3 Effect of Zn Alloying on Defect Density.....	76

Chapter 4: Conclusions and Summary.....	98
References.....	100
Appendix.....	104
Appendix A: Crystal Analysis Tool Dislocation Models .....	104
Appendix B: Common Neighbor Analysis Algorithm .....	113
Curriculum Vita .....	115

## List of Tables

Table 1.1: List of highest efficiency CdTe solar cells [18].....	4
Table 1.2: Table of material properties employed for nano-heteroepitaxy modelling. ....	8
Table 2.1: List of employed Crystal Analysis Tool lattice and defect patterns.....	36
Table 2.2: List of detected Burgers vectors detected by the Crystal Analysis tool using the zinc blende (diamond) and wurtzite (hexagonal diamond) structure patterns.....	45
Table 2.3: Comparison of system size, computing time, and computing cores used for the three different island sizes studied.....	52
Table 2.4: Comparison between simulation target temperature and actual average temperature for CdTe/ZnTe bilayer on CdS.....	55
Table 2.5: Comparison between simulation target temperature and actual average temperature for planar CdTe on CdS.....	59
Table 2.6: Comparison between simulation target temperature and actual average temperature for planar ZnTe on CdS.....	62
Table 2.7: Comparison between simulation target temperature and actual average temperature for selective CdTe on CdS.....	65
Table 2.8: Comparison between simulation target temperature and actual average temperature for selective CdTe/ZnTe bilayer on CdS.....	68
Table A.1: Wurtzite dislocation types detected by the Crystal Analysis Tool. The notation in this table refers to the schematic in Fig. A.6. *The origin needs to be transferred to the position of $\zeta$ . **The origin needs to be transferred to the position of F. Points A-G, $\alpha$ , $\beta$ , $\zeta$ are lie on the basal plane. Points $\delta$ and $\gamma$ lie on a plane above and parallel to the basal plane.....	111

## List of Figures

Figure 1.1: Illustration of (a) selective growth and (b) planar configurations indicating the different stress relief mechanisms; (i) vertical lattice deformation, (ii) lateral lattice deformation, (iii) island edge, (iv) misfit dislocation. Adapted from [19].	7
Figure 1.2: Misfit strain partitioning prediction for CdTe/CdS nano-islands. Smaller island dimensions promote an increase in 3-D relaxation and substrate partitioning as evidenced by the difference in strain values away from the interface.	9
Figure 1.3: Time and length scales for study of microstructural phenomena where MD simulations are commonly employed. Adapted from [30].	15
Figure 1.4: Flow chart of MD simulation. Adapted from [30].	16
Figure 1.5: The Stillinger-Webber potential function for a pair interaction. At atomic spacing less than $r_0$ the particles repel, while at distances greater than $r_0$ they attract. The interaction at distances greater than the virtual cutoff is negligible. Adapted from [34].	19
Figure 2.1: Sequence of images illustrate the simulated planar heteroepitaxy configuration.	24
Figure 2.3: Sequence of images illustrate the simulated selective heteroepitaxy configuration.	28
Figure 2.4: Visualization of a CdTe film: a) after deposition, b) after annealing simulation, and c) after annealing and energy minimization post-treatment steps.	30
Figure 2.5: Illustration of the steps followed by the Crystal Analysis Tool for the defect information extraction from an atomistic data set of CdTe/CdS heterostructure. Adapted from [43].	35
Figure 2.6: Top view of a closed packed plane illustrating the similarities between zinc blende and wurtzite systems and their respective lattice structures and dislocation types.	41
Figure 2.7: a) Atomistic visualization of the CdTe/CdS heterojunction. b) Visualization of the wurtzite dislocation lines detected inside the CdTe epilayer. c) Visualization of the zinc blende dislocation lines detected inside the CdTe epilayer.	42
Figure 2.8: a) Top view visualization of the wurtzite dislocation lines detected inside the CdTe epilayer. b) Top view visualization of the zinc blende dislocation lines detected inside the CdTe epilayer.	43
Figure 2.9: a) Top view cross-section visualization lattice structures along the vertical axis a) at the interface b) at the center of the film.	44
Figure 2.9: Structural defect comparison between simulated and experimental CdTe growths validates MD modeling approach. a) shows the simulation stacking fault frequency in very good agreement with the experimental image b). Figures e-f) are simulated dislocation core structures in good relation with the results reported in literature (Figures c-d). Experimental images from Li, et al. [16].	48
Figure 3.1: Plot of dislocation densities for planar CdTe / ZnTe / CdS at several deposition temperatures.	56
Figure 3.2: Structure analysis visualization for CdTe/ZnTe layers grown on CdS at a) 600 K and b) 1400 K target deposition temperatures. The red arrows serve to indicate the interface between the film and substrate.	57
Figure 3.3: Plot of dislocation densities for planar CdTe on CdS at several deposition temperatures.	60
Figure 3.4: Plot of dislocation densities for planar ZnTe on CdS at several deposition temperatures.	63

Figure 3.5: Plot of dislocation densities for selective CdTe on CdS at several deposition temperatures. ....	66
Figure 3.7: Cross-section visualization of a structural analysis for selective CdTe/ZnTe grown on CdS at a) 1000 K, b) 1100 K, and c) 1200 K (target temperatures). Red arrows indicate the location of the film-substrate interface. ....	70
Figure 3.8: Plot of dislocation densities for multiple size CdTe islands grown on CdS. ....	73
Figure 3.9: Dislocation profile visualizations for multiple size CdTe islands grown on CdS. a) ~214 Å, b) ~430 Å, and c) ~640 Å island width. ....	74
Figure 3.10: Lattice structure maps for material slices parallel to the interface plane at a distance of half the epilayer thickness. Fewer grains are observed in the smallest island (a), while the grain size and type increase with larger island size (b and c). ....	75
Figure 3.12: Plot of composition profile for planar Cd <sub>0.8</sub> Zn <sub>0.2</sub> Te deposited on CdS. ....	79
Figure 3.13: Cross-section visualization of a planar Cd <sub>0.8</sub> Zn <sub>0.2</sub> Te film deposited on CdS a) species b) structural analysis. The red arrows indicate the location of the film-substrate interface. ....	80
Figure 3.14: Top view dislocation profile visualization for a planar Cd <sub>0.8</sub> Zn <sub>0.2</sub> Te film deposited on CdS a) zinc blende dislocations b) wurtzite dislocations. ....	81
Figure 3.15: Plot of dislocation densities for several x composition values in Cd <sub>(1-x)</sub> Zn <sub>x</sub> Te selective film depositions grown on CdS. ....	83
Figure 3.16: Plot of composition profile for selective Cd <sub>0.8</sub> Zn <sub>0.2</sub> Te deposited on CdS. ....	84
Figure 3.17: Atomistic visualization of a selective Cd <sub>0.8</sub> Zn <sub>0.2</sub> Te deposited on CdS simulation. a) cross-section image showing the different atomic species within the nanostructure b) cross-section image showing the identified lattice structures within the nanostructure. The red arrows indicate the location of the film-substrate interface. ....	85
Figure 3.18: Dislocation profile top view visualization of defects detected within a selective Cd <sub>0.8</sub> Zn <sub>0.2</sub> Te deposited on CdS simulation. a) zinc blende dislocations b) wurtzite dislocations. Refer to Table 2.2 for dislocation type indexing. ....	86
Figure 3.19: Plot of comparing the defect densities for several nano-structured CdTe films deposited on CdS. ....	88
Figure 3.20: Atomistic visualization of the planar and selective CdTe on CdS systems after energy minimization. ....	93
Figure 3.21: Plot of potential energy difference between planar and selective CdTe on CdS. ....	94
Figure 3.22: Atomistic visualization of the selective Cd <sub>(1-x)</sub> Zn <sub>x</sub> Te on CdS systems after energy minimization. ....	95
Figure 3.23: Plot of potential energy difference between planar and selective CdTe/ZnTe/CdS. ....	96
Figure 3.24: Plot of potential energy difference between planar and selective Cd <sub>0.8</sub> Zn <sub>0.2</sub> Te on CdS. ....	97
Figure A.1: Atomistic data visualization of a coherent twin model (blue atoms) with periodic images (red atoms) to aid structural identification. ....	107
Figure A.2: Atomistic data visualization of an intrinsic stacking fault model (blue atoms) with periodic images (red atoms) to aid structural identification. ....	108
Figure A.3: Atomistic data visualization of an extrinsic stacking fault model (blue atoms) with periodic images (red atoms) to aid structural identification. ....	109
Figure A.4: Dislocation visualization of the results obtained for the four different tests designed to evaluate the performance of four different hexagonal diamond defect detection analysis configurations. ....	110

Figure A.6: Schematic of a wurtzite crystal illustrating different dislocation types and the vector notation for hexagonal systems. The notation in this figure refers to the information listed in Table A.1 .....	112
---	-----

## Chapter 1: Introduction

This section will cover an introduction to the current state of CdTe PV technology and the advanced characterization and simulation techniques used to further understand and improve this material. A description of two defect reduction strategies, selective area growth and Zn alloying, is provided. A brief review of molecular dynamics and the Stillinger-Webber potential employed in this work is also discussed.

### 1.1 CdTe PV Technology

The CdTe thin film solar cell is one of the most promising photovoltaic technologies because of its low production costs and the continued growth of its production capability. CdTe is an ideal solar cell material for terrestrial applications due to its near-optimum bandgap ( $\sim 1.5$  eV) and a high absorption coefficient. However, the technology has yet to reach its theoretical maximum conversion efficiency ( $\sim 32\%$ ) with current average production modules reaching  $\sim 14\%$ . Table 1.1 shows the latest efficiencies achieved by First Solar, the company that currently produces the record performance devices. If CdTe solar cells can reach their maximum efficiency, the technology could become a competitive energy solution.

The low efficiencies achieved by this technology are in part attributed to the high carrier recombination at the interface. This undesired effect is caused by a high defect density that originates from the large strain (as defined in [1]) experienced between the CdS substrate and the CdTe film ( $\sim 11\%$ ) [2]. These defects can trap charge carriers and hinder the solar cell efficiency because of the resulting low open circuit voltage ( $V_{oc}$ ) and low fill-factor (FF) [3].

Many research efforts to increase CdTe PV efficiencies consist of optimizing device post-processing recipes in order to treat defects formed during fabrication. A popular approach is the  $CdCl_2$  treatment that consists of exposing the thin films to  $CdCl_2$  at high temperatures (350-450 °C) with an oxygen rich environment [4] [5]. This treatment has been proven to increase minority carrier lifetime, as well as  $V_{oc}$ , short circuit current ( $J_{sc}$ ), and FF. In contrast, Cruz-Campa, et. al [6] have proposed an approach that directly prevents the formation of defects

during fabrication. It involves creating nanostructured CdTe/CdS solar cells by means of combining selective area growth and Zn ternary alloying to enable strain relief mechanisms and reduce lattice mismatch effects to produce high quality thin films. The aim is to decrease the defect presence to lower the charge carrier recombination and achieve  $V_{oc}$  values above 1.0 V.

Regardless of what fabrication approach is followed, it is clear that a deeper insight into the atomic scale effects of crystal lattice imperfections is needed to understand how they affect the macro-scale properties of the material and then apply this understanding to develop appropriate fabrication methods. In order to address this need, several experimental efforts apply advanced characterization techniques (such as cathodoluminescence (CL), transmission electron microscopy (TEM), etc.) to investigate film morphology, electrical, and optoelectronic properties. A topic of great interest has been the study of grain boundary morphology and how they are affected by the  $CdCl_2$  treatment [7] [8] [9]. Moseley, et. al [8] have shown that as grown CdTe film grain boundaries as well as defects in grain interiors act as major recombination centers consisting of dislocation cores that act as deep states, meanwhile the  $CdCl_2$  treatment passivated this effect with limited efficacy.

Other studies have focused in capturing detailed information about the structures of these defects including dislocation cores [10] [11], twin boundaries [12] , other planar defects [13] [14] [15], and used it to recreate models for *ab initio* calculations that describe their electronic properties. However, the characterization methods needed to obtain a clear view of these structures present a number of challenges to prepare an ideal sample for study. Even then, some defect structures may be unstable and could disappear due to the influence of the characterization equipment [16]. The use of high fidelity molecular dynamics (MD) simulations can help address these challenges by providing unprecedented film morphology data that fully describes defect structures in 3D space. In addition, the application of powerful defect detection algorithms and visualization software tools can provide researchers a deeper understanding of the defect geometries (even unstable structures), distribution, and possible interaction beyond the means of any current characterization tool available. This work employed a carefully parameterized



Stillinger-Webber that has been verified to predict crystal growth of II-IV elements and therefore enables the study of defects formed during epitaxy, unlike other efforts [17] that predicted amorphous CdTe growths.

In this study we applied MD simulations to explore the fabrication strategies proposed by Cruz-Campa, et. al [6] at an atomic scale and used advanced defect detection analysis algorithms to evaluate the efficacy of these approaches. In addition, advanced visualization tools were employed to observe three dimensional geometries that describe dislocation networks found within the epilayer/substrate heterostructure with resolution that is unmatched by current experimental efforts. Simulated defect structures were validated with experimental data available in literature. The goal was to develop a simulation capability that can implement nanostructured thin film vapor deposition and demonstrate that the data obtained can provide valuable insight into the material system behavior. These simulation results could guide experimental efforts and also serve as catalyst for more comprehensive studies such as *ab initio* calculations.

Table 1.1: List of highest efficiency CdTe solar cells [18].

<b>Device</b>	<b>Efficiency (%)</b>	<b>Area (cm<sup>2</sup>)</b>	<b>V<sub>oc</sub> (V)</b>	<b>J<sub>sc</sub> (mA/cm<sup>2</sup>)</b>	<b>Fill Factor (%)</b>
Research cell	21	1.0623	0.8759	30.25	79.4
Record module	17.5	-	-	-	-
Avg. production module	14.1	-	-	-	-

## 1.2 Selective Area Epitaxy

Nanoheteroepitaxy [19] consists of selective area epitaxial growth on patterned substrates with the objective of nucleating an array of nanoscale ( $\sim 100$  nm) islands of high quality material. This configuration enables additional strain relief mechanisms as compared to a conventional planar epilayer due to the free surfaces at the edges (iii) of the island and the strain partitioning between the substrate and the epilayer as illustrated in Fig. 1.1. In a conventional planar structure the epilayer can only deform vertically (ii) to relieve mismatch strain. In contrast a selectively grown epilayer can deform vertically (ii) and laterally (ii) distributing the mismatch strain in three dimensions. Finally, dislocations found within the islands could climb or glide on to the new surfaces created by the island edges, unlike in planar growths where they would likely remain in the epilayer.

The prediction of strain partitioning as a function of distance from the interface is described by the following expressions [19] for the epilayer (e subscript) and the substrate (s subscript):

$$\varepsilon_e = \varepsilon_e^0 e^{\frac{-\pi z}{L}} \quad (1)$$

$$\varepsilon_s = \varepsilon_s^0 e^{\frac{\pi z}{L}} \quad (2)$$

The island width is defined as  $L$ , while the distance from the interface is described by  $z$ .  $\varepsilon_e^0$  and  $\varepsilon_s^0$  are the interfacial epilayer and substrate strains defined respectively by the following equations:

$$\varepsilon_e^0 = \frac{(a_s - a_e)(1 - e^{\frac{-\pi h_s}{L}})}{a_e \left(1 - e^{\frac{-\pi h_s}{L}}\right) + K a_s (1 - e^{\frac{-\pi h_e}{L}})} \quad (3)$$

$$\varepsilon_s^0 = \frac{K(a_e - a_s)(1 - e^{\frac{-\pi h_e}{L}})}{a_e \left(1 - e^{\frac{-\pi h_s}{L}}\right) + K a_s (1 - e^{\frac{-\pi h_e}{L}})} \quad (4)$$

Where  $a_s$  and  $a_e$  are the substrate and epilayer lattice constants.  $K$  is the elastic compliance ratio defined as:

$$K = \frac{Y_e(1 - \nu_s)}{Y_s(1 - \nu_e)} \quad (5)$$

Where  $Y_s$  and  $Y_e$  are the substrate and epilayer Young's modulus. Similarly  $\nu_s$  and  $\nu_e$  are the substrate and epilayer Poisson's ratio. Fig. 1.3 shows the partitioned strain curves (equations 1 and 2) for CdTe/CdS islands of 20, 40, and 60 nm widths. The plot shows that smaller island widths better enable 3-D relaxation mechanisms that relax epilayer strain and substrate partitioning as the distance from the interface increases. Table 1.2 lists the material properties that were used for the modeling of nano-heteropitaxy of these CdTe/CdS heterostructures.

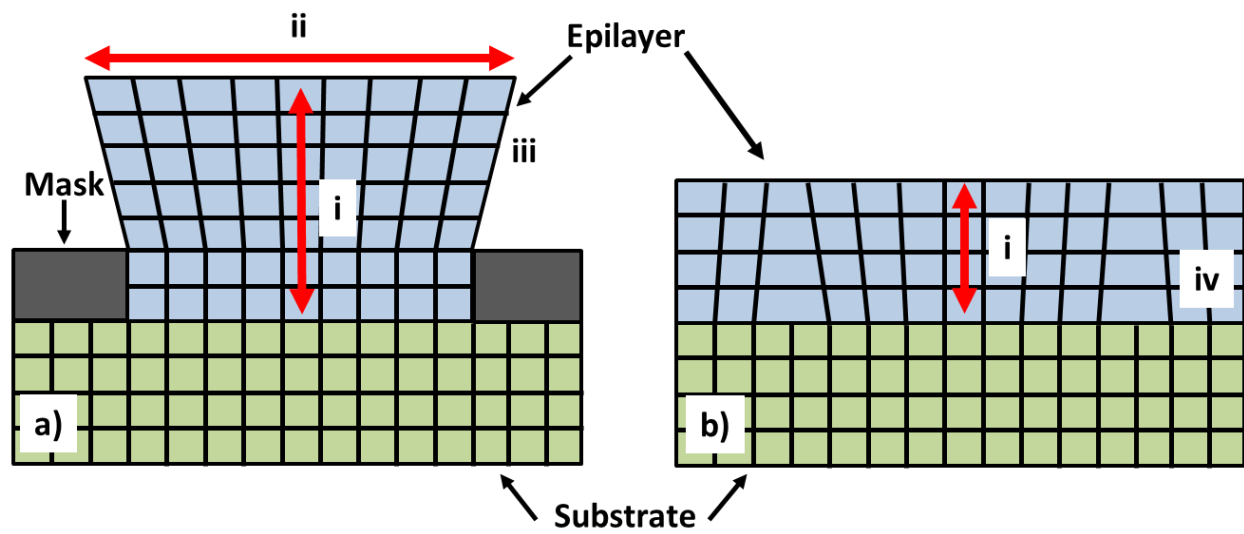


Figure 1.1: Illustration of (a) selective growth and (b) planar configurations indicating the different stress relief mechanisms; (i) vertical lattice deformation, (ii) lateral lattice deformation, (iii) island edge, (iv) misfit dislocation. Adapted from [19].

Table 1.2: Table of material properties employed for nano-heteroepitaxy modelling.

<b>Material Property</b>	<b>CdS</b>	<b>CdTe</b>
Young's Modulus ( $Y$ )	42 (Gpa)	36.52 (Gpa)
Poisson's Ratio ( $\nu$ )	0.38	0.41
Lattice Constant ( $a$ )	0.5835 (nm)	0.6478 (nm)

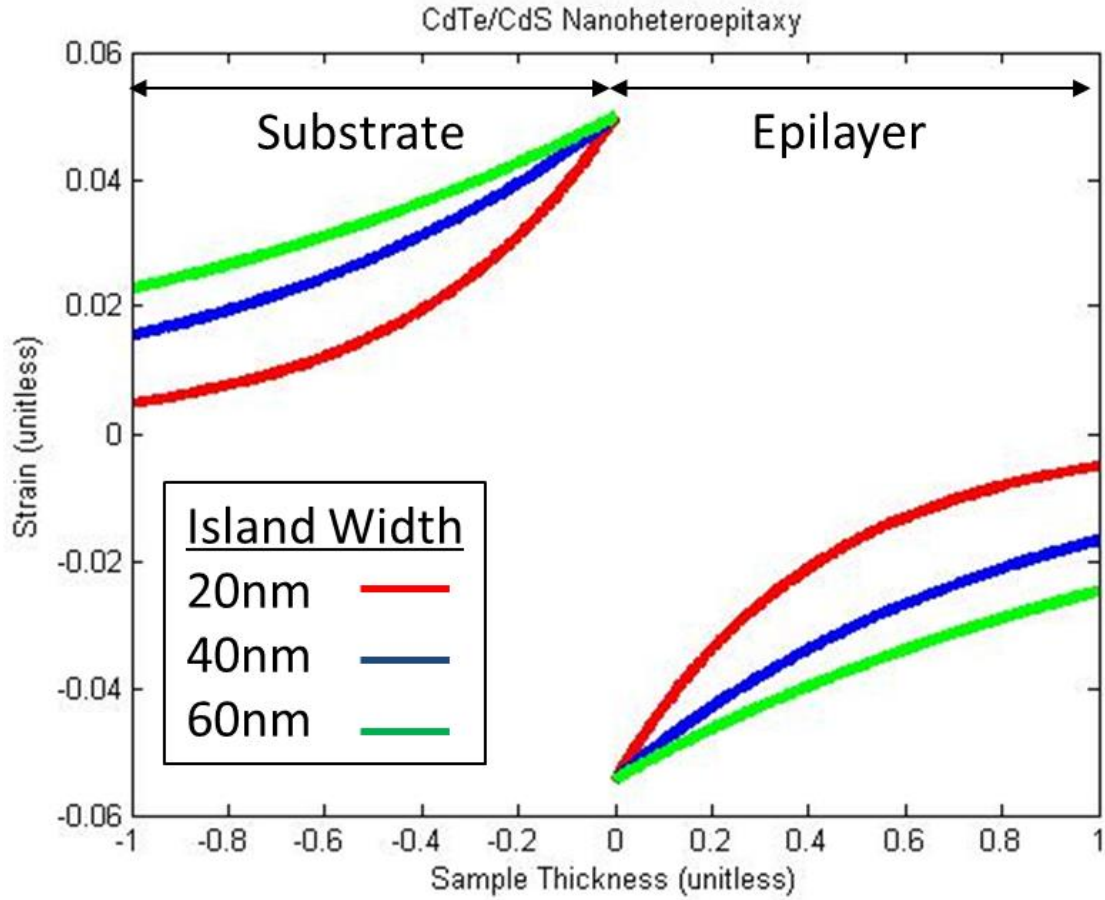


Figure 1.2: Misfit strain partitioning prediction for CdTe/CdS nano-islands. Smaller island dimensions promote an increase in 3-D relaxation and substrate partitioning as evidenced by the difference in strain values away from the interface.

### 1.3 $\text{Cd}_{(1-x)}\text{Zn}_x\text{Te}$ Alloying

The incorporation of Zn to form the a  $\text{Cd}_{(1-x)}\text{Zn}_x\text{Te}$  ternary alloy buffer layer in the CdTe/CdS solar cell structure was proposed by Cruz-Campa, et. al [6] as a strategy to increase solar cell efficiency via reducing the number of defects in the epilayer that are caused due to the large strain ( $\sim 11\%$ ) between CdS and CdTe.

One of the ZnTe buffer layer predicted benefits is that it could serve to decrease the strain experienced between the epilayer and the substrate [6]. ZnTe has a  $\sim 4.5\%$  strain with respect to the CdS substrate, while the CdTe experiences a  $\sim 6\%$  strain with respect to the ZnTe buffer layer. The improved lattice matching experienced between the multilayers could lower the presence of performance hindering defects such as misfit dislocations and contribute to enhanced device performance.

The use of Cd-based II-VI semiconductor film grading to improve lattice matching with substrates is a topic that has been widely researched for optoelectronic applications [20] [21] [22]. These efforts aim towards the fabrication of high quality composite substrates with exact lattice matching to HgCdTe that could be used to produce low defect, high performance radiation detection devices. The composite substrates were created by molecular beam epitaxy depositions of ternary and quaternary alloyed films containing Cd, Zn, Te, and Se deposited on Si (211) substrates (this substrate experiences a  $\sim 19\%$  strain with CdTe). The results report that high quality films can be deposited on Si (211) as long as the Se and Zn concentrations are low ( $< 4\%$  for Se and Zn combined). Species concentrations were determined using wavelength dispersive spectroscopy. The alloyed film thickness was  $\sim 6 \mu\text{m}$ .

The authors [20] [21] [22] observed an alloy disordering effect that became more severe at high Se or Zn concentrations. Films with high Se or Zn concentrations exhibited an increase in surface morphology roughness (determined with an optical microscope) and increased dislocation density (determined by etched-pit density) when compared to samples where the Se or Zn concentrations were low. The alloy disordering effect was speculated to be a distortion of the CdTe matrix caused by segregation of a third (or also fourth) species resulting in lattice



alterations that degrade the crystallinity of the film. This effect was observed to be more drastic for Zn than Se, suggesting that segregation appears to be lower for Se than Zn. The best film quality for samples containing Zn occurred when its concentration was  $< 1.5\%$ , while the optimal concentration for samples containing Se was  $< 4\%$ . These results suggest that the most promising strategy for producing low defect  $\text{Cd}_{(1-x)}\text{Zn}_x\text{Te}$  films would likely occur for low  $x$  values.

An additional anticipated benefit is the creation of a graded band gap semiconductor that can be engineered by controlling the Zn concentration [6] forming an internal built-in electrostatic field that could improve device efficiencies by improving minority carriers collection [23], preventing interface recombination [24], and localizing carrier absorption [25].

Contreras, et. al have demonstrated improved efficiencies in thin film poly-crystalline  $\text{Cu}(\text{In,Ga})\text{Se}_2$  solar cells due to customized bandgaps accomplished by compositional variations in the device multilayers that generated force fields that improved carrier collection [26]. The compositional variations in the absorber layer were accomplished with a three stage processing using an in-line co-evaporation [27] system where a computer precisely controls species evaporation and flux [26]. During each stage the In, Ga, Cu, and Se species fluxes are evaporated following precise programmed profiles that effectively create the desired graded semiconductor. The reported CIGS layer thickness was  $\sim 2\text{-}3.25\ \mu\text{m}$ . Similarly, Dalal, et al. have modeled graded junction layers in amorphous silicon solar cells and reported promising results in electron collection and surface recombination inhibition if the resultant field and graded layer can be extended over the width of their simulated device junction layer (100nm) and the slope of the field is low [28]. A crucial design constraint for  $\text{Cd}_{(1-x)}\text{Zn}_x\text{Te}$  solar cells was reported by Anwar [29], where numerical modeling indicated degraded device performance could be obtained for high Zn concentrations ( $x > 0.3$ ) due to an unfavorable conduction band offset that generates a kink near the  $V_{oc}$  of the J-V curves.

The behavior reported in literature suggests that Zn incorporation in  $\text{CdTe/CdS}$  solar cells could be beneficial only if its optimal concentration can be achieved and controlled during fabrication. This would ensure that the benefits on device performance due to improved lattice

matching are significant and offset the fabrication challenges that accompany the integration of the  $\text{Cd}_{(1-x)}\text{Zn}_x\text{Te}$  buffer layer.

#### 1.4 Molecular Dynamics

Molecular dynamics (MD) is one of many simulation tools available to study the behavior of materials at an atomic level resolution with an amount of insight that can't be achieved through experimental characterization. In simple terms, MD simulations consist of creating and tracking the trajectories of particles that represent the atoms in a material system by direct numerical integration of Newton's equations of motion, and the interactions between atoms are described using a specified potential function [30].

There are two major types of MD simulations available: *ab initio* and classical. In *ab initio* MD the forces on the nuclei from the surrounding electronic structure are computed "on-the-fly" as the trajectory of the particles in the system changes, meaning that the electronic interactions are active degrees of freedom during the simulation [31]. In contrast, for classical MD the atoms are treated as classical entities and the interactions between atoms are predefined in a potential function [30]. These simulations separate the electronic and nuclear motions of particles by assuming the Born-Oppenheimer [32] approximation, where the nuclei are treated as being fixed in instantaneous positions and the electrons (due to their relatively fast motion because of their small mass in comparison with nuclei) are assumed to always be in ground state [30]. This work employed classical MD simulations.

One major strength of MD is the ability to describe crystal geometry with good approximation using only the interatomic potential and the position of the particles in the system with no further assumptions made. The virtual experiment can reveal unexpected structures with the use of advanced visualization tools. The results obtained can often contribute towards developing an understanding of a physical phenomenon and provide valuable insight towards the design of succeeding calculations with higher accuracy such as *ab initio* MD, as well as providing guidance in experimental efforts. Unlike experimental approaches that are often

affected by extraneous factors, MD creates an ideal environment to conduct numerical experiments in which there is perfect control over the initial, boundary and intermediate conditions that make it possible to easily explain any phenomena that is observed.

One major limitation in the use of MD in computational computer science is the time-scale it can model. The simulation needs to be able to account for atomic inertia and vibrations that occur typically in the picosecond range [30]. Therefore the simulation time step needs to be at least two orders of magnitude below this value (typically  $\sim 10^{-15}$  s). Most MD simulations are normally used to study phenomena over time intervals below  $\sim 1$ -10 ns [30], although the development of massively parallel computers can push this limit to close to milliseconds. Fig. 1.3 illustrates the range of length and time scales where MD can be applied for the study of microstructural phenomena. One more limitation is the availability of accurate interatomic potentials that limit the number of material systems that can be studied, although this situation can be expected to improve as the method becomes more widely known and attracts the focus of researchers to expand this field.

Fig. 1.4 shows a flowchart of the typical steps followed in an MD simulations code. The first step consists of creating the initial configuration of the system. The initial configuration (at time  $t_0$ ) can consist of atoms arranged in a crystal lattice forming a substrate, atomic vapor at random positions, etc. The next consists of assigning initial velocities to the particles in the initial configuration. Afterwards, the force on each particle is computed by numerically solving Newton's equations. The computation results update the positions and velocities of particles for the next time step ( $\Delta t$ ). At this point an output file can be created that captures the current velocities and positions of the particles of the system if desired. If the simulation has reached a predetermined final time step ( $L$ ) the simulation ends, otherwise the code goes back to calculating the force of the updated system configuration and repeats this cycle until the final time step is reached.

In an MD simulation with a system containing  $N$  particles, during any instant of time  $t$  the coordinates of the particles are kept in a 3 by  $N$  dimensional vector,  $\mathbf{r}^{3 \times N} \equiv$

$\{r_1(t), r_2(t), \dots, r_N(t)\}$ , where  $\mathbf{r}_i$  holds the x, y, z coordinates for atom  $i$ . The initial configuration of the system is defined as  $\mathbf{r}^{3xN}(t_0)$ . Similarly, the initialized particle velocities are kept in vector  $\mathbf{v}^{3xN}(t_0)$ .

The energy of the system in an MD simulation consists of the sum the kinetic and potential energies of the particles in the system. The kinetic energy is the sum of the individual kinetic energies of all atoms in the system,

$$K = \frac{1}{2} m \sum_{j=1}^N \mathbf{v}_j \cdot \mathbf{v}_j \quad (6)$$

The potential energy is described by the interatomic potential employed and can consist of the interaction of all particles in the system,  $U = U(\mathbf{r}^{3xN})$ . Typically an approximation is employed by limiting the interaction to a few particles only, i.e. pair-wise interaction, in order to reduce the computational load.

Afterwards Newton's equations of motion need to be solved numerically in order to find the atom trajectories in the following time step. There are multiple integration schemes that can be used to achieve this, one of these is the Verlet method [33], briefly described in the following paragraphs. The Newton equation for the N particle system is given by:

$$m \frac{d^2 \mathbf{r}_j}{dt^2} = -\nabla_{\mathbf{r}_j} U(\mathbf{r}^{3xN}), j = 1, \dots, N \quad (7)$$

Where  $m$  is the particle mass and  $U$  is the potential energy. The simulation time is divided into small time steps  $\Delta t$ , causing the system to evolve in successive time increments starting at the initial conditions  $\mathbf{r}^{3xN}(t_0)$  until reaching the final time step  $\mathbf{r}^{3xN}(t_L)$ .

The Verlet method for numerically solving Newton's equation adds the two Tailor series expansions for  $r_j(t_0 - \Delta t)$  and  $r_j(t_0 + \Delta t)$  to obtain this expression:

$$r_j(t_0 + \Delta t) = -r_j(t_0 - \Delta t) + 2\mathbf{r}_j(t_0) + \mathbf{a}_j(t_0)(\Delta t)^2 + \dots \quad (8)$$

The left side of this expression gives the position of particle  $j$  at the following time step.  $\mathbf{a}_j$  is the acceleration of the particle, and can be substituted by  $\frac{\mathbf{F}_j(\mathbf{r}^{3xN}(t_0))}{m}$ , where  $\mathbf{F}_j$  is given by the right side of equation 7. In an MD simulation equation 8 is solved for the successive increments of  $\Delta t$  until the final time step is reached.

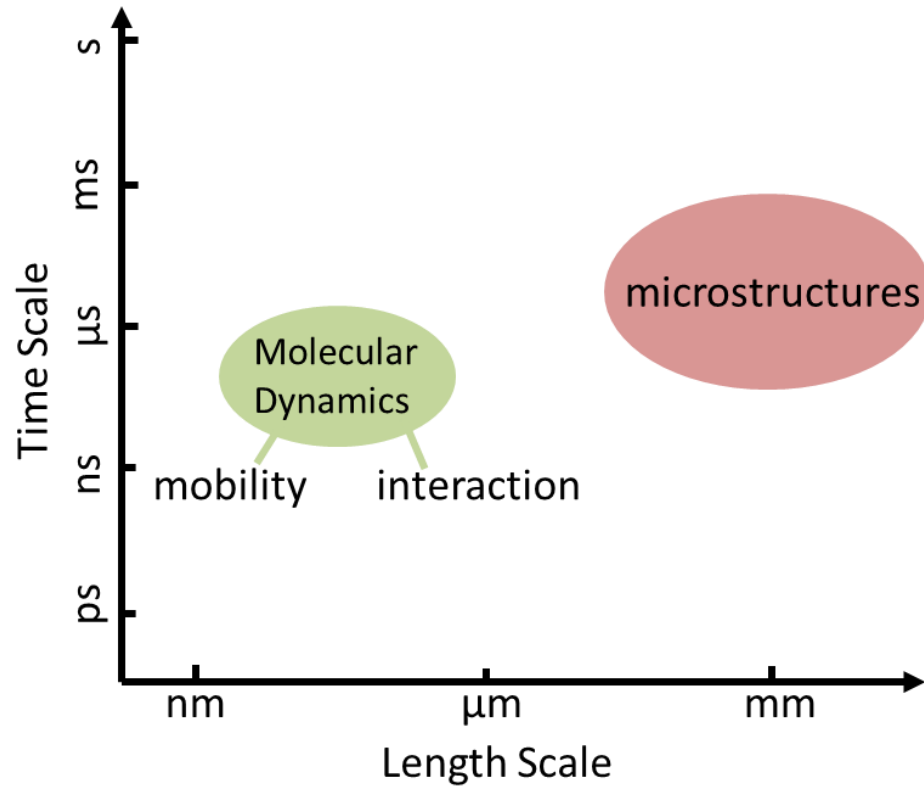


Figure 1.3: Time and length scales for study of microstructural phenomena where MD simulations are commonly employed. Adapted from [30].

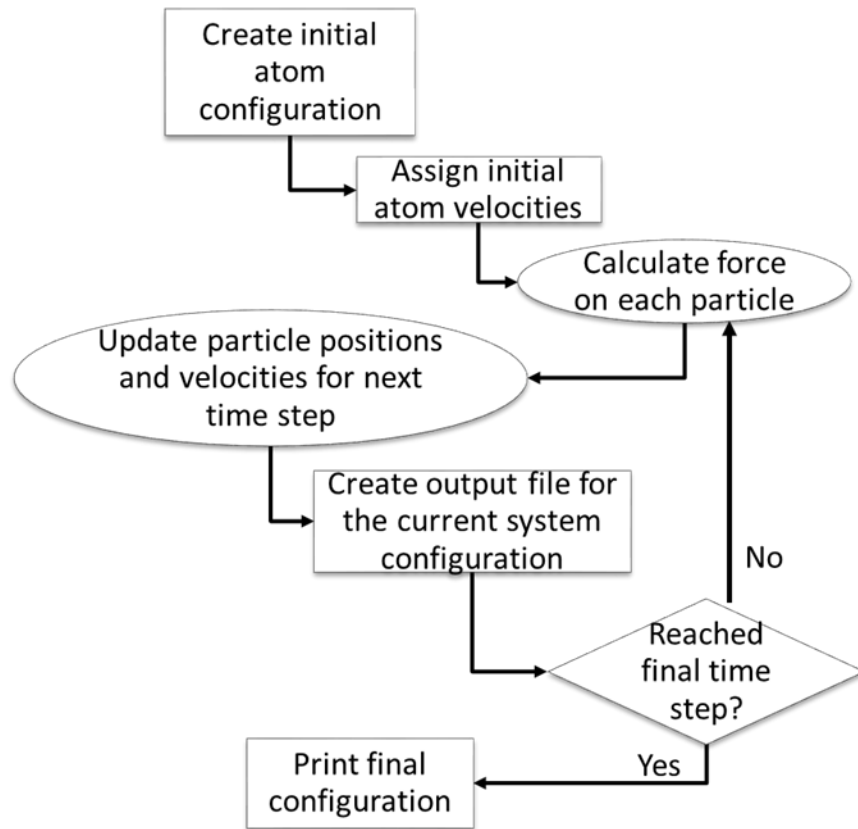


Figure 1.4: Flow chart of MD simulation. Adapted from [30].

## 1.4 Stillinger-Webber Potential

The choice of the interatomic potential is critical in MD simulations since it controls the complexity of the algorithm that computes the atomic interactions forces as well as the fidelity of the results. This work employs the Stillinger-Webber potential for the II-VI elements Cd, Te, Zn, S, Hg, and Se developed by Zhou, et. al [34]. This potential has been carefully parameterized to ensure that it reproduces the experimental lattice constants, cohesive energies, and elastic constants of all binary compounds [34]. It also captures the correct energy trends to predict the formation of stoichiometric compounds under stoichiometric conditions. In addition its predictive capability has been verified through challenging crystal growth simulations under different stoichiometric conditions.

Stillinger-Weber potentials are branded with employing an energy penalty for non-tetrahedral bond angles to ensure the tetrahedral structure (such as zinc blende and wurtzite) is the lowest energy configuration. If this penalty is applied properly the properties of the compound phases are correctly predicted and it is possible to study the formation of defects.

The Stillinger-Webber potential function for a system of  $N$  atoms has the following format:

$$U = \frac{1}{2} \sum_{i=1}^N \sum_{j=i_1}^{i_N} \left[ V_{IJ}^R(r_{ij}) - V_{IJ}^A(r_{ij}) + u_{IJ}(r_{ij}) \times \sum_{k=i_1}^{i_N} u_{IJ}(r_{ik}) \left( \cos \theta_{jik} + \frac{1}{3} \right)^2 \right] \quad (9)$$

Where  $i_1, i_2, \dots, i_N$  is a list of neighbor of atom  $i$ ,  $\theta_{jik}$  is the bond angle formed by neighbor atoms  $j$  and  $k$ .  $V_{IJ}^R(r_{ij})$  is the pairwise repulsive function, while  $V_{IJ}^A(r_{ij})$  is the pairwise attractive function. The  $u_{IJ}(r_{ij}) \times \sum_{k=i_1}^{i_N} u_{IJ}(r_{ik}) \left( \cos \theta_{jik} + \frac{1}{3} \right)^2$  is a three-body term that penalizes non-tetrahedral angles. The  $ij$  subscript indicates the pair of atoms, while  $IJ$  subscript indicates the species of the pair of atoms [34].

Fig. 1.5 plots the Stillinger-Webber potential as a function of pairwise distance. At atomic spacing less than  $r_0$  the particles repel, while at distances greater than  $r_0$  they attract. The minimum of the function occurs at  $r_0$ , which is also the nearest neighbor distance. The repulsion occurs due to the overlap of the electron clouds. The attraction is caused by the interaction

between the induced dipole in each particle. The interaction at distances greater than the virtual cutoff is negligible.



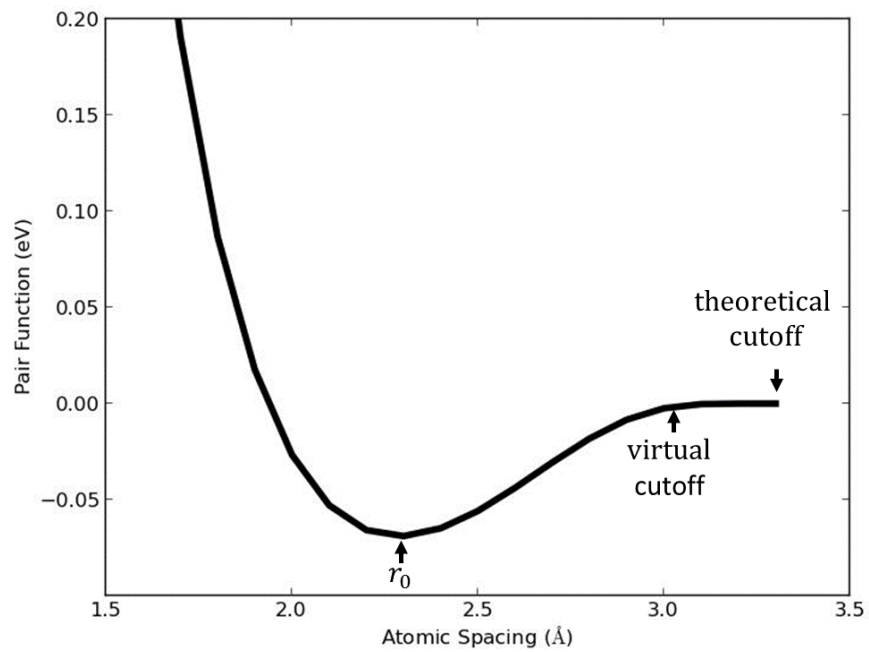


Figure 1.5: The Stillinger-Webber potential function for a pair interaction. At atomic spacing less than  $r_0$  the particles repel, while at distances greater than  $r_0$  they attract. The interaction at distances greater than the virtual cutoff is negligible. Adapted from [34].

## 1.5 Research Objectives

In this dissertation, defect reduction strategies for CdTe/CdS thin film solar cells are studied at the atomic scale using MD simulations. First, the simulation code that incorporates the novel fabrication procedures during a thin film growth is developed and applied to produce the nanostructured samples. Then, advanced analysis algorithms were applied to characterize and identify crystal lattice defects within the raw data. However, the Crystal Analysis Tool could not detect defects in wurtzite materials (only zinc blende originally), therefore new wurtzite structure defect models are developed and evaluated to expand the tool's capability. The analyses results are then compared to detect trends and evaluate the efficacy of each defect-reducing nanostructure.

The first defect reduction strategy evaluated is the incorporation of Zn for improved lattice matching between epilayer and substrate. The newly developed deposition code is used to obtain controlled species concentrations in  $\text{Cd}_{(1-x)}\text{Zn}_x\text{Te}$  thin films over a wide range of growth configurations and alloy profiles. In particular the following aspects are addressed:

- Defect trends for  $\text{Cd}_{(1-x)}\text{Zn}_x\text{Te}$  as a function of Zn concentration
- Types of defects found within  $\text{Cd}_{(1-x)}\text{Zn}_x\text{Te}$  films
- Optimal deposition temperature for low defect  $\text{Cd}_{(1-x)}\text{Zn}_x\text{Te}/\text{CdS}$  simulated thin films
- Optimal Zn concentration for low defect  $\text{Cd}_{(1-x)}\text{Zn}_x\text{Te}/\text{CdS}$  simulated thin films

The second defect reduction strategy studied is the selective area growth of CdTe to enable strain relief mechanisms that improve epilayer material quality. The simulation capability to model selective area growth is developed and used to grow islands of different sizes. One more set of simulations are produced that combine both selective area growth and Zn alloying over a variety of selective  $\text{Cd}_{(1-x)}\text{Zn}_x\text{Te}$  configurations for one island size. In particular the following aspects are addressed:

- Defect trends for selective CdTe as a function of island size
- Defect trends for selective  $\text{Cd}_{(1-x)}\text{Zn}_x\text{Te}$  as a function of Zn concentration

- Types of defects found within selective  $\text{Cd}_{(1-x)}\text{Zn}_x\text{Te}$  films
- Optimal deposition temperature for selective  $\text{Cd}_{(1-x)}\text{Zn}_x\text{Te}/\text{CdS}$  simulated thin films
- Optimal Zn concentration for selective  $\text{Cd}_{(1-x)}\text{Zn}_x\text{Te}/\text{CdS}$  simulated thin films

## Chapter 2: Methodologies

The following sub-sections describe details about the simulation configuration, post-processing analysis software tools, and experiment designs. The procedures described in this chapter were employed to obtain the results presented in chapter 3.

### 2.1 Simulation Configuration

This work employed three major types of molecular dynamics simulations: planar thin film growth, selective area growth, and post-growth treatments. The details for each configuration are discussed in the following sub-sections.

#### 2.1.1 Simulated Thin Film Growth

The simulated growth employed the Large-Scale Atomic/Molecular Massively Parallel Simulator (LAMMPS) molecular dynamics package [35]. The atomistic interactions were defined within the Stillinger-Webber potential that can simulate the II-VI elements Cd, Zn, Te, S, Hg, and Se [34]. In a simulated growth, adatoms are deposited on top a substrate under favorable conditions to induce epitaxial growth. The atomic vapor consisted of groups of atoms that are created in random positions on top of the substrate and are given initial velocities with a direction towards the substrate's surface. The atomistic diffusion that occurs on the substrate surface and the conditions for nucleation have been discussed in detail by Almeida, et al. [36]. In simple terms, during a simulation once these adatoms come in contact with the substrate some will nucleate and begin forming a grain while others re-evaporate. During a simulation, the re-evaporated atoms are removed to prevent collision and interaction with incoming adatoms. After the previous group has been cleansed (re-evaporated atoms have been deleted), a new group of adatoms is formed and the process repeats in a cycle until the simulation reaches the final time step. The elemental composition ratio of each atomic vapor group is assigned according to the desired epilayer stoichiometry, i.e.  $\text{Cd} = 0.25$ ,  $\text{Zn} = 0.25$ ,  $\text{Te} = 0.5$  to obtain a  $\text{Cd}_{0.5}\text{Zn}_{0.5}\text{Te}$  epilayer.

The initial substrate structure employed in this work consisted of a wurtzite CdS single crystal with a (0001) CdS oriented surface plane. The [-1100], [0001], [11-20] crystallographic orientations of the crystal aligned with the x, y, z axes of the simulation respectively. Periodic boundary conditions were employed in the horizontal (lateral) directions (x and z), and a free boundary condition in the vertical y direction. The substrate lattice constants were  $a = 4.12597 \text{ \AA}$  and  $c = 6.73768 \text{ \AA}$ .

Visualization of the simulated substrate configurations can be observed in Fig. 2.1 in which Cd and Te adatoms are deposited on top of a CdS substrate. The atoms inside the semi-transparent red box have their positions completely fixed in order to prevent drift due to momentum transfer from the colliding adatoms. An initial substrate temperature was introduced using a Gaussian distribution. The substrate's temperature was regulated using a Nose-Hoover algorithm [37] on the atoms inside a region (green box in Fig. 2.1) to approximate isothermal conditions. The isothermal region began on top of the fixed region and ended a few monolayers below the surface. The top substrate monolayers were kept outside the isothermal region to allow natural surface dynamics consisting of interactions between adatoms and substrate atoms. The top limit of the isothermal region was readjusted according to the film's growth rate in order to keep an approximately constant distance to the substrate's surface throughout the length of the simulation.

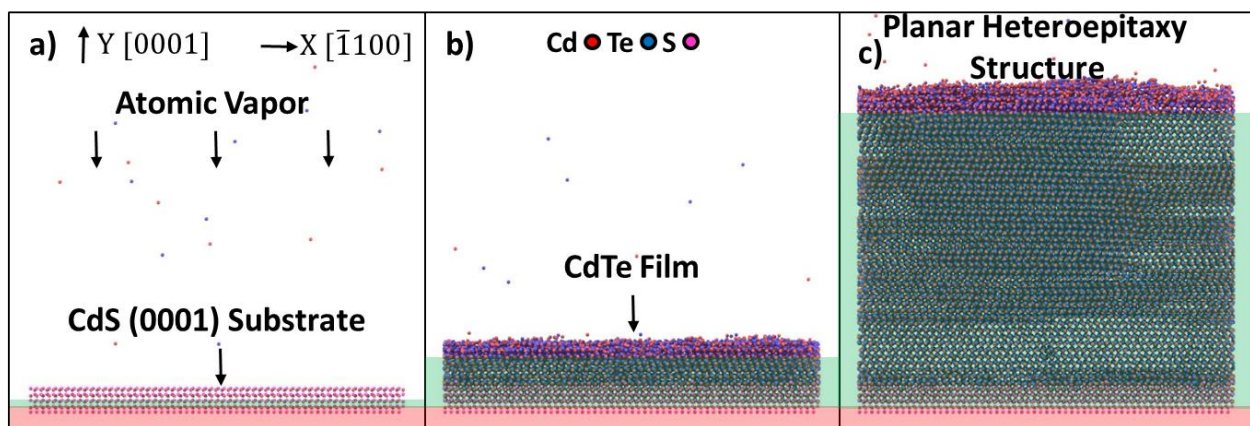


Figure 2.1: Sequence of images illustrate the simulated planar heteroepitaxy configuration.

### 2.1.2 Simulated Thin Film Selective Area Growth

The simulation of selective area growth required the implementation of wall material to be placed on top of the CdS substrate confining the epilayer and disfavoring the nucleation of adatoms on to itself. Experimentally this is achieved by the use of a dielectric layer, such as SiO<sub>2</sub>, that is then patterned through the use of lithography to create window openings to the substrate as shown by Aguirre et. al [38]. The selective area growth simulations in this work employed a modified Stillinger-Weber potential that uses atoms with artificially lowered sticking coefficient to act as the dielectric layer. This was achieved by using modified Cd and Te (dCd and dTe) atoms with half of the attractive force component in the interatomic potential in comparison with the regular elements. This modification successfully created a material that mimics the effect of the dielectric layer.

The simulated mask and substrate structure required three preparation steps as observed in Fig. 2.2. The first step is shown in Fig. 2.2.a and consists of creating a wurtzite single crystal with the desired number of CdS monolayers to create a substrate and the rest of the crystal is formed of dCd and dTe atoms. The second step consists of a simulation to melt the dCd and dTe crystal into an amorphous phase as seen in Fig. 2.2.b. During this simulation the CdS atoms and a top layer of the dCd and dTe crystal are fixed in position in order to preserve the substrate structure and to prevent the atoms to evaporate while keeping the amorphous material with a high density respectively. The final modification step consists of creating the pattern by deleting some of the amorphous atoms. This was accomplished using the delete particle modification in the OVITO software tool [39]. The end result is a single crystal substrate structure with four amorphous walls on top of it as observed in Fig. 2.3.c that can later be used as a substrate structure for a selective epitaxial growth simulation.

The initial substrate configuration for a selective area growth simulation is illustrated in Fig. 2.3.a. The amorphous mask walls are placed on top of the CdS substrate and the position of the atoms that form these walls are fixed throughout the duration of a growth simulation in order to preserve their structure. All other simulation settings are the same as those used in a planar

growth described before. Figs. 2.3.a-c illustrate cross-sectional images a selective epitaxial growth of  $\text{Cd}_{(1-x)}\text{Zn}_x\text{Te}$  at different time steps of the simulation. The semi-transparent red boxes surround the substrate monolayers that were fixed to prevent substrate drift. The semi-transparent green boxes surround the atoms inside the isothermal region.



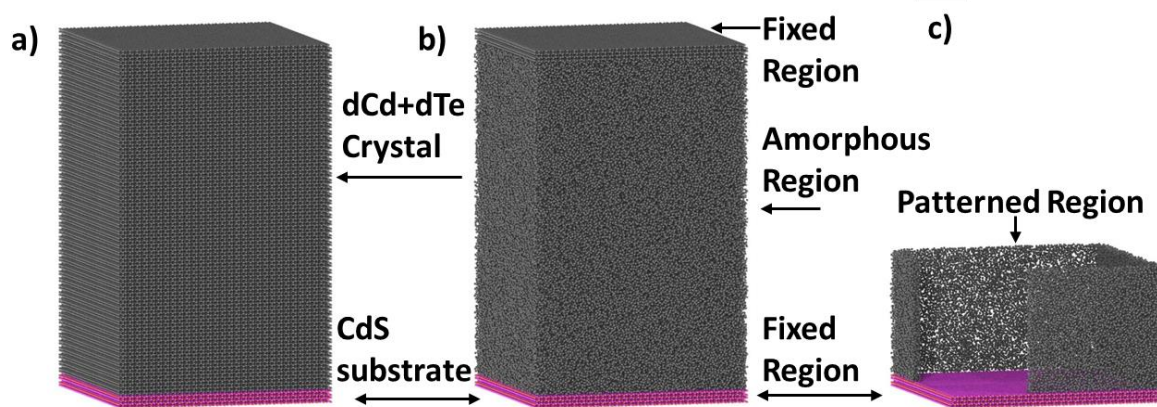


Figure 2.2: Illustration of the steps required to create an amorphous mask for use in selective area growth simulations.

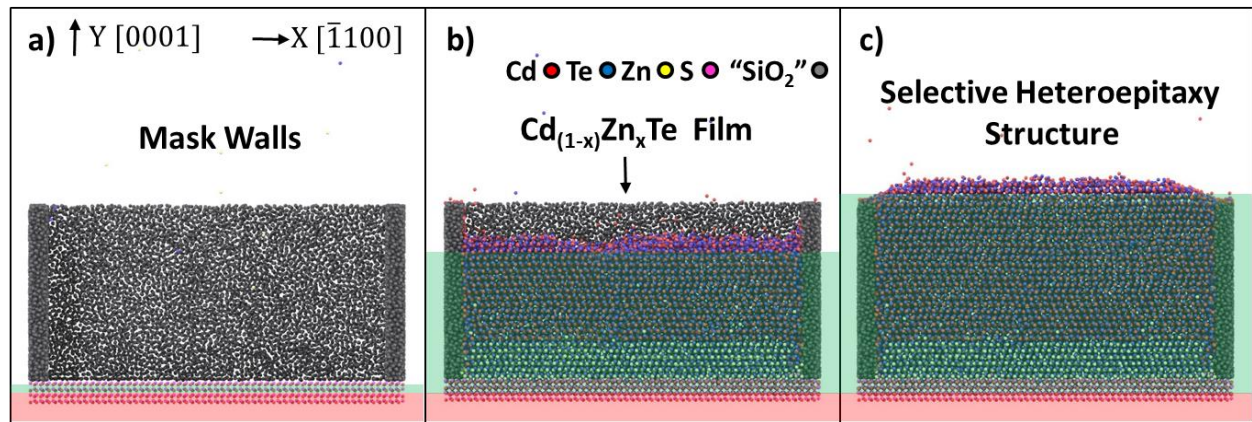


Figure 2.3: Sequence of images illustrate the simulated selective heteroepitaxy configuration.

### 2.1.3 Post-Deposition Treatment Simulations

Following the deposition of a film in an epitaxial growth simulation, the energy of the system is high due to the combination of the isothermal region temperature and the energy of the adatom impact on the substrate's surface. Under these conditions, the atoms in the system experience small vibrations at their lattice site as seen in Fig. 2.4.a for a CdTe film. These vibrations can hinder the accurate characterization of the attained structure through visual inspection and the use structural analysis algorithms. In order to overcome this obstacle, two post-deposition treatment simulations were applied to each film growth data.

The first post-deposition treatment consisted of an annealing simulation of 1,000,000 time steps at the deposition temperature in order to allow system particles additional time to reach a low energy configuration. During this treatment no more adatoms were added. Fig. 2.4.b shows the effect of the CdTe film after the anneal treatment. The atomic vibrations for the system have decreased and it becomes easier to identify lattice sites. The second post-deposition treatment consisted of an energy minimization simulation. This procedure is similar to cooling a sample to 0 K so that the atoms reach their lowest energy configuration. Fig. 2.4.c shows the CdTe film after annealing and energy minimization treatments, it can be seen that the atomic vibrations have reduced drastically and the lattice sites can be clearly identified. The application of these post-processing steps helped to visually identify structures in the films grown but it also increased the accuracy of the structural identification algorithms discussed in the next subsection.

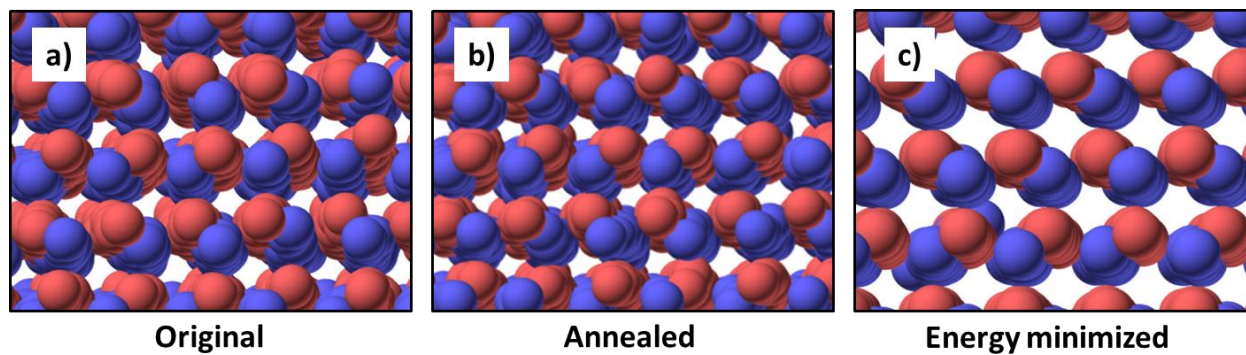


Figure 2.4: Visualization of a CdTe film: a) after deposition, b) after annealing simulation, and c) after annealing and energy minimization post-treatment steps.

## **2.2 Post-Processing Analysis Tools**

Molecular dynamics simulations provide a data set that contains a large amount of three-dimensional atomistic information about the material system being studied. The use of powerful and versatile visualization and analysis tools allows researchers to better interpret and characterize these results in order to maximize the critical analysis information that can be learned from a study. The tools that were employed in this study are described in the following sub-sections.

### **2.2.1 OVITO: The Open Visualization Tool**

This tool was developed and is maintained by Alexander Stukowski from the Darmstadt University of Technology, Germany. OVITO [39] is a scientific visualization and analysis software that is used to process atomistic simulation data. The tool is also Open Source and is available for all major operating systems.

OVITO was employed in this work because of its ample flexibility that allows for the implementation of multiple analyses methodologies and also allows for the rendering of high quality images (all structure and defect visualizations in this document were produced using this tool). OVITO is also able to open LAMMPS and Crystal Analysis Tool files directly, which makes it convenient because a single visualization tool was employed for this work. OVITO version 2.4.4 was used in this work.

### **2.2.2 Strategies for Defect Detection in Atomistic Data**

There are several strategies for the use of software analysis tools to examine lattice structures and detect defects in crystalline materials. Each method has strengths and weaknesses [40] [41] that drive the choice of a particular analysis tool to be determined by the problem that needs to be studied. In this work, the detection of lattice defects was handled by employing the Crystal Analysis Tool (CAT) [41] [42] [43], developed also by A. Stukowski. The CAT version used was that of December 10, 2014.

CAT is a fully automated software that reads in atomistic data files and performs a comprehensive analysis of the structural composition via advanced algorithms to identify crystalline phases, dislocation lines, and even grain boundaries contained within the data. The complete description of the numerous methodologies implemented in this software package can be found in these reference papers [42] [43]. The major steps involved in the extraction of defects from an atomistic data set are illustrated in Fig. 2.5 for the case of dislocation lines inside a CdTe/CdS heterostructure.

Fig. 2.5.a shows the initial phase in the algorithm which consists of the separation of atoms into clusters of ordered and disordered atoms. In order to achieve this, the local structure of each atom in the data set needs to be identified by using a structure identification algorithm that matches atomistic data to a catalog of known template structures [42]. The ordered atoms are then grouped into clusters. The next step in the defect analysis algorithm consists of connecting each atom to its nearest neighbors with a bond vector between each neighbor pair (Fig.2.5.b), effectively creating a tetrahedral mesh. Each tetrahedron edge is then compared to a reference vector. A good tetrahedron is one in which all edges match the reference, if at least one edge differs from the reference the tetrahedron is considered bad. The next step is shown in the schematic in Fig. 2.5.c and involves creating an interface mesh between the bad and good material. Afterwards, the algorithm traces Burgers circuits along the interface mesh until a non-zero Burgers vector is found. Once this happens, one more Burgers circuit is created at that location and advances in the opposite direction than the first. Both circuits continue advancing along the interface mesh while producing a graphic representation of the dislocation line (Fig. 2.5.d). This step is repeated until all dislocation segments in the data file are found.

The catalog of template structures plays a major role in the CAT's ability to capture lattice distortions. Having the proper template structures ensures that the analysis will effectively detect lattices, planar defects and point defects. The CAT can detect many of the common lattices which include FCC, HCP, BCC, diamond, hexagonal diamond, among others [42]. The lattice patterns employed for the analyses in this work were the diamond and hexagonal diamond

lattice patterns. These lattice structures are analogous to the zinc blende and wurtzite lattice structures respectively, that are commonly observed in alloys and compounds containing the Cd, Te, Zn, and S. The difference between the analogous structures is that the former pair contain only a single atom type (for example the Si lattice), while the later pair contain two or more atoms types (such as in the case of CdTe or  $\text{Cd}_{(1-x)}\text{Zn}_x\text{Te}$ ). This means the CAT can provide information about the structural composition of the simulation data based on the position of the atoms. However, because the algorithms employed for structural pattern matching don't simultaneously account for the position and elemental composition of each atom, defects such as substitutionals and dislocation cores can't be properly identified using this methodology alone. Sub-section 2.2.4 discusses a proposed methodology to aid in overcoming this limitation.

The structure identification method employed in this work was the common neighbor analysis (CNA) algorithm for diamond and hexagonal diamond structures. More information about the common neighbor analysis is found in Appendix B. Table 2.1 lists the lattice and defect pattern templates that were employed. The normal font pattern templates names in Table 2.1 indicate the files that were originally included with the tool. The italicized name in the table is a new pattern file that was created in this work to expand the CAT defect detection capabilities for hexagonal diamond based defects. The creation of this file consisted of exploiting the structural similarities between hexagonal diamond, diamond lattice and their corresponding defect structures in order to reuse the information from the original diamond CAT pattern files. These files define a defect structure that is surrounded by diamond structure atoms. In the new pattern files, the defect structure is defined as being surrounded by hexagonal diamond structure atoms instead. This change creates pattern files that effectively identify hexagonal diamond based defects and extract lattice defect information. An evaluation of the defect patterns was performed in order to learn how each defect pattern is associated with the Burgers vectors it identifies and the dislocation lines it generates. This evaluation also served to identify which dislocation patterns should be used during each analysis in order to optimize the defects that can

be detected. Details about the defect structure models and their evaluation can be found in Appendix A.



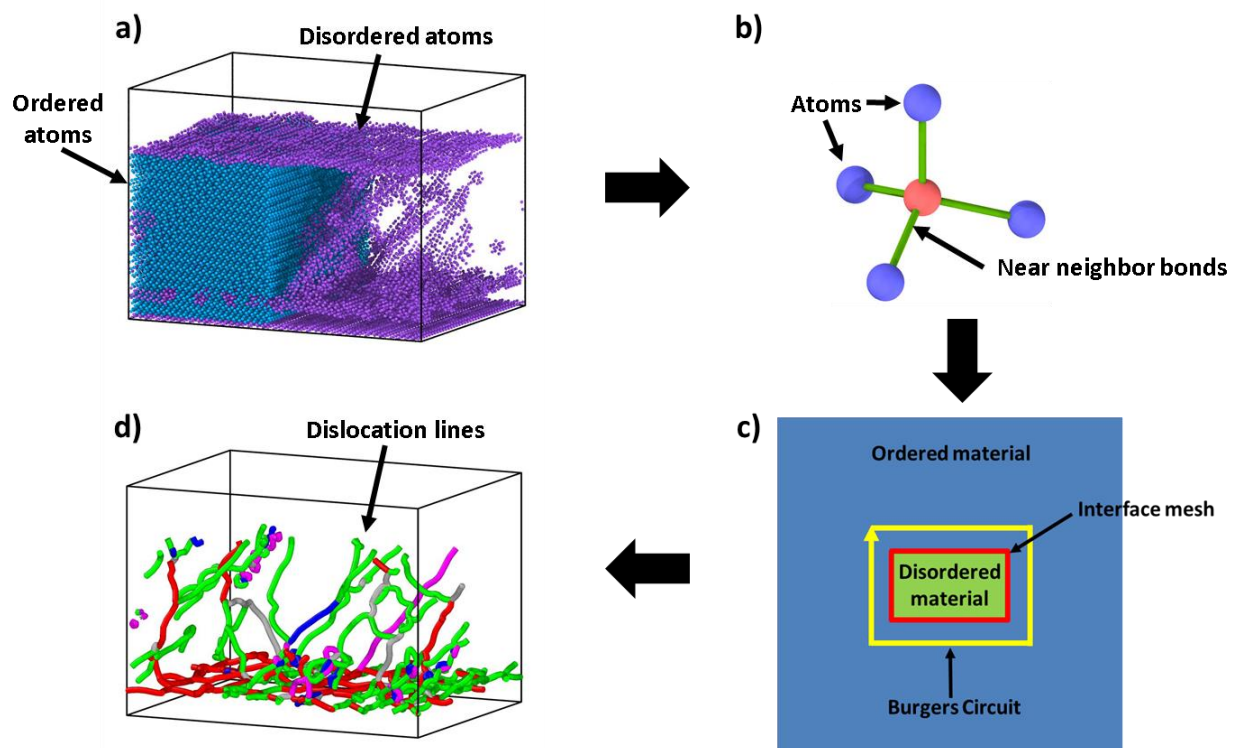


Figure 2.5: Illustration of the steps followed by the Crystal Analysis Tool for the defect information extraction from an atomistic data set of CdTe/CdS heterostructure. Adapted from [43].

Table 2.1: List of employed Crystal Analysis Tool lattice and defect patterns.

<b>Lattice Patterns</b>	<b>Defect Patterns</b>
Diamond	Coherent $\Sigma 3$ twin boundary
	Intrinsic stacking fault
	Triple stacking fault
Hexagonal diamond	<i>Intrinsic stacking fault</i>

### 2.2.3 Zinc Blende and Wurtzite Dislocation Systems

It is well known that the material compounds of CdTe, ZnTe, CdS and their alloys can crystallize in the form of wurtzite and zinc blende crystal lattices. In simulated thin film growth domains of both crystal structures are often observed within a sample, even when grown on a single crystal substrate. The reason behind this is the structural similarity of the closed-packed planes between the two structures that happen to also be aligned with the preferred growth orientation of these materials, making the phase transition a likely occurrence. For example a grain with zinc blende structure that has a growth orientation aligned with the [111] will have a layer stacking sequence of AaBbCcAa... and can experience stacking faults that can easily change the stacking sequence to AaBbAaBb... which is indicative of the wurtzite lattice with a growth orientation aligned along the [0001]. Because this domain transition is a common occurrence, the presence of both wurtzite and zinc blende structures can be expected inside an epilayer.

Figure 2.6 illustrates the top view of a closed-packed plain along with the orientation axes and unit cells for wurtzite and zinc blende systems. The wurtzite unit cell basal plane is shown as the green parallelepiped (where  $a_w$  is the a-lattice parameter). A segment of the triangular geometry associated to zinc blende closed-packed planes is outlined using a blue triangle for reference (where  $a_{z.b.}$  is the lattice parameter). The types of dislocations that can occur in this plane are also illustrated as arrows. The perfect/full dislocations that can occur in these planes are associated with a Burgers vector,  $\vec{b}$ , of  $\frac{1}{\sqrt{3}} \langle 1120 \rangle$  or  $\frac{1}{\sqrt{2}} \langle 110 \rangle$ , respectively for hexagonal and cubic structure systems and it is illustrated with the black arrow. The partial dislocations that can occur on these planes, known as Shockley partials, are illustrated with the red arrows. The dislocation reactions that generate these partial dislocations are the following:

$$\frac{1}{\sqrt{3}} \langle 1120 \rangle \rightarrow \frac{1}{\sqrt{3}} \langle 1010 \rangle + \frac{1}{\sqrt{3}} \langle 0110 \rangle, \text{ for hexagonal systems.}$$

$$\frac{1}{\sqrt{2}} \langle 110 \rangle \rightarrow \frac{1}{\sqrt{6}} \langle 211 \rangle + \frac{1}{\sqrt{6}} \langle 121 \rangle, \text{ for cubic systems.}$$

These Burgers vectors are found inside a simulation data set by the CAT based on the structural template defect models specified during an analysis. Only one lattice structure can be used as a reference at a given time therefore it was necessary to analyze each data set twice, once for zinc blende based analysis and another for wurtzite structures. Two different dislocation network profiles are produced with variations of Burgers vectors, dislocation line length, dislocation density, dislocation location, etc. Fig. 2.7 shows the visualization of the two dislocation profiles obtained by analyzing a planar CdTe film grown on CdS (0001) (this was the simulation that contained the most defects from all others in this work). Fig. 2.7.a is an atomistic visualization of the CdTe/CdS heterojunction. Fig. 2.7.b is a visualization of the zinc blende dislocation lines detected inside the CdTe epilayer. Fig 2.7.c is a visualization of the wurtzite dislocation lines detected inside the CdTe epilayer. Comparison between the two dislocation profiles in this figure reveals several differences, in particular the dislocation location in reference to the CdTe/CdS interface. It can be seen that wurtzite based dislocations are shorter in length, but are more numerous and form a complex network close to the interface. In contrast, dislocations associated with zinc blende structure are further away from the interface, closer to the film's surface, and their dislocation line segments are longer.

Fig. 2.8 is a top view illustration of both dislocation network profiles and offers another perspective in which the dislocation line layout across the substrate surface can be observed in greater detail. In Fig. 2.8.b, the short dislocation line segments are located at the interface, and connect in high frequency in a way that resembles triangles, hexagons, etc. In comparison, the dislocation line segments shown in Fig. 2.8.a are longer, rarely form junctions, and they appear to have random geometries when they do connect to other segments. The colors of the dislocation lines in Fig. 2.8 and Fig. 2.7 help to distinguish the several different types of dislocations detected in the data set by using their respective Burgers vector (see Table 2.2 for color index). The total dislocation line length in a system was calculated by adding the dislocation length of both dislocation profiles.

The reason why wurtzite dislocations appear in great numbers near the interface could be that the wurtzite single crystal substrate ensures that defects formed by the first film monolayers are surrounded by wurtzite lattice atoms. Because of the surrounding wurtzite lattice structure, the CAT would associate the defects found in this region to the wurtzite defect models, and thus the dislocation lines are assigned a wurtzite lattice Burgers vector. Fig. 2.9.a shows a cross-section visualization along the vertical axis of the film near the interface after a structure analysis algorithm was applied to the data. This image shows grain boundaries (orange atoms) forming along the interface plane that connect to each other in similar geometries to the dislocation network shown in Fig. 2.7.b. The grain boundaries in Fig. 2.9.a surround single crystal grains, which are mostly wurtzite (in the image shown as red and what appears to be purple in some grains because of the small image size) as well as fewer zinc blende grains (light blue). As the analysis moves away from the interface, the lattice structure environment changes to either wurtzite or zinc blende. Fig. 2.9.b is also a cross-section image along the vertical axis, but this time the cut was made in a region close the center of the film. The grain boundaries in this image have become longer, have more separation between them and the grains increase in size when compared to structure at the interface. The reason why the zinc blende dislocations are closer to the surface is also shown in Fig. 2.9.b since away from the interface more zinc blende grains (light blue) are found in this region, thus the CAT classifies them as zinc blende defects.

The various Burgers vector families detected by CAT are listed in Table 2.2. The table is also sorted by total dislocation length in decreasing order from the top. The zinc blende Burgers vectors associated with the Shockley partial dislocation were found to have the longest total dislocation line length, followed with a large margin (~10 times less) by the full dislocation. The reason why these types of defects are favored is that they have Burgers vectors that lie on the closed-packed plane of the zinc blende lattice. By definition the atoms in this plane encounter the smallest displacements required for slip, and therefore dislocations associated with these Burgers vectors are more likely to occur because they are energetically favorable. Similarly, the longest dislocation line length that is associated with wurtzite Burgers vector was the  $\frac{1}{3} < 1010 >$

(Shockley Partial), followed closely by the  $\frac{1}{3} \langle 1\ 1\ 2\ 0 \rangle$  (Full Dislocation) and  $\frac{1}{3} \langle 0\ 1\ 1\ 0 \rangle$  (Shockley Partial) dislocation line types.



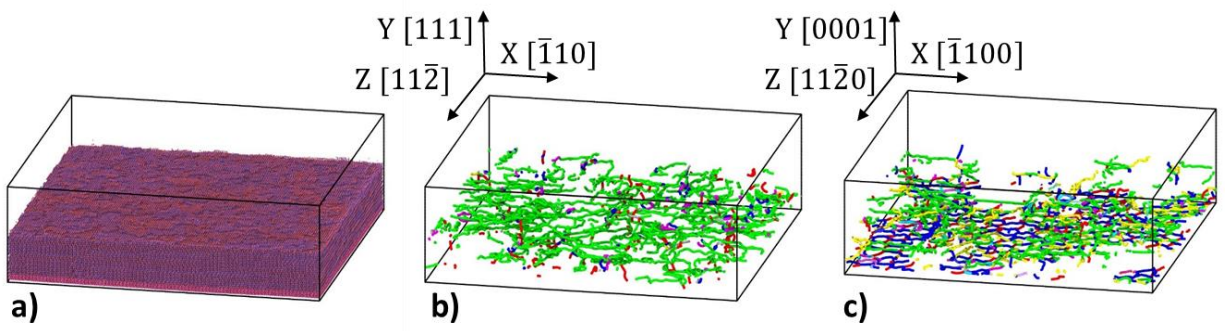


Figure 2.7: a) Atomistic visualization of the CdTe/CdS heterojunction. b) Visualization of the wurtzite dislocation lines detected inside the CdTe epilayer. c) Visualization of the zinc blende dislocation lines detected inside the CdTe epilayer.



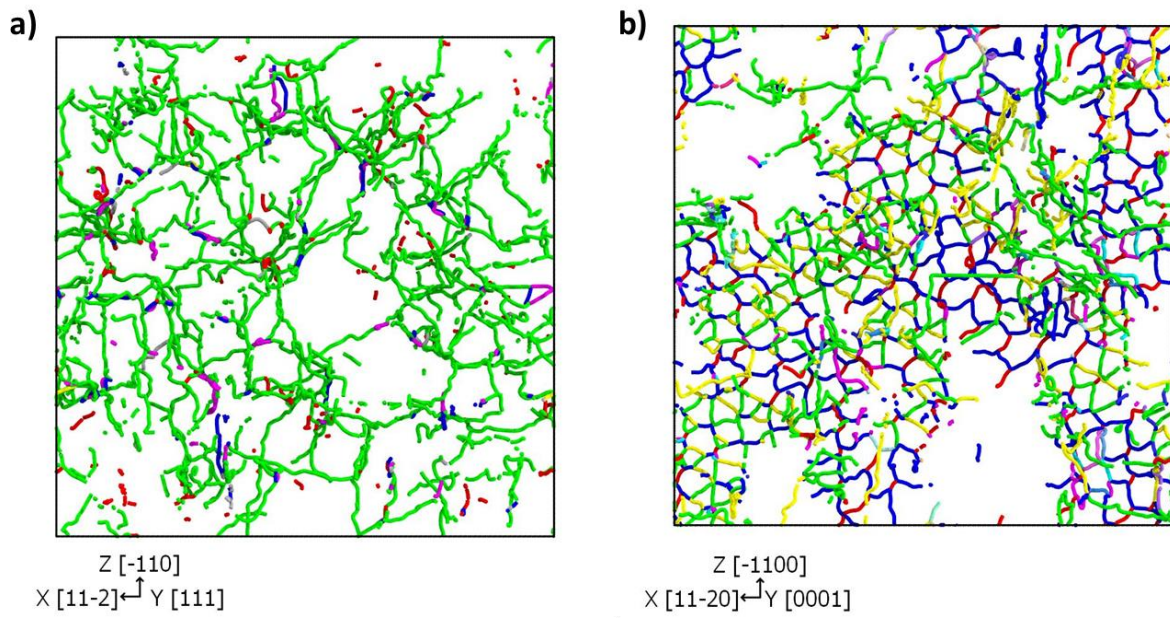


Figure 2.8: a) Top view visualization of the wurtzite dislocation lines detected inside the CdTe epilayer. b) Top view visualization of the zinc blende dislocation lines detected inside the CdTe epilayer.

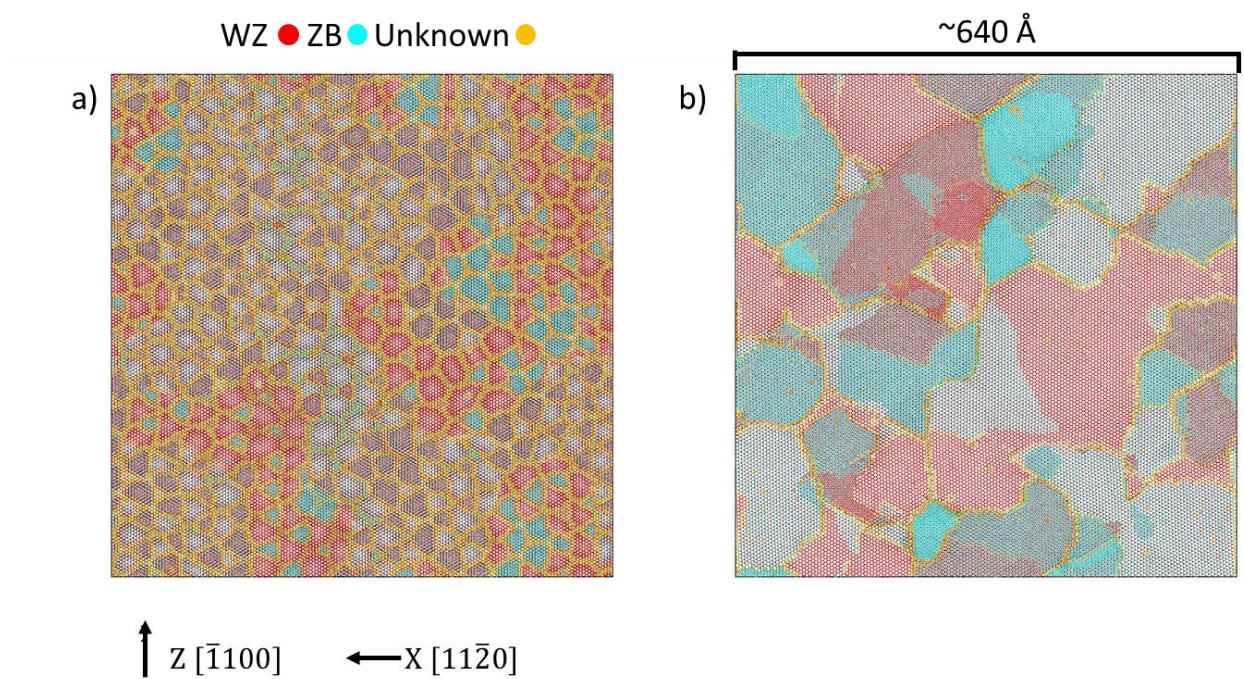


Figure 2.9: a) Top view cross-section visualization lattice structures along the vertical axis a) at the interface b) at the center of the film.

Table 2.2: List of detected Burgers vectors detected by the Crystal Analysis tool using the zinc blende (diamond) and wurtzite (hexagonal diamond) structure patterns.

Zinc Blende Burgers Vector Family	Wurtzite Burgers Vector Family
$\frac{1}{6}\langle 1\ 1\ 2 \rangle$ (Shockley Partial)	$\frac{1}{3}\langle 1\ 0\ 1\ 0 \rangle$ (Shockley Partial)
$\frac{1}{2}\langle 1\ 1\ 0 \rangle$ (Full Dislocation)	$\frac{1}{3}\langle 1\ 1\ 2\ 0 \rangle$ (Full Dislocation)
$\frac{1}{4}\langle 1\ 1\ 1 \rangle$ Partial	$\frac{1}{3}\langle 0\ 1\ 1\ 0 \rangle$ (Shockley Partial)
$\frac{1}{12}\langle 1\ 1\ 1 \rangle$ Partial	$\langle 0\ 0\ 0\ 1 \rangle$ (Full Dislocation)
$\frac{1}{3}\langle 0\ 0\ 1 \rangle$ (Hirth Partial)	$\frac{1}{12}\langle 0\ 0\ 0\ 1 \rangle$ (Frank Partial)
$\frac{1}{3}\langle 1\ 1\ 1 \rangle$ (Frank Partial)	$\frac{1}{12}\langle 0\ 0\ 0\ 1 \rangle$ (Frank Partial)
$\frac{1}{6}\langle 1\ 1\ 0 \rangle$ (Stair-rod)	$\frac{2}{3}\langle 1\ 0\ 1\ 0 \rangle$ (Shockley Partial)

## 2.2.4 Simulated Defect Structure Validation

Validation of the defect structures detected by the CAT was achieved by comparing experimental cross-section scanning transmission electron microscope (STEM) images of CdTe films grown on polycrystalline CdS. Li, et al. [16] have reported a number of defect structures including stacking faults, Shockley partial dislocations, Frank partial dislocations, among others. In Fig. 2.9.b, Fig. 2.9.c and Fig. 2.9.d Z-contrast was employed to identify the elemental composition of the atoms in the TEM images by comparing the different image intensities given off by each element, such that the atoms surrounded by the yellow circle are Te while those circled in blue are Cd. Fig. 2.9.b shows a cross-sectional TEM image of CdTe closed-packed planes viewed from the  $[110]$  direction in which the AaBbCc... stacking order characteristic of the zinc blende lattice can be observed. Stacking faults can also be seen in the image and are indicated by the black arrows on the side. Fig. 2.9.a shows a cross-section atomistic visualization of a simulated CdTe film grown on CdS (0001)A (meaning that the substrate terminated in a Cd monolayer) in which the yellow circles indicate Te and blue Cd atoms. The stacking faults in this image are indicated by the red arrows on the side. A comparison between Fig. 2.9.a and Fig 2.9.b reveals that the simulated film's stacking fault presence is in very good agreement with the experimental result.

Fig. 2.9.c illustrates the Burgers circuit built around a two layer  $30^\circ$  Shockley partial. Two dislocation cores can also be observed in each figure and consist of a single Cd atom, although Te cores were also reported [16]. Fig. 2.9.e shows a cross-section visualization of defect structures inside the simulated CdTe film. The Burgers circuits in Fig. 2.9.e surround  $90^\circ$  Shockley partials with single Te atoms dislocation cores. Similarly, Fig. 2.9.c illustrates a Burgers circuit around a two layer  $90^\circ$  Shockley partial in a TEM image. Fig. 2.9.f shows a cross-section visualization in which the Burgers circuit surrounds another  $90^\circ$  Shockley partial. The dislocation core in this case consists of two pair of opposing dumbbells, in each of which incorrect bonding occurs. The top faulted dumbbell pair has Te-Te bonding, while the bottom faulted pair has Cd-Cd bonds. Below these two faulted dumbbells, there is one more defect that

can be observed and it consists of a Cd atom that has bonded to two Te atoms forming what appears to be a twin dumbbell. Li, et al. discussed the possibility of the opposing dumbbell dislocation core existing, but were unable to observe it in detail due to it being unstable, and disappearing when it was under the microscope's beam.

The defect structure comparison between experimental and simulated growths shows that the defects predicted by the molecular dynamics thin film growth simulations are in very good agreement with the experimental data reported in literature. In addition, the combination of defect structure algorithms and high resolution visualization software employed in this work can offer unprecedented insight into structural defect information that cannot be easily obtained through experimental efforts alone due to numerous challenges of characterization.

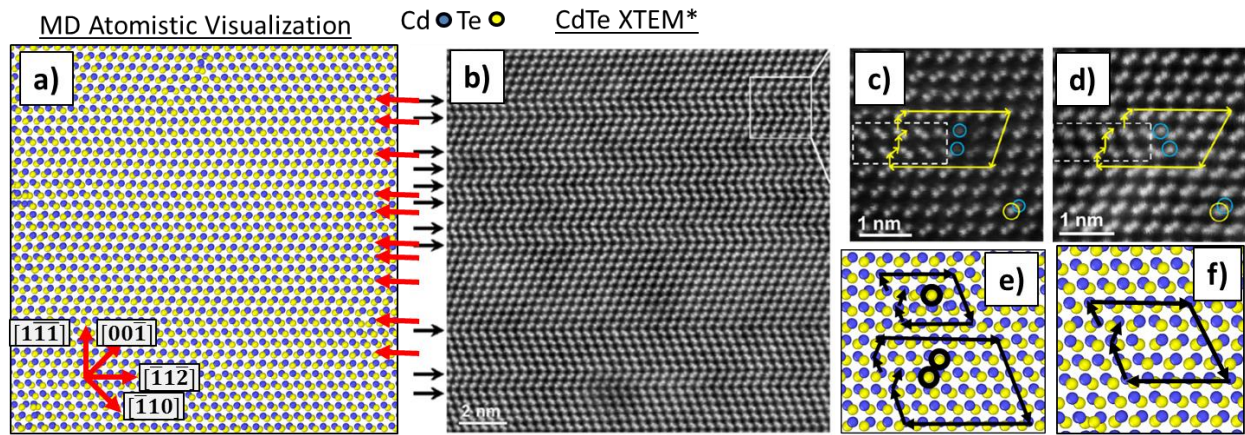


Figure 2.9: Structural defect comparison between simulated and experimental CdTe growths validates MD modeling approach. a) shows the simulation stacking fault frequency in very good agreement with the experimental image b). Figures e-f) are simulated dislocation core structures in good relation with the results reported in literature (Figures c-d). Experimental images from Li, et al. [16]



## 2.3 Design of Experimental Procedures

This section describes the multiple experiments designed to study the simulated planar and selective thin film growth while combining the methodologies discussed in the previous section.

### 2.3.1 Study of Deposition Temperature

This set of experiments was designed to determine the optimal deposition temperature to be used during the epitaxial growth of a given material under certain substrate conditions. The ideal deposition temperature in each case was the value at which the film was crystalline material and contained the smallest total length of dislocation lines.

The planar deposition cases studied were CdTe, ZnTe, and CdTe/ZnTe bilayer grown on CdS (0001) substrates. The deposition conditions follow the procedure described in sub-section 2.1.1. The CdS substrate measured  $\sim 214$  Å,  $\sim 14$  Å, and  $\sim 214$  Å in the x, y, and z dimensions respectively. The total number of time steps for these simulations was 15,000,000 which resulted in a film thickness of  $\sim 150$  Å. The calculated deposition rate was defined as the ratio of the final film thickness over the simulated time and was calculated to be  $\sim 0.0025$  Å/ps. The number of particles in a system of these dimensions was  $\sim 225,000$  atoms. This simulation size was considered ideal for most of the simulations in this work because the computing time required was 60 hours while using 80 computing cores, which was a reasonable amount of time given the computer resources available for this study.

The first case studied was that of the planar CdTe/ZnTe bilayer grown on CdS. One of the goals in these simulations was to grow a ZnTe buffer layer that was  $\sim 30$  Å thick ( $\sim 1/5$  of the total epilayer thickness). This was achieved by setting the elemental vapor composition to ZnTe initially, and then switching it to CdTe during growth at a time determined using the calculated deposition rate. This configuration was used for the following range of temperatures: 600 K, 800 K, 1000 K, 1200 K, 1400 K, 1600 K, 1800 K, and 2000 K. This broad range of temperatures was initially used to identify a more focused range of values that result in films grown with small

defect densities. Three simulations were produced for each temperature value. The final results were then post-processed using the techniques discussed in sub-section 2.1.3. Following post-deposition treatments, the atomistic data was analyzed using the CAT, and the results for each temperature value were averaged. The processing steps described in this and the previous paragraph were used in all simulations unless otherwise stated.

The next cases studied were planar CdTe on CdS and ZnTe on CdS. In these cases the elemental vapor composition remained fixed during the growth. The range of temperatures was also reduced by focusing only in the range of temperatures with lower defect density observed for the CdTe/ZnTe bilayer simulations. Reducing the range of temperatures studied also decreased the amount of data that needed to be analyzed and allowed for the limited computing resources to be used in more critical simulations.

The optimal deposition temperature for selective area growths was studied for the CdTe on CdS and the CdTe/ZnTe bilayer on CdS cases. The substrate configuration used was that described in sub-section 2.1.2. The mask walls were  $\sim 10$  Å thick and  $\sim 100$  Å tall for all selective growth simulations. The targeted epilayer thickness was  $\sim 100$  Å and the average number of particles in these systems was  $\sim 180,000$  atoms. The computational load for these simulations increased because of the large number of atoms that formed the mask walls. The computing time for these simulations was 96 hours while using 80 processing cores.

The actual substrate temperature for all simulations was monitored using LAMMPS in order to obtain an accurate reading of the temperature of the system since targeted temperature value was not truly achieved during a simulation.

### **2.3.2 Study of Selective Area Growth**

The selective area growth study was designed to observe the effect of the island dimensions in the defect density present within the epilayer during a CdTe on CdS growth. The selective area configuration used was that described in sub-section 2.1.2. Three different island sizes were studied:  $\sim 214$  Å,  $\sim 430$  Å, and  $\sim 640$  Å. Table 2.3 compares the average number of



particles, computing time, and number of computing cores employed in each of the different island size simulations. In addition, planar growths of CdTe on CdS with a substrate size of  $\sim 640$  Å were performed under the same deposition conditions for direct comparison to the island of the same size. The planar simulation data was used for the CAT examples discussed in subsection 2.2.3.

### **2.3.3 Study of Zn Alloying**

This set of experiments was designed to learn what Zn alloy profile more efficiently reduced the defect density in the CdTe epilayer. These simulations used the bilayer configuration discussed in sub-section 2.3.1, but this time the elemental vapor composition of the buffer layer was varied. The targeted compositions of the buffer layer were: CdTe,  $\text{Cd}_{0.8}\text{Zn}_{0.2}\text{Te}$ ,  $\text{Cd}_{0.6}\text{Zn}_{0.4}\text{Te}$ ,  $\text{Cd}_{0.4}\text{Zn}_{0.6}\text{Te}$ ,  $\text{Cd}_{0.2}\text{Zn}_{0.8}\text{Te}$ , and ZnTe.

Simulations that combined selective area and Zn alloy growth used the selective area configuration described in sub-section 2.1.2 and also incorporated the bilayer configuration discussed in the previous paragraph. A cross-section atomistic visualization for the selective CdTe/ZnTe on CdS growth can be observed in Fig. 2.3.

Table 2.3: Comparison of system size, computing time, and computing cores used for the three different island sizes studied.

<b>Island Size (Å)</b>	<b>Avg. Number of Particles</b>	<b>Avg. Computing Time (hours)</b>	<b>Number of computing cores</b>
~214	~180,000	96	80
~430	~650,000	96	144
~640	~1,500,000	192	144
~640 (Planar)	~1,500,000	192	144

## Chapter 3: Results

The following section reports the results obtained for the experiments described in chapter 2. The average dislocation densities calculated for different epilayer growth configurations are reported. Visualization of selected structures and dislocation profiles are also presented to aid in understanding the data interpretation.

### 3.1 Effect of Deposition Temperature on Defect Density

The following sub-sections report the defect data detected using the CAT for the simulations used to study the effect of deposition temperature on defect density. The dislocation information obtained for each data set consisted of the sum of the zinc blende data plus the wurtzite data (refer to sub-section 2.2.3). Each plot has been normalized by the volume of the system.

#### 3.1.1 Optimal Deposition Temperature for Planar CdTe / ZnTe bilayer on CdS

Fig. 3.1 plots the dislocation data detected inside the CdTe/ZnTe on CdS simulations performed over a wide range of temperatures. At low temperatures, adatoms land on the substrate and remain stuck in that position because they lack the energy to move into a lower energy configuration. As a consequence, the films grown at low temperatures have low crystallinity and a large presence of dislocations, in good agreement with the experimental observations [7] in which low deposition temperature films exhibited a high density of intra-grain dislocations. Fig. 3.2.a shows the cross-section of a CdTe/ZnTe/CdS sample grown at a target deposition temperature of 600 K. The image shows that a large amount of disordered atoms are present, which can be associated with grain boundaries and defects. Fig. 3.2.b shows the cross-section of a sample grown at a target deposition temperature of 1400 K. The number of disordered atoms has decreased, and more zinc blende and wurtzite atoms can be seen indicating that the film crystallinity has increased.

In contrast, films grown at high temperatures (beyond the CdTe melting point) exhibit little to almost no crystallinity since the system has very high energy, which causes the substrate

and adatoms to be unable to nucleate and remain in an ordered arrangement. The CAT analysis was unable to find crystalline material inside these high temperature growths, and consequently no dislocation information was detected inside them (these values were omitted from Fig. 3.1).

As discussed previously in the design of experiment, the system temperature was monitored throughout the simulation in order to get a more accurate idea of the growth conditions. Table 2.4 compares the simulation target temperature values with the actual values. The measured temperature values were used for Fig. 3.1.

The trend observed was that film crystallinity increases as the substrate temperature approaches the melting point of CdTe (1314 K). From the plot of Fig. 3.1 the optimal deposition temperature for the CdTe/ZnTe bilayer grown on CdS was determined to be ~1284 K (target temperature of 1400 K). The trend observed in these experiments was that film crystallinity increases when the deposition temperature is closest to the CdTe melting point.

Table 2.4: Comparison between simulation target temperature and actual average temperature for CdTe/ZnTe bilayer on CdS.

<b>Target Temperature (K)</b>	<b>Avg. Measured Temperature (K)</b>
600	564
800	743
1000	923
1200	1102
1400	1284
1600	1472
1800	1665
2000	1854

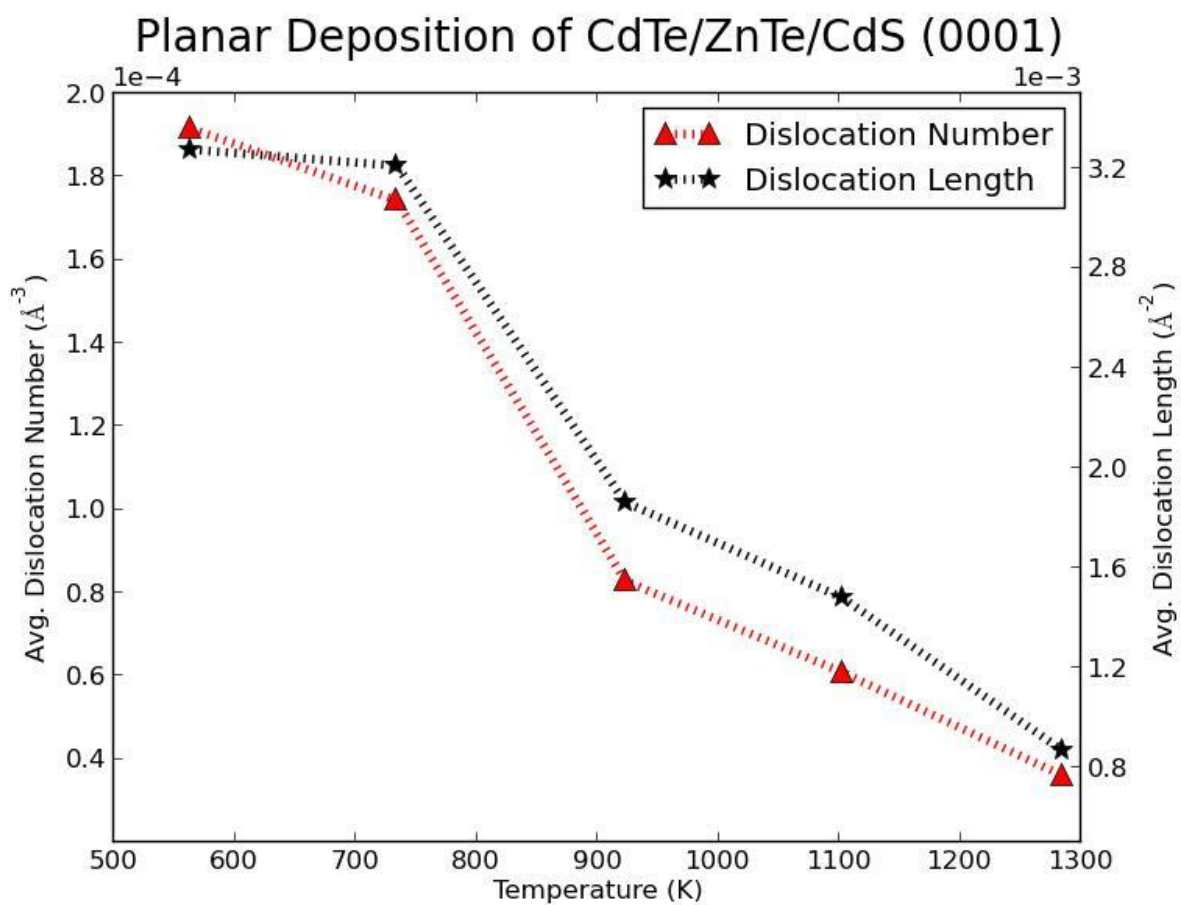


Figure 3.1: Plot of dislocation densities for planar CdTe / ZnTe / CdS at several deposition temperatures.

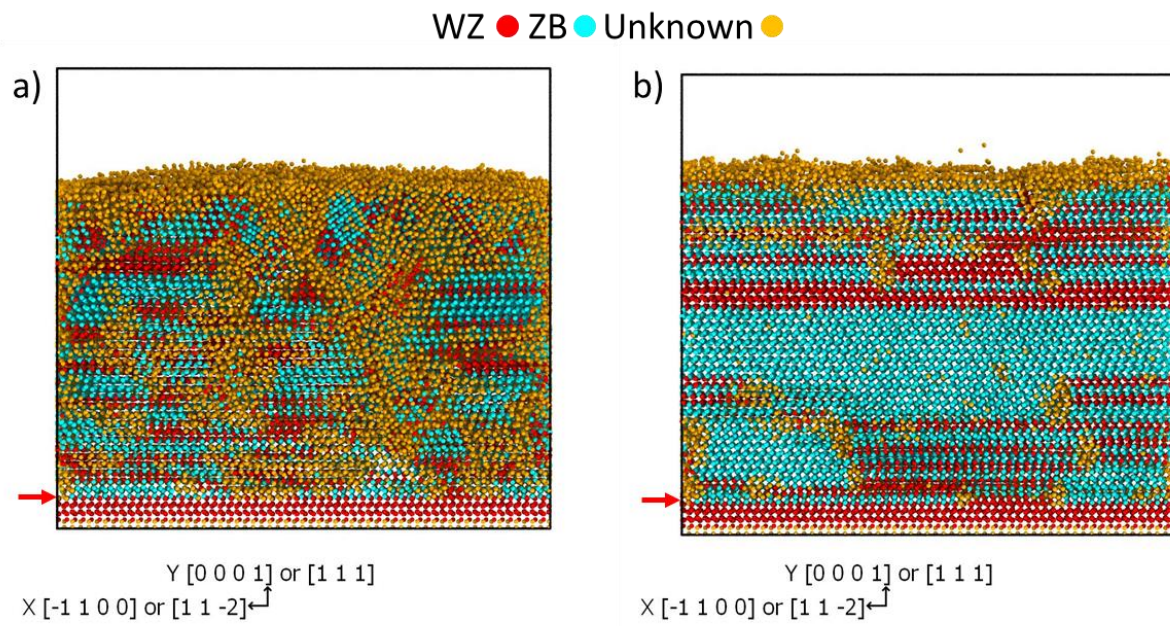


Figure 3.2: Structure analysis visualization for CdTe/ZnTe layers grown on CdS at a) 600 K and b) 1400 K target deposition temperatures. The red arrows serve to indicate the interface between the film and substrate.

### **3.1.2 Optimal Deposition Temperature for Planar CdTe on CdS**

The plot in Fig. 3.3 shows the defect information for the planar CdTe on CdS depositions performed over a range of temperatures shown in Table 2.5. Similarly to the previous case, the optimal deposition temperature for the planar CdTe grown on CdS was determined to be ~1294 K (target temperature of 1400 K). The trend observed here was also that film crystallinity improved as the substrate temperature approached the melting point of CdTe (1314 K). Simulations with temperatures beyond the melting point resulted in amorphous growths and were omitted from defect analyses.



Table 2.5: Comparison between simulation target temperature and actual average temperature for planar CdTe on CdS.

<b>Target Temperature (K)</b>	<b>Avg. Measured Temperature (K)</b>
1200	1111
1300	1203
1400	1294
1500	1388

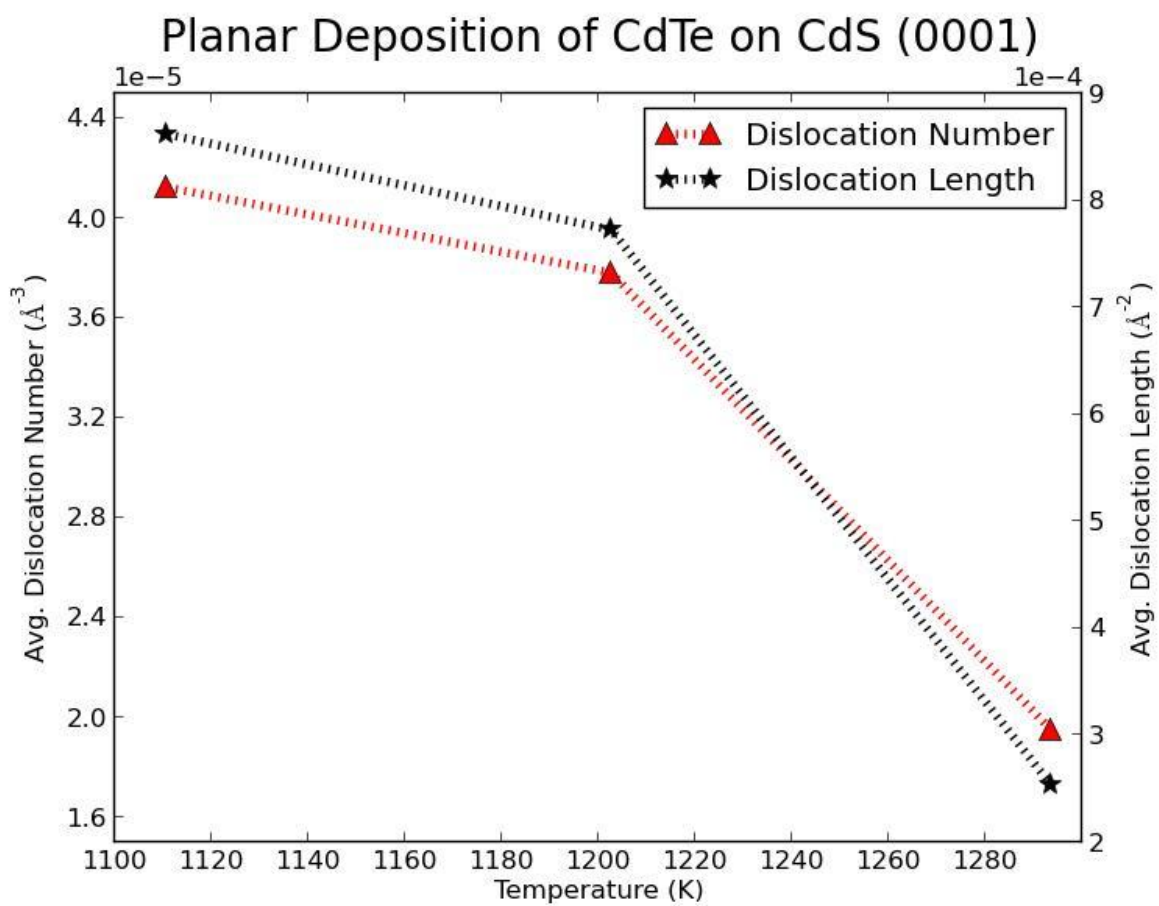


Figure 3.3: Plot of dislocation densities for planar CdTe on CdS at several deposition temperatures.

### **3.1.3 Optimal Deposition Temperature for Planar ZnTe on CdS**

The defects analyses results for the planar ZnTe on CdS planar can be seen in Fig. 3.4. The range of temperatures used during the simulations is shown in Table 2.6. The previous trends were observed in these experiments also, film crystallinity increased as the substrate temperature approached the melting point of ZnTe (1511 K). The films grown beyond the ZnTe melting point exhibited low crystallinity and were omitted from the analyses. The deposition temperature that resulted in less defects was ~1450 K (target temperature of 1600K).

Table 2.6: Comparison between simulation target temperature and actual average temperature for planar ZnTe on CdS.

<b>Target Temperature (K)</b>	<b>Avg. Measured Temperature (K)</b>
1200	1093
1400	1271
1600	1450
1800	1646

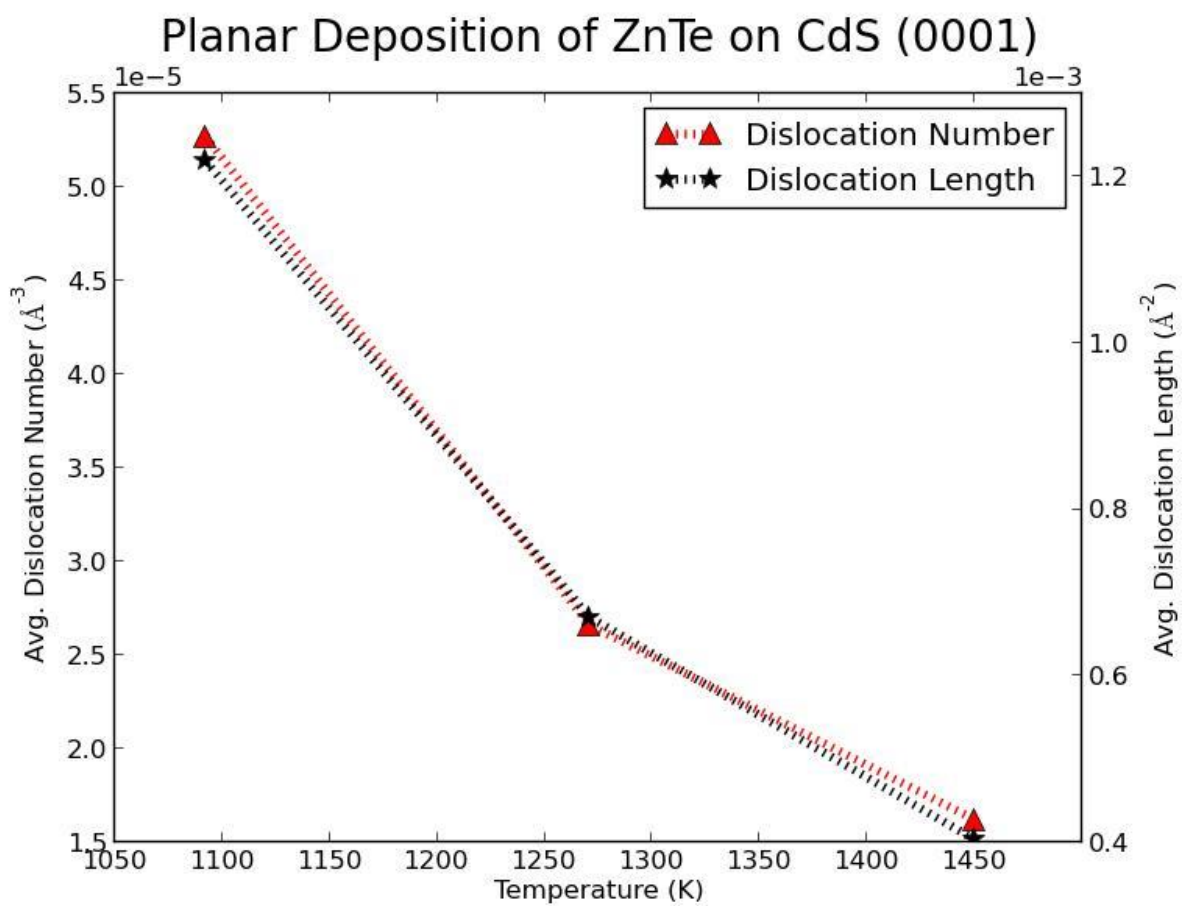


Figure 3.4: Plot of dislocation densities for planar ZnTe on CdS at several deposition temperatures.

### 3.1.4 Optimal Deposition Temperature for Selective CdTe on CdS

This subsection reports the defect data measured for selective CdTe on CdS depositions performed over a range of temperatures. The range of temperatures used for these experiments is shown in Table 2.7. The plot in Fig. 3.5 shows that selective growths share the crystallinity trend observed in planar growths, however at high deposition temperature values (starting at target temperature 1200 K) an amorphous layer formed at the surface of the film. This effect was very similar to that shown in Fig. 3.7 where a layer of amorphous material (orange atoms) formed on top of the film, becoming thicker as the temperature increased. The amorphous material seemed to originate from the accumulation of atoms into the mask walls and the condition worsened at higher temperatures due to the higher mobility of particles. Because of the decrease in crystalline material that occurred during at these temperatures, these values were discarded for future simulations. Taking these observations into consideration, the best crystalline films in these experiments were grown at ~925 K (target temperature of 1100 K).

Table 2.7: Comparison between simulation target temperature and actual average temperature for selective CdTe on CdS.

<b>Target Temperature (K)</b>	<b>Avg. Measured Temperature (K)</b>
1000	845
1100	925
1200	1007
1300	1098

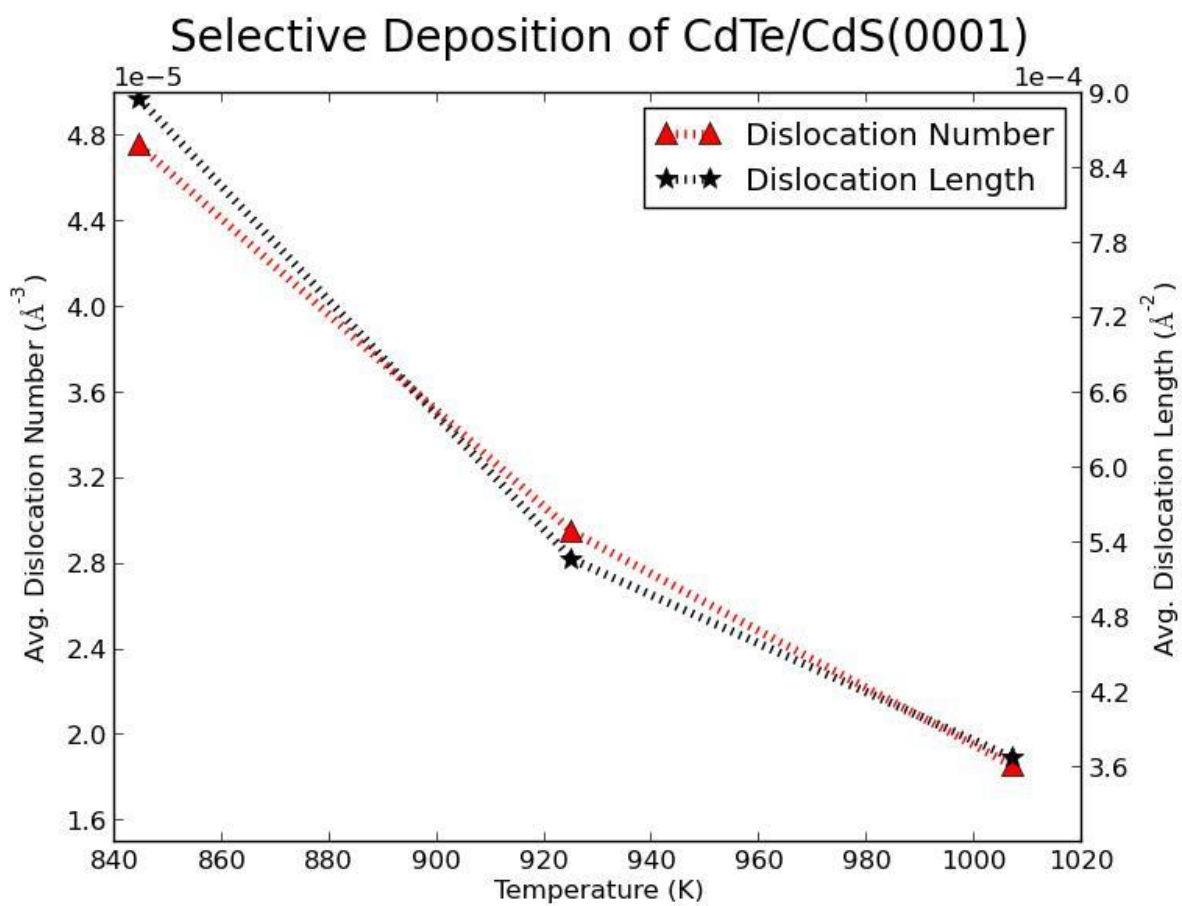


Figure 3.5: Plot of dislocation densities for selective CdTe on CdS at several deposition temperatures.



### **3.1.5 Optimal Deposition Temperature for Selective CdTe/ZnTe bilayer on CdS**

This sub-section reports the results obtained for the CdTe/ZnTe bilayer on CdS depositions using the range of temperatures shown in Table 2.8. Fig. 3.6 plots the dislocation analyses results. Less defects were found in simulations grown at ~912 K (target temperature of 1100 K), while growths at temperatures lower than this exhibit a higher defect presence. An interesting trend was observed for films grown at higher temperatures (beginning at target temperature 1200 K) that consisted of an amorphous layer that formed at the surface of the film that can be seen in Fig. 3.7 (orange atoms on the film surface). Visualization of the growths helped identified the origin of this condition, which appears to be influenced by the accumulation of adatoms at the mask walls. This behavior worsened as the substrate temperature increased and as result the film crystallinity in those simulations dropped.

Table 2.8: Comparison between simulation target temperature and actual average temperature for selective CdTe/ZnTe bilayer on CdS.

<b>Target Temperature (K)</b>	<b>Avg. Measured Temperature (K)</b>
1000	832
1100	912
1200	995
1300	1083

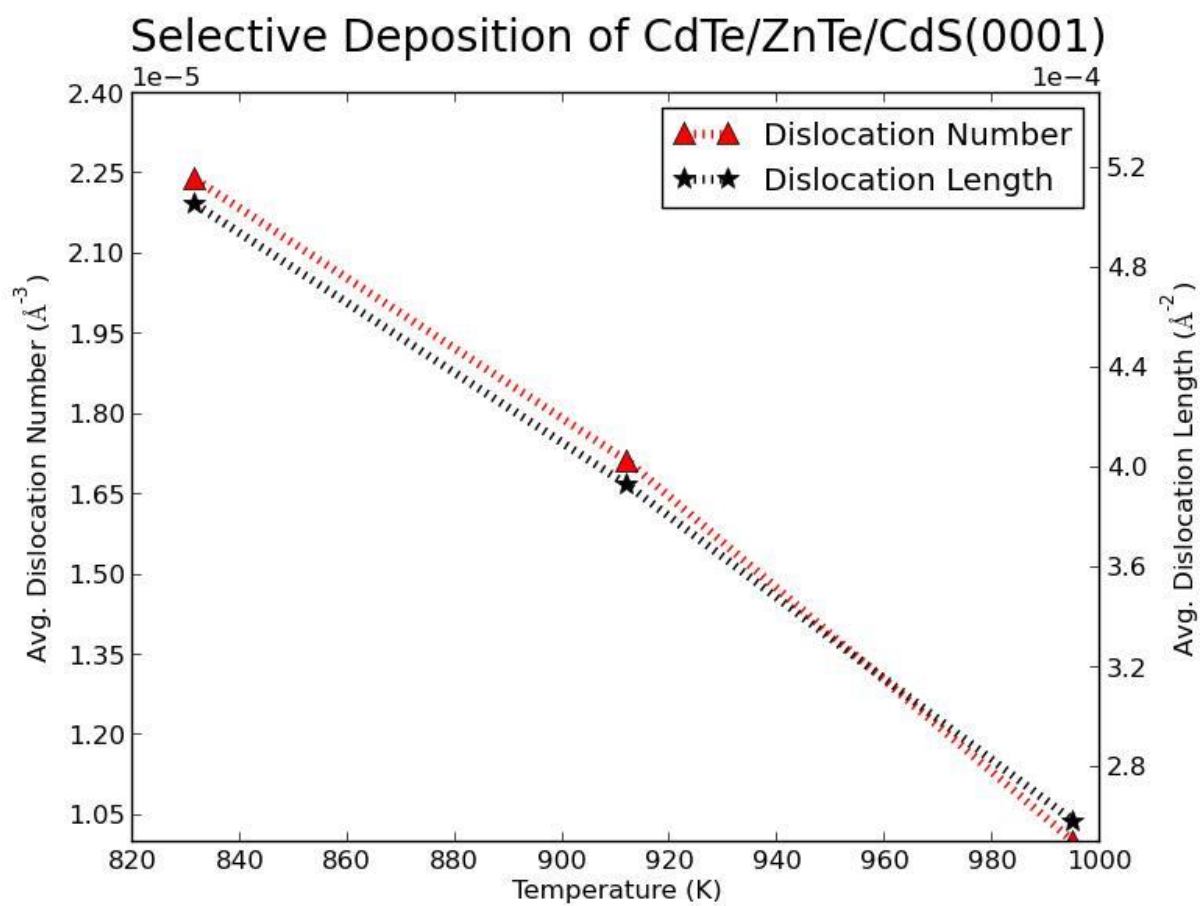


Figure 3.6: Plot of dislocation densities for selective CdTe/ZnTe bilayer on CdS at several deposition temperatures.

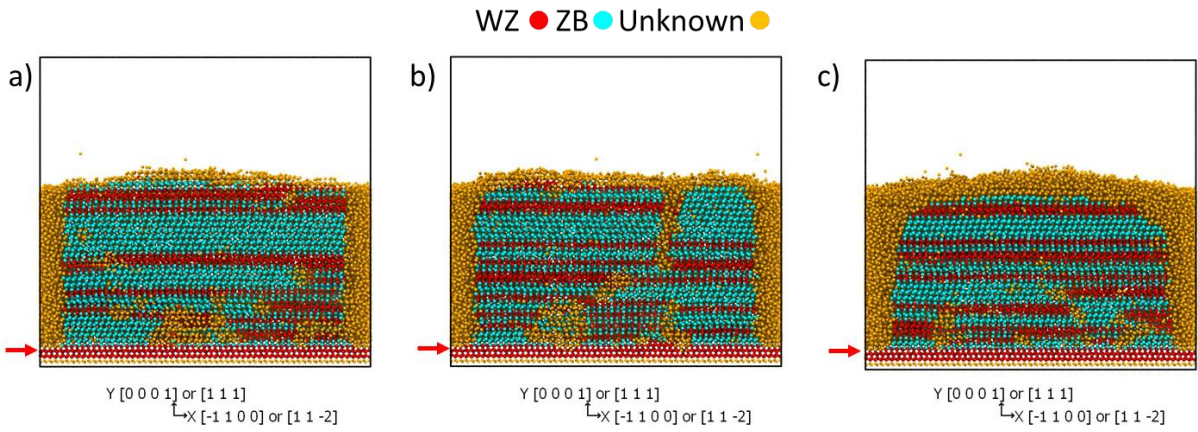


Figure 3.7: Cross-section visualization of a structural analysis for selective CdTe/ZnTe grown on CdS at a) 1000 K, b) 1100 K, and c) 1200 K (target temperatures). Red arrows indicate the location of the film-substrate interface.

### **3.2 Effect of Island Size on Defect Density**

The following sub-sections report the dislocation densities detected within the selective epilayer growths designed to study the effect of island size. Visualization of dislocation profiles and lattice structure maps are shown to describe the structural changes occurring within the epilayers grown as islands of different widths.

#### **3.2.1 Different Island Size for CdTe on CdS Depositions**

The dislocation densities measured in CdTe islands grown on CdS are plotted in Fig. 3.8. The trend observed was that film crystallinity improved as the island size decreased. These results are in good agreement with the CdTe/CdS island model predicted by nano-heteroepitaxy in sub-section 1.2. A visualization of the wurtzite dislocation profile detected is shown in Fig. 3.9 for all three island sizes. Comparison of Fig.3.9.a-c reveals that the length, type, and number of dislocations increases with increasing island size. A similar behavior was observed in zinc blende dislocations (not shown). In addition the dislocation behavior described in subsection 2.2.3 was seen for all three island sizes, a large number of wurtzite dislocations are formed close to the interface, while more zinc blende dislocations formed away from the interface.

Fig. 3.10 shows the structural analysis for the three different island sizes. These are material slices parallel to the interface plane, at a distance about half the total film thickness. Zinc blende domains are represented by light blue atoms, wurtzite domains by red atoms, and unknown atoms structures (mask walls and grain boundaries) are displayed in orange. Comparison between these images indicates that fewer grains are contained within smaller islands. In contrast the grain size, distribution, and lattice structure becomes more diverse and numerous as the island size increases. This behavior correlates well with the dislocation data since large numbers of grain indicate that many grain boundaries are found within the film, therefore dislocations originating in these grain boundaries should be just as numerous. Additionally the grain size behavior described in subsection 2.2.3 was seen for all three island

sizes, meaning that small grain sizes were seen at the interface while larger grains were observed away from the interface.

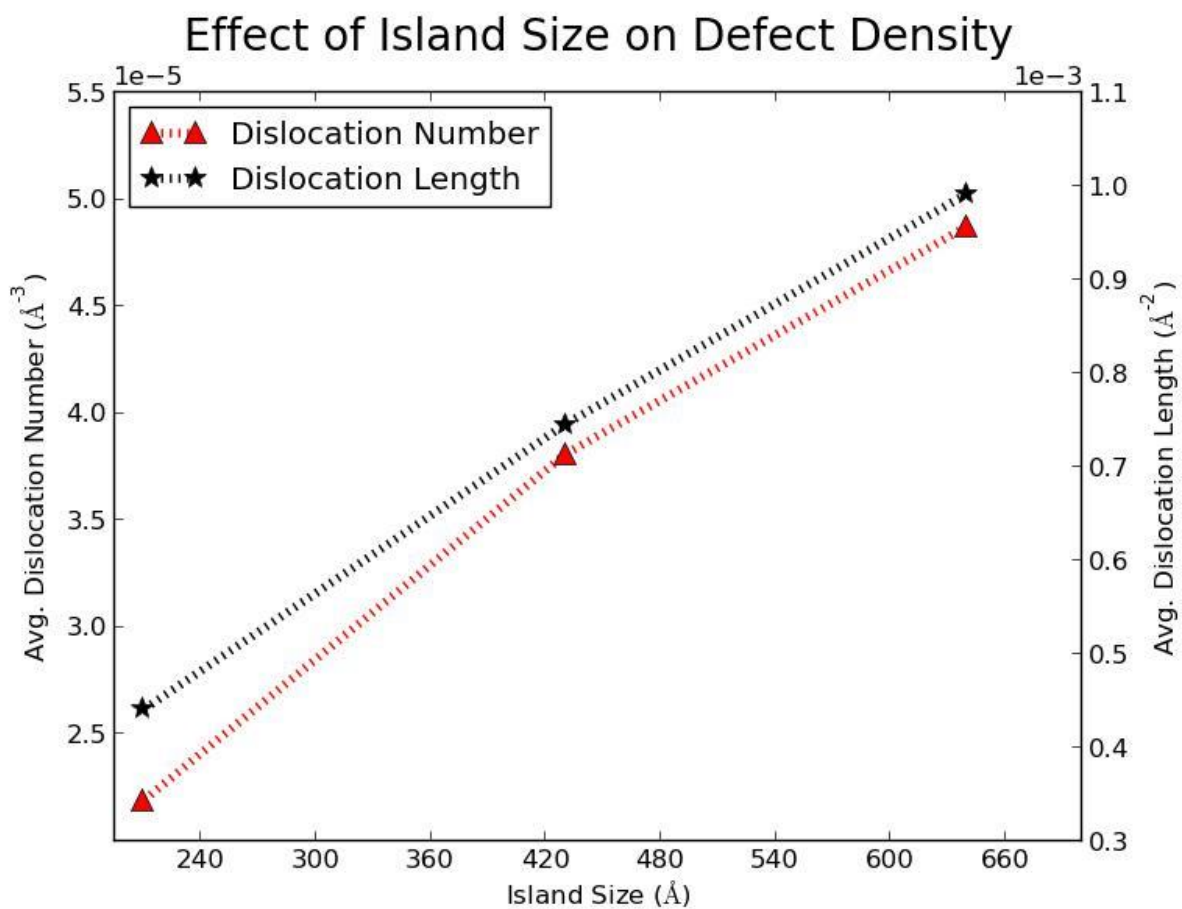


Figure 3.8: Plot of dislocation densities for multiple size CdTe islands grown on CdS.

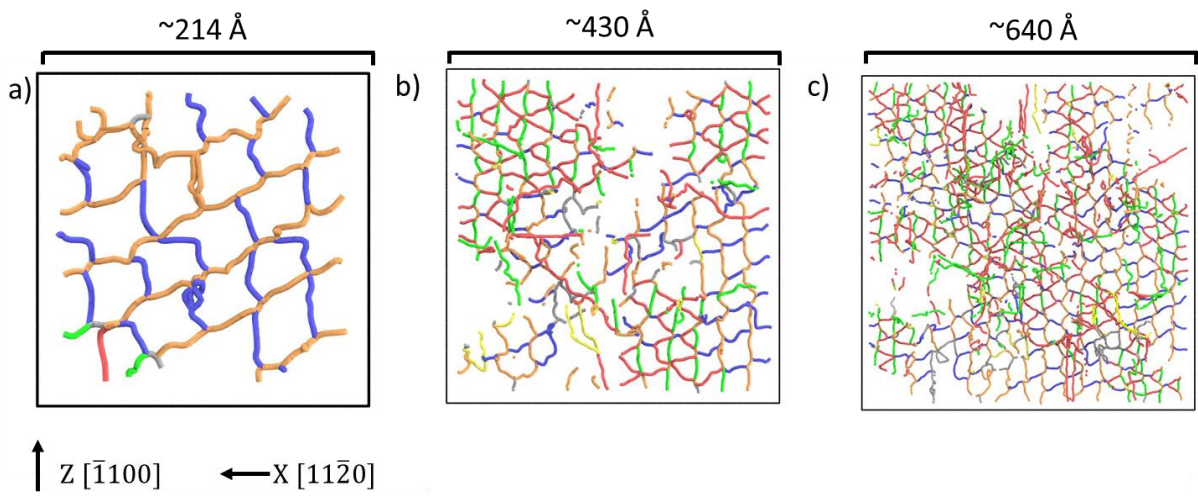


Figure 3.9: Dislocation profile visualizations for multiple size CdTe islands grown on CdS. a)  $\sim 214 \text{ \AA}$ , b)  $\sim 430 \text{ \AA}$ , and c)  $\sim 640 \text{ \AA}$  island width.



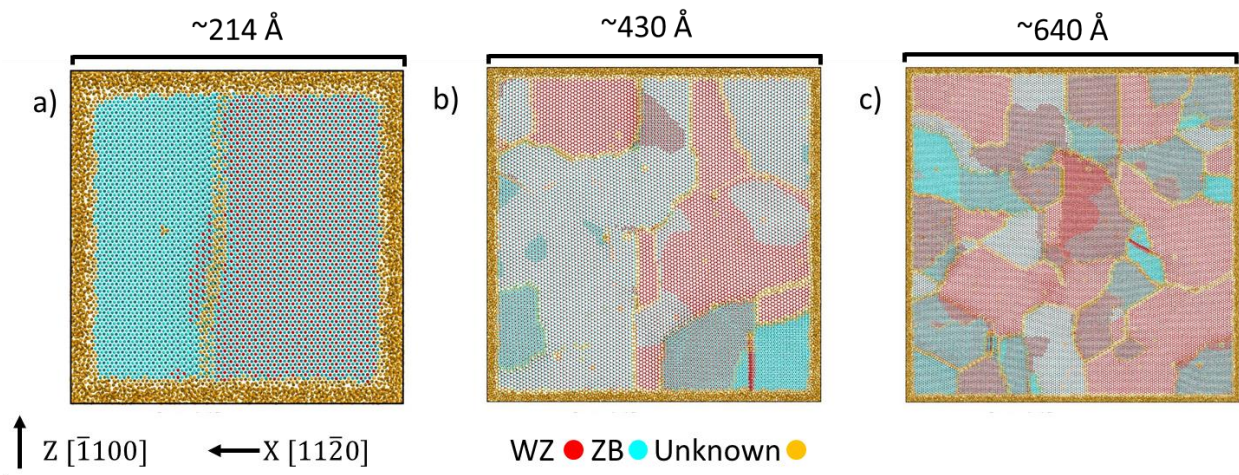


Figure 3.10: Lattice structure maps for material slices parallel to the interface plane at a distance of half the epilayer thickness. Fewer grains are observed in the smallest island (a), while the grain size and type increase with larger island size (b and c).

### 3.3 Effect of Zn Alloying on Defect Density

The following sub-sections report the dislocation densities detected using the CAT for simulations used to study the effect of Zn alloying. Visualization of dislocation profiles and lattice structure maps are shown to describe the epilayer structure. Composition profiles were employed to verify the elemental composition as a function of sample thickness.

#### 3.3.1 Optimal Alloy Composition in Planar $\text{Cd}_{(1-x)}\text{Zn}_x\text{Te}$

In this sub-section the defect analysis results for the planar  $\text{Cd}_{(1-x)}\text{Zn}_x\text{Te}$  on CdS simulations performed over a range of  $x$  values are reported. Fig. 3.11 plots the dislocation data detected inside the planar  $\text{Cd}_{(1-x)}\text{Zn}_x\text{Te}$  films. In this data, the trend observed was that high Zn content in the buffer layer creates more defects when compared to conventional CdTe growths. However, the use of a  $\text{Cd}_{0.8}\text{Zn}_{0.2}\text{Te}$  buffer layer was successful in decreasing the epilayer dislocation density when compared to CdTe growths alone. Fig. 3.12 shows a composition profile of one of the  $\text{Cd}_{0.8}\text{Zn}_{0.2}\text{Te}$  buffer layer growths as a function of sample thickness. It can be seen that  $\text{Cd}_{0.8}\text{Zn}_{0.2}\text{Te}$  composition was successfully achieved and the Zn concentration was mostly constant throughout the buffer layer.

Employing the  $\text{Cd}_{0.8}\text{Zn}_{0.2}\text{Te}$  buffer layer resulted in highly crystalline films as observed in Fig. 3.13.a and confirmed by the structural analysis in Fig. 3.13.b. In addition, the dislocations profiles shown in Fig. 3.14 revealed that the use of this buffer layer configuration was successful in suppressing the formation of dislocations within the bulk of the film. The dislocations were formed only close to the interface, in good agreement with the location of the disordered atoms (orange) in Fig. 3.12.b. These results indicate that the  $\text{Cd}_{0.8}\text{Zn}_{0.2}\text{Te}$  buffer layer was successful in accommodating some of the strain between the film and the substrate, and allowed the growth of an almost single crystalline film.

The drop in film crystallinity for buffer layers containing high Zn concentrations ( $x > 0.2$ ) is in good agreement with experimental data available in literature [20] [21] [22] for ternary and quaternary CdTe-based alloys grown on Si (211) substrates. These studies reported that high

concentrations of a ternary or quaternary species degraded the crystallinity of the CdTe film, while low concentrations showed some promising lattice matching results. The reason why this behavior occurs is not well understood, however one reason could be that the additional species are incompatible with the CdTe lattice and create large distortions at high concentrations. The literature studies experimented with two different alloy species, Zn and Se. Out of these two species, the incorporation of Se was shown to have the best results when compared to Zn ( this species needed lower concentrations to obtain similar crystal morphologies).

The results obtained in these experiments helped identified a Zn concentration that could be used in experiments to produce CdTe films with few defects. More importantly, the simulation capability was able to capture the alloying behavior reported in literature and could therefore be applied towards the study of the crystal disordering phenomenon seen for alloys with high concentrations of a ternary or quaternary species. In particular, the simulation configuration employed in this work could be used to explore the use of Se as a buffer layer since this element is supported by the Stillinger-Webber potential.

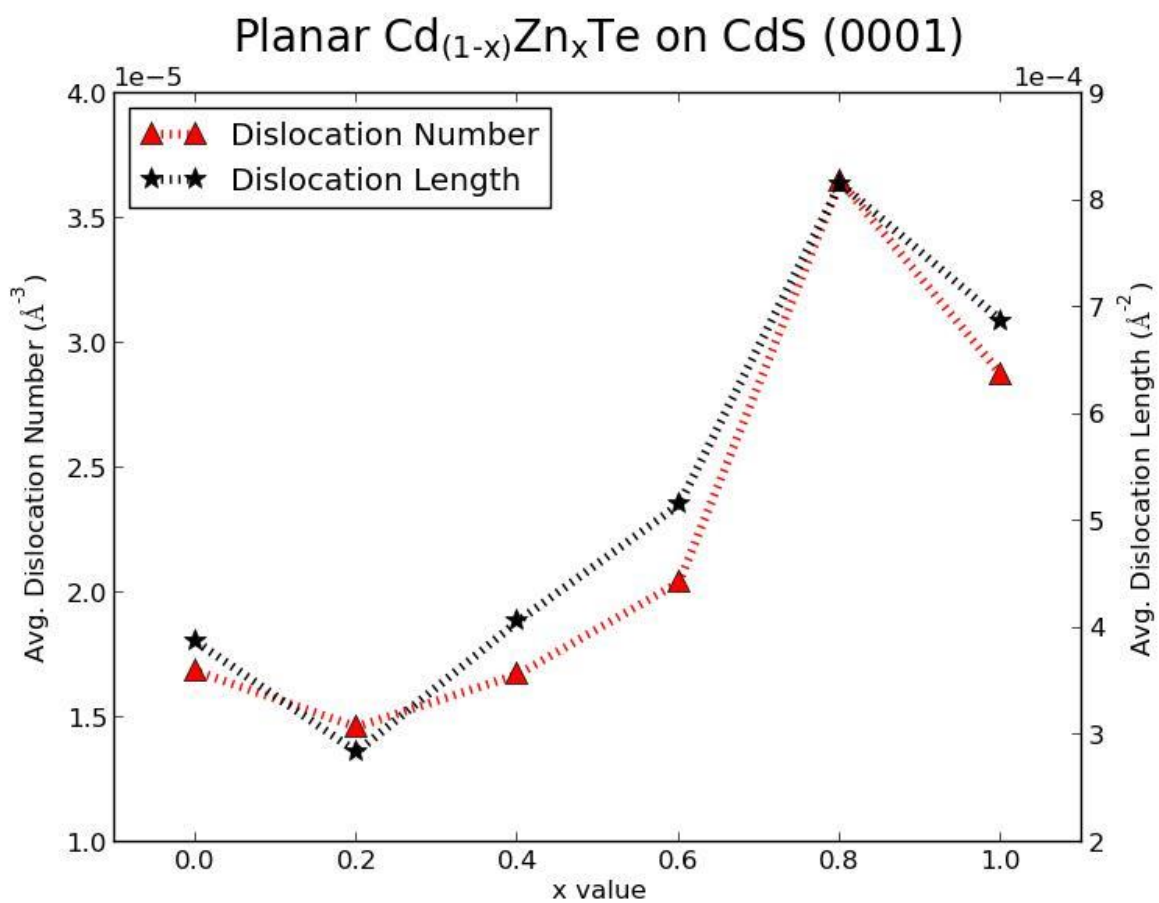


Figure 3.11: Plot of dislocation densities for several x composition values in  $\text{Cd}_{(1-x)}\text{Zn}_x\text{Te}$  planar film depositions grown on CdS.

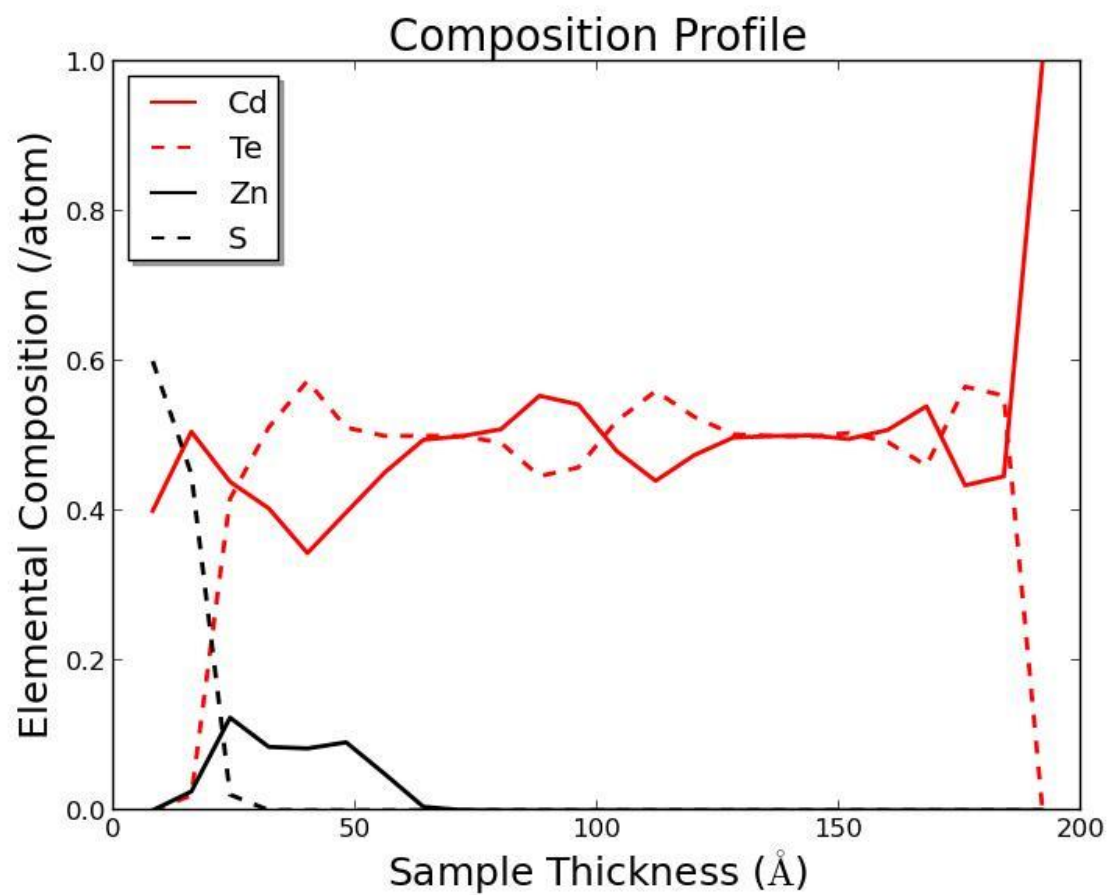


Figure 3.12: Plot of composition profile for planar  $\text{Cd}_{0.8}\text{Zn}_{0.2}\text{Te}$  deposited on CdS.

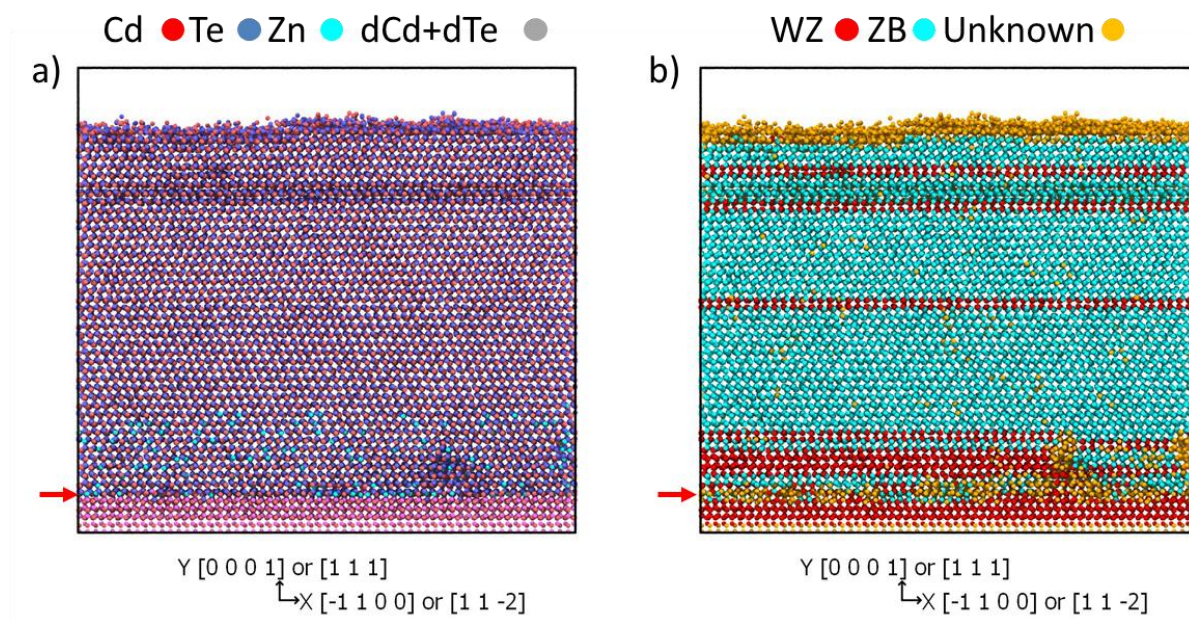


Figure 3.13: Cross-section visualization of a planar  $\text{Cd}_{0.8}\text{Zn}_{0.2}\text{Te}$  film deposited on  $\text{CdS}$  a) species b) structural analysis. The red arrows indicate the location of the film-substrate interface.

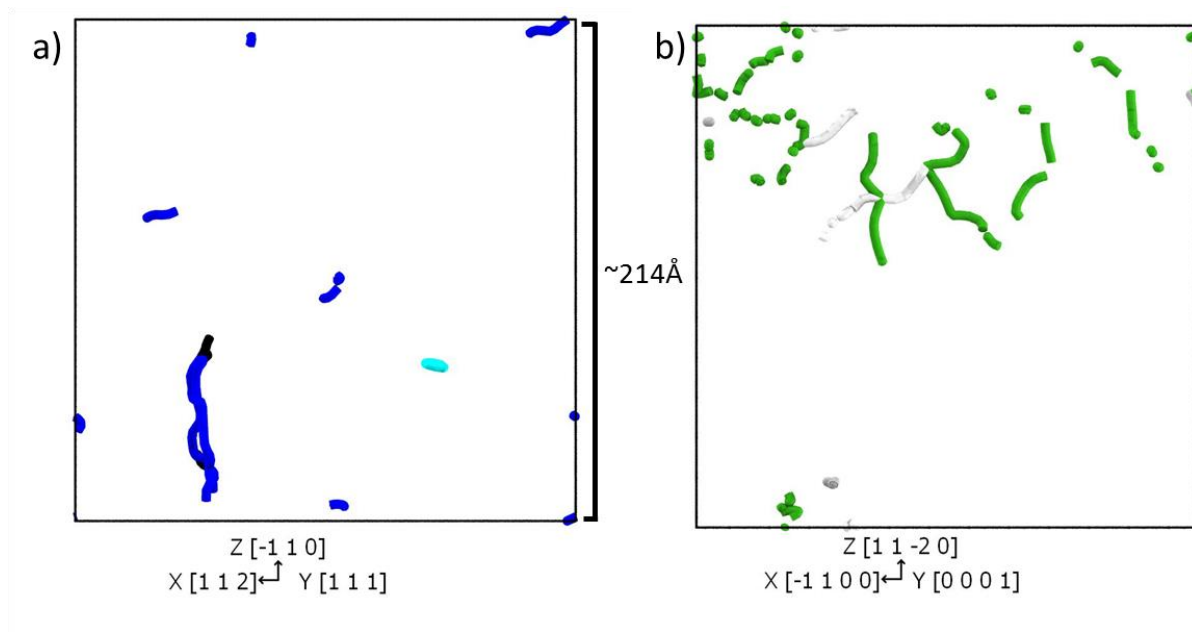


Figure 3.14: Top view dislocation profile visualization for a planar  $\text{Cd}_{0.8}\text{Zn}_{0.2}\text{Te}$  film deposited on CdS a) zinc blende dislocations b) wurtzite dislocations.

### 3.3.2 Optimal Alloy Composition in Selective $\text{Cd}_{(1-x)}\text{Zn}_x\text{Te}$

The defect analyses data for the selective  $\text{Cd}_{(1-x)}\text{Zn}_x\text{Te}$  on CdS simulations performed over a range of  $x$  values are reported in this subsection. Fig. 3.15 plots the dislocation densities detected in these simulations. Similarly to the planar graded growth, the trend observed in this data is that high Zn content in the buffer layer degrades the crystallinity of the epilayer. In addition, the use of a  $\text{Cd}_{0.8}\text{Zn}_{0.2}\text{Te}$  buffer layer was also successful in decreasing the epilayer dislocation density when compared to CdTe alone for selective growths. Fig. 3.16 shows a composition profile of one of the  $\text{Cd}_{0.8}\text{Zn}_{0.2}\text{Te}$  buffer layer growths as a function of sample thickness. It can be seen that  $\text{Cd}_{0.8}\text{Zn}_{0.2}\text{Te}$  composition was successfully achieved and the Zn concentration profile was mostly linear throughout the buffer layer.

A cross-sectional visualization displaying the species in a  $\text{Cd}_{0.8}\text{Zn}_{0.2}\text{Te}$  buffer layer growth can be seen in Fig. 3.17.a. The structural analysis of this growth can be seen in Fig. 3.17.b and shows that the film was composed mostly majorly of zinc blende atoms (light blue), with some wurtzite (red) layers. The disordered atoms (orange) are found near the interface. The dislocations profiles shown in Fig. 3.18 revealed that the use of this configuration combining the buffer layer and selective area growth was more successful in suppressing the formation of dislocations when compared to a conventional CdTe configuration.



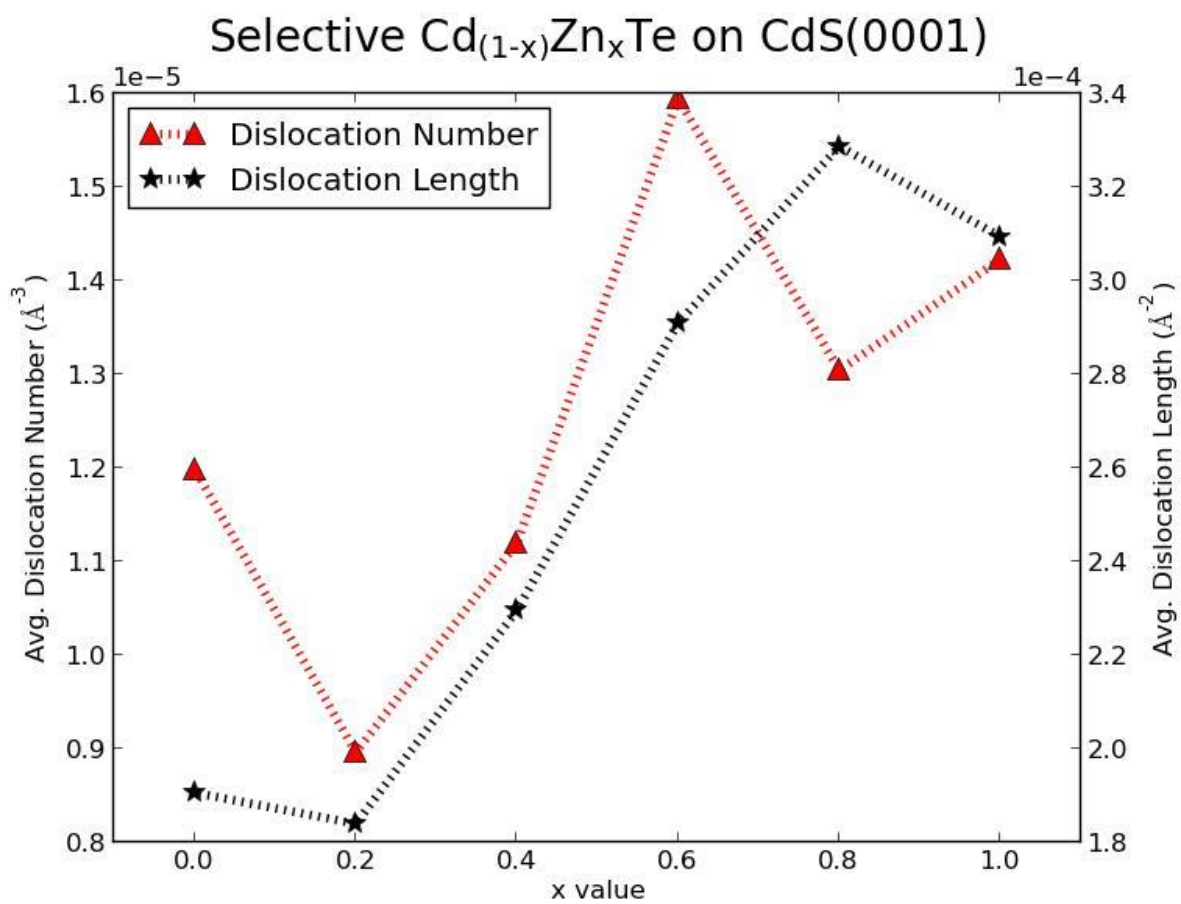


Figure 3.15: Plot of dislocation densities for several x composition values in  $\text{Cd}_{(1-x)}\text{Zn}_x\text{Te}$  selective film depositions grown on  $\text{CdS}$ .

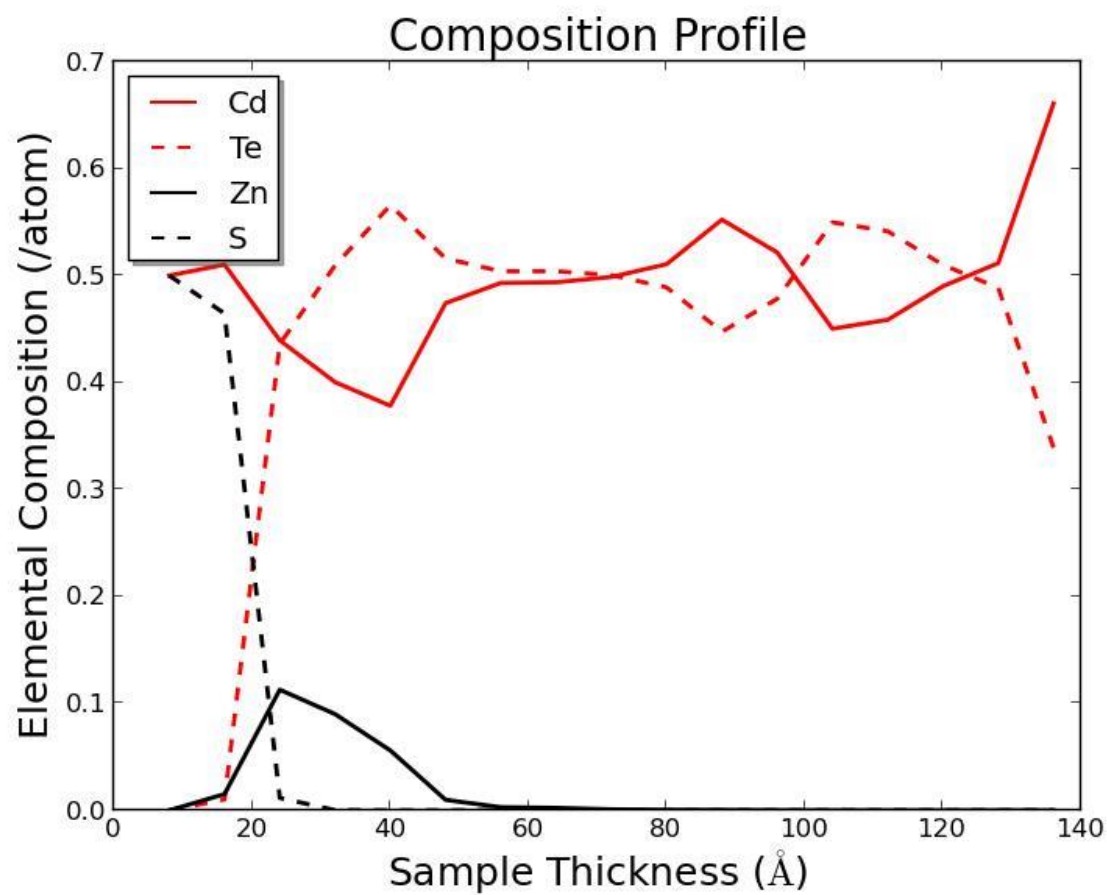


Figure 3.16: Plot of composition profile for selective  $\text{Cd}_{0.8}\text{Zn}_{0.2}\text{Te}$  deposited on  $\text{CdS}$ .

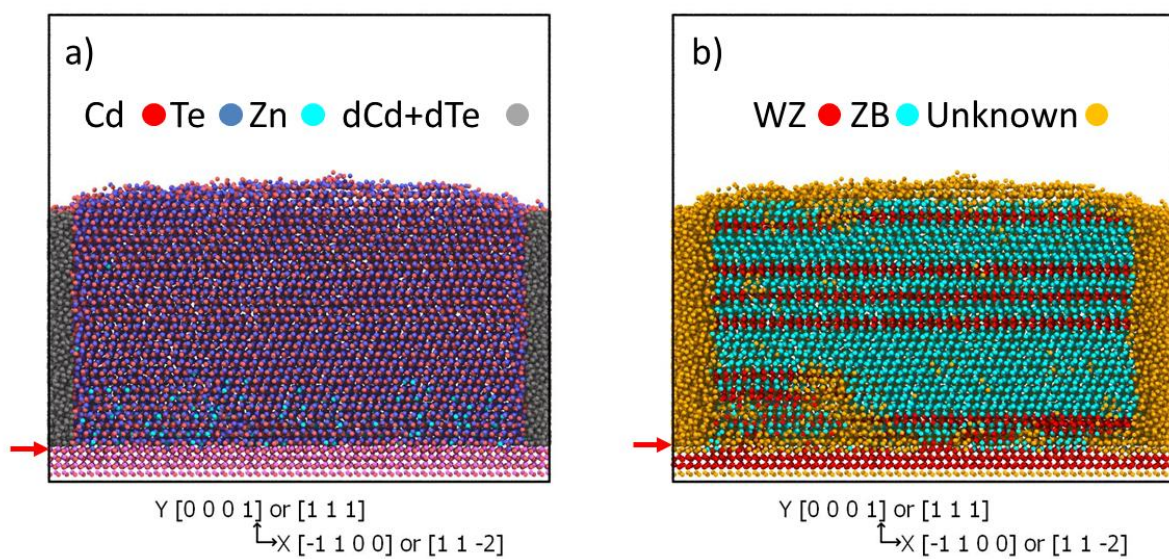


Figure 3.17: Atomistic visualization of a selective  $\text{Cd}_{0.8}\text{Zn}_{0.2}\text{Te}$  deposited on  $\text{CdS}$  simulation. a) cross-section image showing the different atomic species within the nanostructure b) cross-section image showing the showing the identified lattice structures within the nanostructure. The red arrows indicate the location of the film-substrate interface.

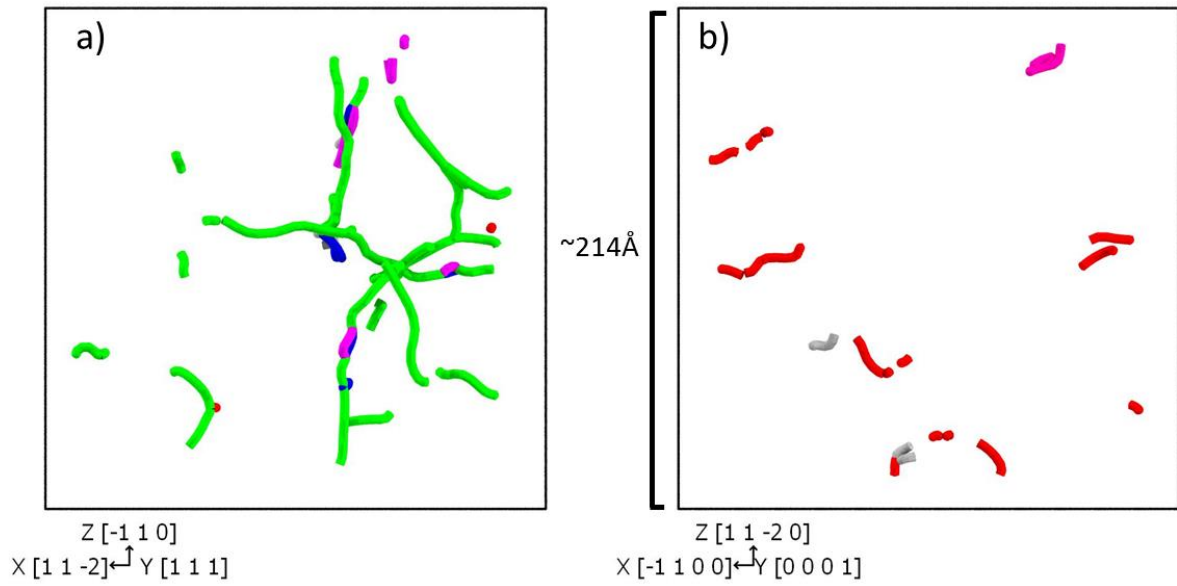


Figure 3.18: Dislocation profile top view visualization of defects detected within a selective  $\text{Cd}_{0.8}\text{Zn}_{0.2}\text{Te}$  deposited on CdS simulation. a) zinc blende dislocations b) wurtzite dislocations. Refer to Table 2.2 for dislocation type indexing.

### 3.4 Dislocation Density Comparison

Fig. 3.19 compares the lowest defect simulations from among all the growth configurations previously discussed in order to provide a clear comparison of the effectiveness of each growth configuration and to visualize the trend obtained in this study. The highest dislocation density measured was from a conventional planar CdTe on CdS simulation with a  $\sim 640$  Å substrate (discussed in subsection 2.3.3). Next to this value we observe how the dislocation density drops as we decrease the size of the island by 11%, 34%, and 47% for the  $\sim 640$ , 430, and 210 Å islands respectively compared to the conventional CdS structure. Then we observe how the  $\text{Cd}_{0.8}\text{Zn}_{0.2}\text{Te}$  alloying profiles further decrease defects densities by 60% and 80%, for planar and selective graded growths respectively, when compared to the conventional structure. The lowest defect density measured in this study was the selective  $\text{Cd}_{0.8}\text{Zn}_{0.2}\text{Te}/\text{CdS}$  configuration. These results clearly suggest that careful nano-structuring that combines Zn alloying and nanoheteroepitaxy could effectively reduce the presence of defects in CdTe films grown on CdS substrates.

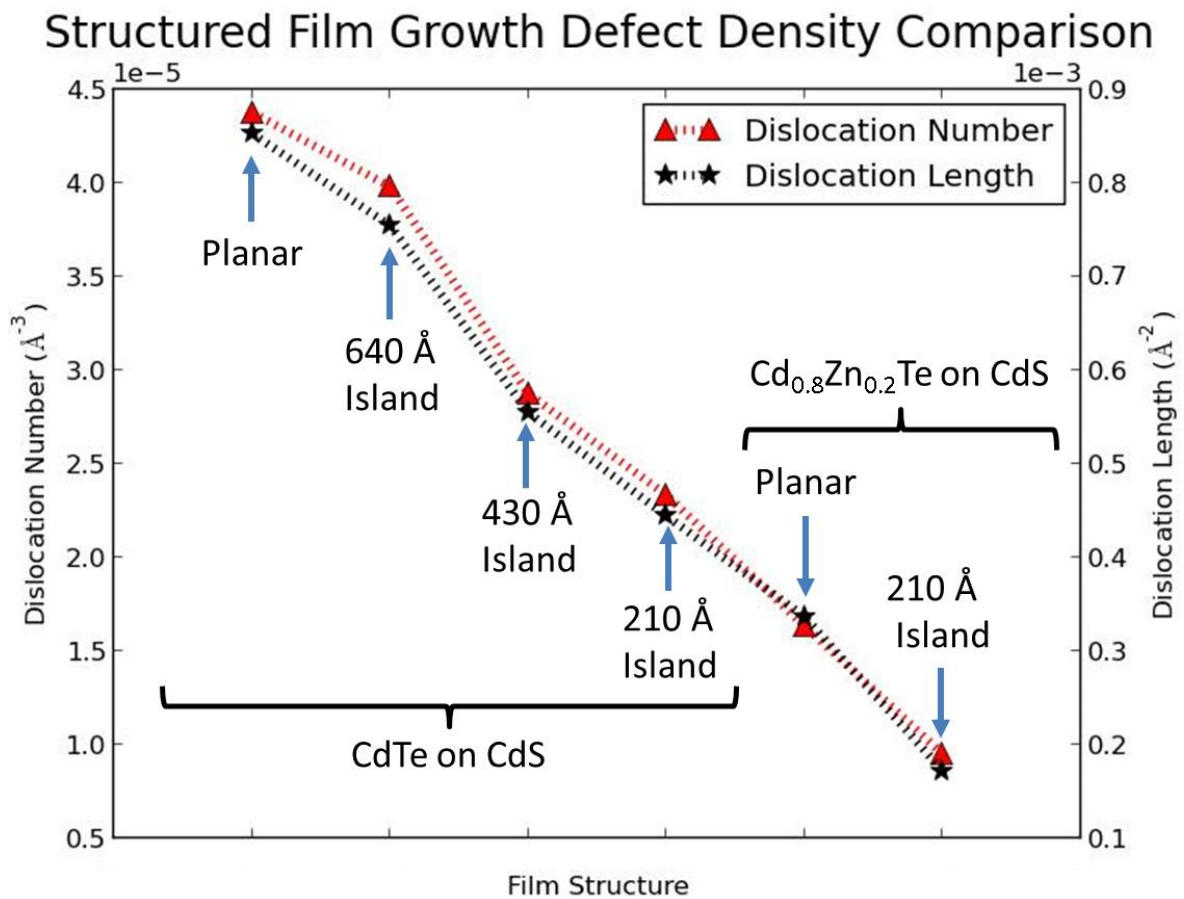


Figure 3.19: Plot of comparing the defect densities for several nano-structured CdTe films deposited on CdS.

### 3.3.6 Thermodynamics Study of Simulated Nanostructures

This subsection describes a thermodynamics model that was developed to explain in terms of energy why the defect density in the CdTe epilayer decreased during the simulated growths when nano-structured epitaxy was used. The nanoheteroepitaxy theory proposes that during selective area growth conditions, the epilayer should be able to decrease its strain energy through three dimensional strain partitioning. Some of this energy will be shared with a compliant substrate. The combination of these conditions allows the epilayer to prevent the formation of dislocations. In conventional planar heteroepitaxy, as the film thickness increases so does the strain energy. Dislocation formation begins when the critical film thickness is reached, in order to relieve strain energy and allow the film to relax.

The model employed molecular statics simulations in order to find evidence of strain partitioning in the system. The objective of molecular statics is to find the minimum energy configuration of a given input system of particles (no growth dynamics). The aim was to calculate the potential energy difference as a function of distance between planar and selective CdTe/CdS systems. The potential energy difference as a function of distance between the two systems would reveal if the energy of the system changed as predicted by nanoheteroepitaxy. The energy of the substrate was supposed to increase, while the energy of the epilayer was supposed to decrease.

The two structures created consisted of 89 closed-packed planes of wurtzite CdTe and CdS. The substrates consisted of 44 closed-packed CdS (0001) planes with total number of 274,560 atoms. The films were made up of 45 closed-packed CdTe (0001) planes with a total number of 219,420 atoms.

Once the atomistic models were created, the next step was to minimize the energy of each system in order to allow the atoms to relax to their lowest energy configuration. The planar system had an additional number of film atoms during the energy minimization in order to maintain the periodicity of the planar structure. These extra atoms were removed after minimization as seen in Fig. 3.20.a in order to keep the exact number of film atoms described in

the previous paragraph. The selective system has these extra atoms removed before the energy minimization in order to create the nano-island structure. Fig. 3.20.b shows the relaxed nano-island configuration in which three dimensional relaxation and substrate compliance can be observed due to the displacement of atoms in the epilayer and at the corners of the interface. These structural changes are evident when compared to the structure in Fig. 3.20.a.

Then the potential energy for every atom in the relaxed systems was calculated. Afterwards, the atoms were grouped into 89 groups according to the closed-packed plane they belonged to. The pre-energy minimization structures were used as reference to group atoms using a unique atomic identifier that remained unchanged after energy minimization and that effectively linked each atom to its closed-packed plane group. An algorithm was employed to calculate the average potential energy for all the atoms inside each closed-packed plane. The potential energy difference was then calculated by applying equation 10 to each corresponding group of atoms.

$$\varphi_{difference} = \frac{(\varphi_{selective} - \varphi_{planar})}{|\varphi_{planar}|} \times 100 \quad (10)$$

Fig. 3.21 plots the calculated potential energy difference as a function of distance (black solid line), as well as the average potential energy for each group of atoms in the planar (red dotted line) and selective (green dotted line) structures. The average potential energy in the planar system is a step function due to the difference in average potential energy for each closed-packed plane between the CdS and CdTe materials. The average potential energy curve for the selective system shows that under these conditions the step function disappears and the average potential energy value changes linearly throughout the system thickness. The potential energy curve has a negative sign on the substrate region indicating that energy of the substrate increased for the selective system when compared planar. This could be evidence of substrate compliance. In contrast, the potential energy curve shows a positive sign for the film region indicating that



the film energy decreased in the selective system when compared to planar. This could be evidence of three dimensional relaxation in the film.

The model was expanded to incorporate the presence of the Zn alloying in order to explain the defect density behavior observed in the simulated growths in chapter 3. Fig. 3.22.a shows the atomistic visualization of the selective system of CdTe/ZnTe bilayer on CdS after energy minimization. It can be seen that a large amount of deformation occurred in the ZnTe buffer layer while almost no deformation can be seen on the CdS substrate. Fig. 3.22.b shows the atomistic visualization of the selective system of CdTe/  $\text{Cd}_{0.8}\text{Zn}_{0.2}\text{Te}$  bilayer on CdS after energy minimization. The image shows film relaxation and substrate deformation that create a more coherent film/substrate interface than the two previous cases.

Fig 3.23 plots the calculated potential energy difference as a function of distance (black solid line), as well as the average potential energy for each group of atoms in the planar (red dotted line) and selective (green dotted line) CdTe/ZnTe bilayer on CdS structure. Similarly to the CdTe on CdS system discussed previously, the average potential energy in the planar system is a step function that this time includes an additional small step due to the ZnTe buffer layer presence. The average potential energy curve for the selective system shows that under these conditions the step function changes to a smooth curve. In contrast to the CdTe on CdS system, the curve reaches a minimum value just below the interface indicating that in this region the substrate was less compliant. The potential energy curve has a negative sign on the substrate region indicating that energy of the substrate increased for the selective system when compared planar, except for the small peak close to the interface in the substrate region that did not exhibit much compliance. In contrast, the potential energy curve shows a positive sign for the film region indicating that the film energy decreased in the selective system when compared to planar. This could be evidence of three dimensional relaxation in the film.

Fig 3.24 plots the calculated potential energy difference as a function of distance (black solid line), as well as the average potential energy for each group of atoms in the planar (red dotted line) and selective (green dotted line) CdTe/  $\text{Cd}_{0.8}\text{Zn}_{0.2}\text{Te}$  bilayer on CdS structure.

Similarly to the CdTe/ZnTe on CdS system discussed previously, the average potential energy in the planar system is a step function with a smoother ZnTe step. The average potential energy curve for the selective system shows that under these conditions the step function changes to a smooth linear curve. The potential energy curve has a negative sign on the substrate region indicating that energy of the substrate increased for the selective system when compared planar. In contrast, the potential energy curve shows a positive sign for the film region indicating that the film energy decreased in the selective system when compared to planar. This could be evidence of three dimensional relaxation in the film.

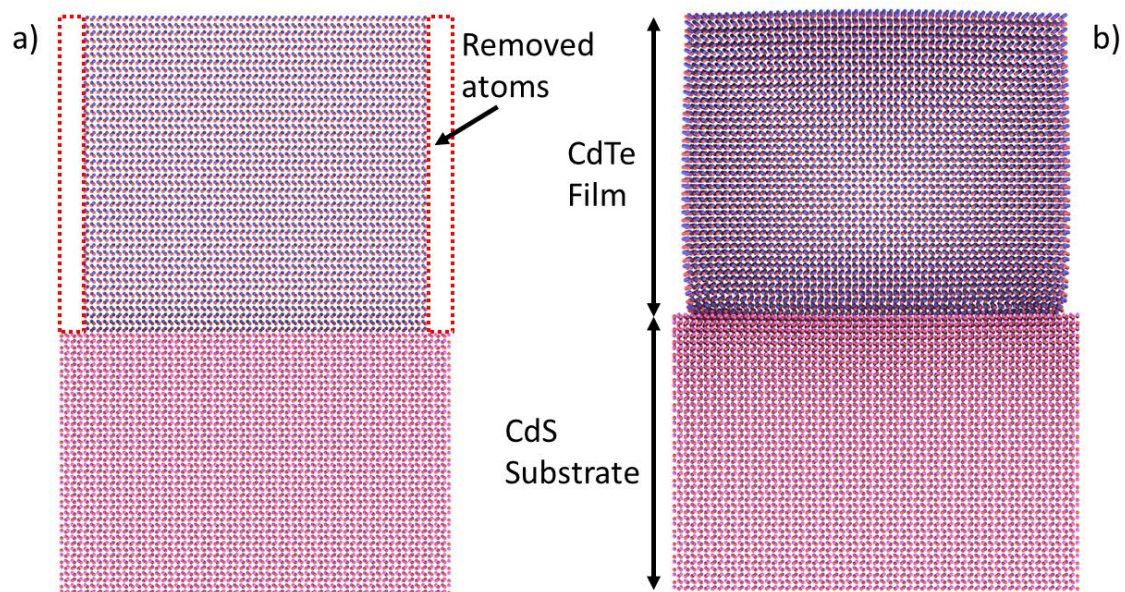


Figure 3.20: Atomistic visualization of the planar and selective CdTe on CdS systems after energy minimization.

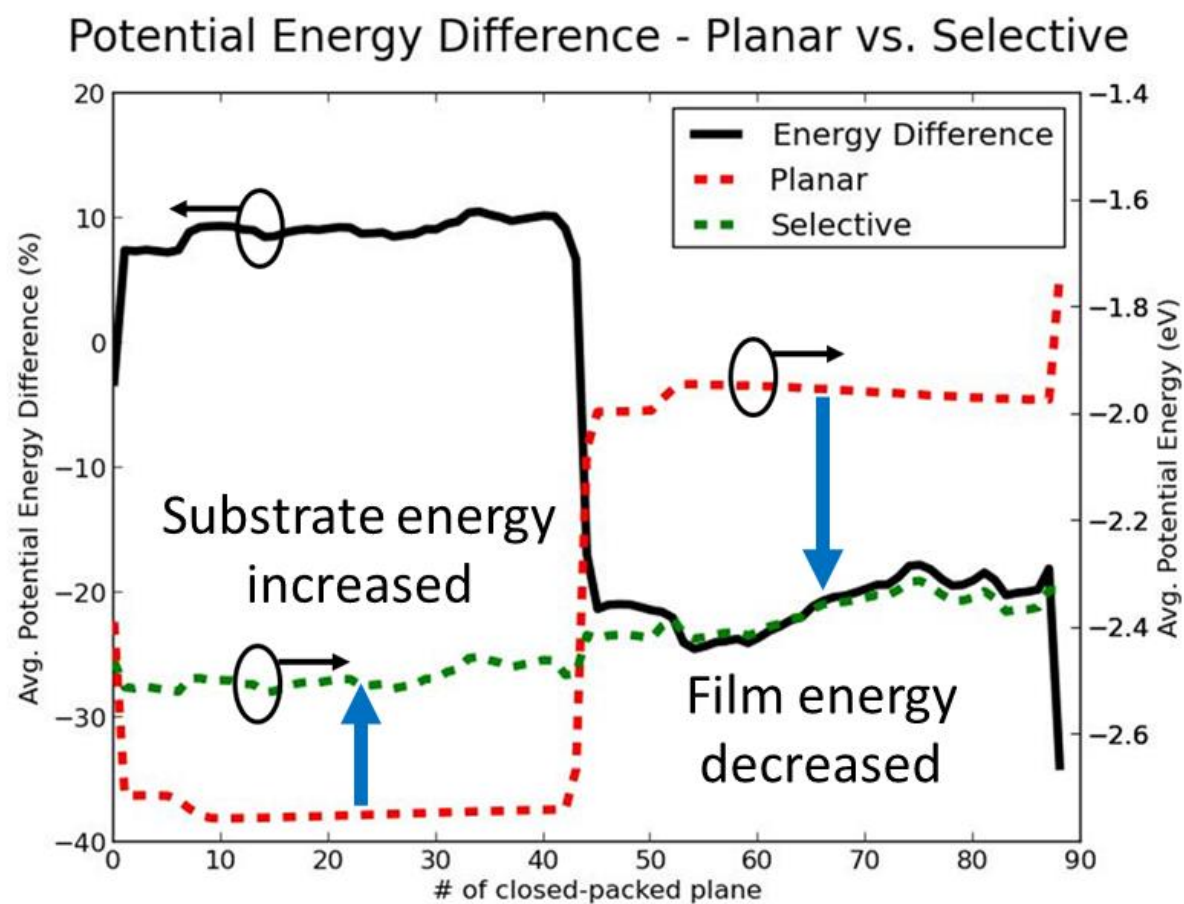


Figure 3.21: Plot of potential energy difference between planar and selective CdTe on CdS.

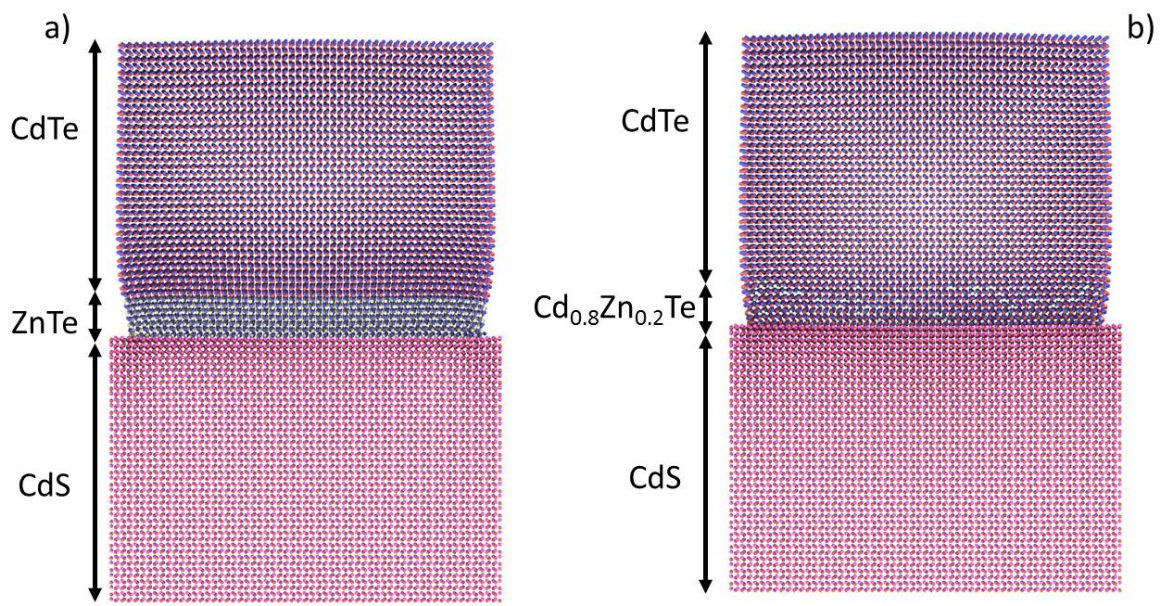


Figure 3.22: Atomistic visualization of the selective  $\text{Cd}_{(1-x)}\text{Zn}_x\text{Te}$  on  $\text{CdS}$  systems after energy minimization.

## Potential Energy Difference - Planar vs. Selective

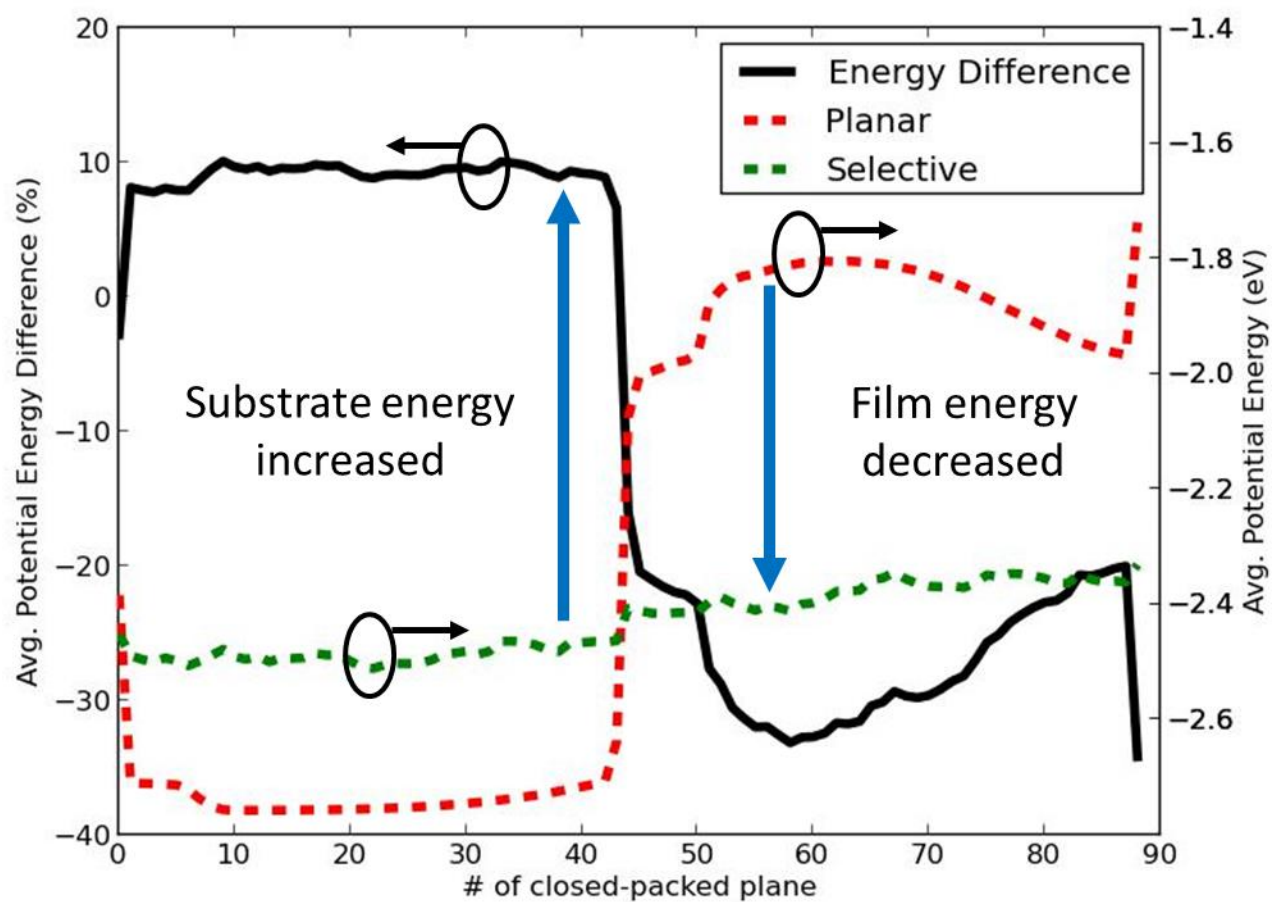


Figure 3.23: Plot of potential energy difference between planar and selective CdTe/ZnTe/CdS.



## Potential Energy Difference - Planar vs. Selective

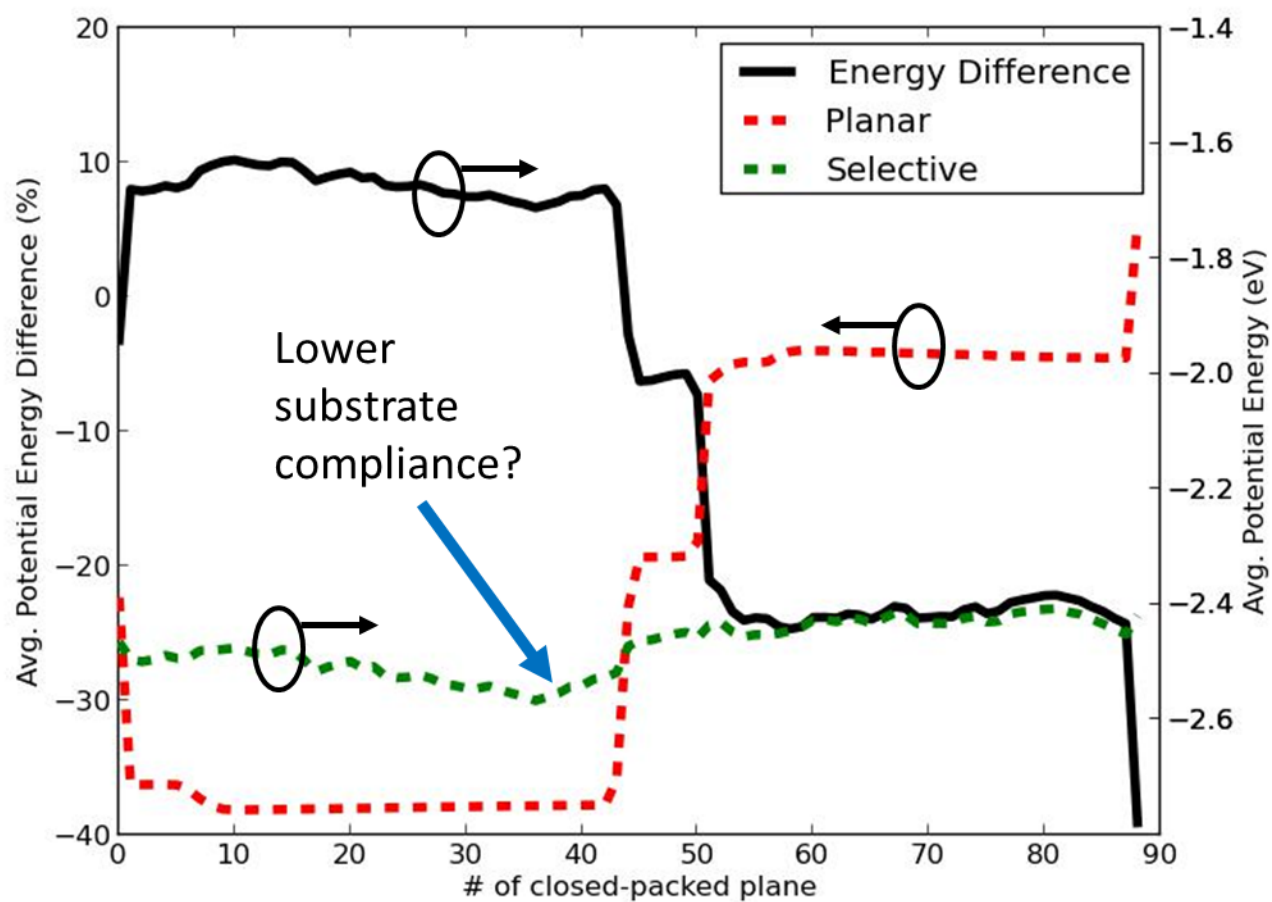


Figure 3.24: Plot of potential energy difference between planar and selective  $\text{Cd}_{0.8}\text{Zn}_{0.2}\text{Te}$  on  $\text{CdS}$ .

## Chapter 4: Conclusions and Summary

Molecular dynamics simulations employing a high fidelity Stillinger-Webber interatomic potential have been carried out to evaluate defect reduction strategies during the fabrication of CdTe on CdS thin films grown via vapor deposition. The first defect reduction strategy consisted of introducing Zn alloying in order to reduce the effect of the large strain between CdTe and CdS. A capability to simulate the controlled vapor deposition of  $\text{Cd}_{(1-x)}\text{Zn}_x\text{Te}$  was developed and used to deposit alloyed films over a wide range of growth configurations and alloy profiles. The second defect reduction strategy studied was the selective-area growth of CdTe to enable strain relief mechanisms that improve epilayer material quality. The simulation capability to model selective-area growth was developed and used to grow islands of different sizes. The vapor disposition simulation code was designed to allow the combination of both defect reduction strategies, and was employed to grow a variety of selective  $\text{Cd}_{(1-x)}\text{Zn}_x\text{Te}$  configurations.

The MD atomistic data results were analyzed using a defect detection capability that consisted of software tools that detect, quantify, categorize and visualize the dislocations found within a simulation data file. A new intrinsic stacking fault defect model for the Crystal Analysis Tool was developed and evaluated in order to detect dislocation lines inside of hexagonal diamond lattice structure atomistic data. The Crystal Analysis Tool was used to search for dislocation line densities in each simulation result in order to evaluate the effectiveness of the defect reduction strategies described in the previous paragraph.

The dislocation line densities trend observed in the planar  $\text{Cd}_{(1-x)}\text{Zn}_x\text{Te}/\text{CdS}$  simulations showed that the presence of Zn is detrimental since higher defect densities were detected in growths containing x composition values higher than 0.4 when compared to conventional CdTe on CdS. The exception was the  $\text{Cd}_{0.8}\text{Zn}_{0.2}\text{Te}$  configuration which showed the lowest defect densities from all simulations in this experiment and suggests that a low presence of Zn (x values < 0.2) could in fact help prevent the formation of dislocations in the CdTe epilayer.



The dislocation line densities trend observed in the selective CdTe/CdS simulations indicated that nanoheteroepitaxy was an effective defect reduction strategy when compared to planar CdTe/CdS. The dislocation densities decreased with decreasing island size. These results are in good agreement with the CdTe/CdS island model predicted by nano-heteroepitaxy in subsection 1.2.

The dislocation line densities trend observed in the selective  $\text{Cd}_{(1-x)}\text{Zn}_x\text{Te}/\text{CdS}$  simulations reiterate the observations from the previous strategies; selective-area growth helped decreased the presence of defects but once again higher defect densities were detected in growths containing Zn composition values higher than 0.4 when compared to selective CdTe/CdS. Once again, the exception was the selective  $\text{Cd}_{0.8}\text{Zn}_{0.2}\text{Te}$  configuration which showed the lowest defect densities from all simulations in this study and suggests that a low presence of Zn ( $x$  values  $< 0.2$ ) could in fact help prevent the formation of dislocations in the selective CdTe epilayer. These results are in good agreement with the experimental observations reported in literature [20] [21] [22] where high Zn concentrations degraded film quality suggesting that a similar alloy disordering behavior was captured by the simulations. Future alloying simulations could consider the incorporation of Se (this element is supported by the Stillinger-Webber potential) and switching to CdS (211) zinc blende substrates in order to explore this alloying phenomenon further.

Molecular statics models were developed to understand the effect of the defect reduction strategies evaluated in this work in terms of potential energy difference in the systems. These models included the CdTe/CdS, CdTe/ZnTe/CdS, and  $\text{Cd}_{0.8}\text{Zn}_{0.2}\text{Te}/\text{CdS}$  configurations. The results of these analyses display evidence of the strain relief mechanisms that occur in these three structures and it is observed that these mechanisms are favored by the  $\text{Cd}_{0.8}\text{Zn}_{0.2}\text{Te}/\text{CdS}$  configuration.

## References

- [1] D. Zubia, "Strain partitioning in coherent compliant heterostructures," *Applied Physics Letters*, vol. 80, no. 5, pp. 740-742, 2002.
- [2] C. A. Wolden, J. Kurtin, J. B. Baxter, I. Repins, S. E. Shaheen, J. T. Torvik, A. Rocket, V. A. Fthenakis and E. S. Aydil, "Photovoltaic manufacturing: Present status, future prospects, and research needs," *JVST A – Vac., Surf., Films*, vol. 29, pp. 30801-30816, 2011.
- [3] Z. C. Feng, H. C. Chou, A. Rohatgi, G. K. Lim, A. Wee and K. L. Tan, "Correlations between CdTe/CdS/SnO<sub>2</sub>/glass solar cell performance and the interface surface properties," *J. Appl. Phys.*, vol. 79, no. 1996, pp. 2151-2153, 1996.
- [4] B. E. McCandless and J. R. Sites, "Cadmium telluride solar cells," in *Handbook of Photovoltaic Science and Engineering*, 2nd ed., West Sussex, UK, The Atrium, 2011, pp. 617-672.
- [5] W. K. Metzger, D. Albin, D. Levi, P. Sheldon, X. Li, B. M. Keyes and R. K. Ahrenkiel, "Time-resolved photoluminescence studies of CdTe solar cells," *J. Appl. Phys.*, vol. 94, pp. 3549-3555, 2003.
- [6] J. L. Cruz-Campa and et. al, "Nanopatterning and Bandgap Grading to Reduce Defects in CdTe Solar Cells," *Photovoltaic Specialists Conference (PVSC), 2012 38th IEEE*, pp. 838-842, 2012.
- [7] M. M. Al-Jassim, Y. Yan, H. R. Moutinho, M. J. Romero, R. D. Dhere and K. M. Jones, "TEM, AFM, and cathodoluminescence characterization of CdTe thin film," *Thin Solid Films*, vol. 387, pp. 246-250, 2001.
- [8] J. Moseley, M. M. Al-Jassim, D. Kuciauskas, H. Moutinho, N. Paudel, H. Guthrey, Y. Yan, W. K. Metzger and R. K. Ahrenkiel, "Cathodoluminescence Analysis of Grain Boundaries and Grain Interiors in Thin-Film CdTe," *IEEE Journal of Photovoltaics*, vol. 4, no. 6, pp. 1671-1679, 2014.
- [9] T. Paulauskas, C. Buurma, E. Colegrove, Z. Guo, S. Sivananthan, M. Chan and R. F. Klie, "Atomic-resolution characterization of the effects of CdCl<sub>2</sub> treatment on poly-crystalline CdTe thin films," *Applied Physics Letters*, vol. 105, 2014.
- [10] T. Paulauskas, C. Buurma, E. Colegrove, B. Stafford, Z. Guo, M. Chan, C. Sun, M. J. Kim, S. Sivananthan and R. F. Klie, "Atomic scale study of polar Lomer–Cottrell and Hirth lock dislocation cores in CdTe," *Acta Crystallographica*, vol. 70, pp. 524-531, 2014.
- [11] Y. Yan, K. M. Jones, M. M. Al-Jassim, R. Dhere and X. Wu, "Transmission electron microscopy study of dislocations and interfaces in CdTe solar cells," *Thin Solid Films*, vol. 519, pp. 7168-7172, 2011.
- [12] Y. Yan, M. M. Al-Jassim and K. M. Jones, "Structure and effects of double-positioning twin boundaries in CdTe," *Journal of Applied Physics*, vol. 94, no. 2976, 2003.
- [13] Y. Yan, M. M. Al-Jassim and K. M. Jones, "Characterization of extended defects in polycrystalline CdTe thin films grown by close-spaced sublimation," *Thin Solid Films*, vol. 389, pp. 75-77, 2001.
- [14] Y. Yan and M. M. Al-Jassim, "Energetics and effects of planar defects in CdTe," *Journal of Applied Physics*, vol. 90, no. 8, 2001.

- [15] Y. Yan, K. M. Jones, C. S. Jian, X. Z. Wu, R. Noufi and M. M. Al-Jassim, "Understanding the defect physics in polycrystalline photovoltaic materials," *Physica B*, pp. 25-32, 2007.
- [16] C. Li, J. Poplawsky, Y. Wu, A. R. Lupini, A. Mouti, D. N. Leonard, N. Paudel, K. Jones, W. Yin, M. Al-Jassim, Y. Yan and S. J. Pennycook, "From atomic structure to photovoltaic properties in CdTe solar cells," *Ultramicroscopy*, vol. 134, pp. 113-125, 2013.
- [17] Z. Zhang, A. Chatterjee, C. Grein, A. J. Ciani and P. W. Chung, "Molecular Dynamics Simulation of MBE Growth of CdTe/ZnTe/Si," *Journal of Electronic Materials*, vol. 40, no. 2, pp. 109-120, 2011.
- [18] M. A. Green, K. Emery, Y. Hishikawa, W. Warta and E. D. Dunlop, "Solar cell efficiency tables (Version 45)," *Progress in Photovoltaics: Research and Applications*, vol. 23, pp. 1-9, 2015.
- [19] D. Zubia and S. D. Hersee, "Nanoheteroepitaxy: The Application of nanostructuring and substrate compliance to the heteroepitaxy of mismatched semiconductor materials," *Journal of Applied Physics*, vol. 85, 1999.
- [20] Y. P. Chen, G. Brill and N. K. Dhar, "MBE growth of CdSeTe/Si composite substrate for long-wavelength IR HgCdTe applications," *Journal of Crystal Growth*, vol. 252, pp. 270-274, 2003.
- [21] Y. P. Chen, G. Brill, E. M. Campo, T. Hierl, J. C. Hwang and N. K. Dhar, "Molecular Beam Epitaxial Growth of  $\text{Cd}_{1-y}\text{Zn}_y\text{Se}_{1-x}\text{Te}_x$  on Si(211)," *Journal of Electronic Materials*, vol. 33, no. 6, pp. 498-502, 2004.
- [22] G. Brill, Y. Chen, P. M. Amirtharaj, W. Sarney, D. Chandler-Horowitz and N. K. Dhar, "Molecular Beam Epitaxial Growth and Characterization of Cd-Based II-VI Wide-Bandgap Compounds on Si Substrates," *Journal of Electronic Materials*, vol. 34, no. 5, pp. 655-661, 2005.
- [23] J. E. Sutherland and J. Hauser, "A computer analysis of heterojunction and graded composition solar cells," *IEEE Trans. Elec. Dev.*, vol. 24, pp. 363-372, 1977.
- [24] A. Dhingra and A. Rothwarf, "Computer simulation and modeling of graded bandgap  $\text{CuInSe}_2/\text{CdS}$  based solar cells," *IEEE Trans. Elec. Dev.*, vol. 43, pp. 613-621, 1996.
- [25] A. Morales-Acevedo, "Effective absorption coefficient for graded band-gap semiconductors and the expected photocurrent density in solar cells," *Solar Ener. Mater. Solar Cells*, vol. 2009, pp. 41-44, 2009.
- [26] M. Contreras and et. al, "High efficiency graded bandgap thin-film polycrystalline  $\text{Cu(In,Ga)Se}_2$ -based solar cells," *Solar Energy Materials and Solar Cells*, vol. 41/42, pp. 231-246, 1996.
- [27] A. M. Gabor and et. al, *Proc. 12th NREL P. V. Program Review Meeting*, pp. 13-15, 1993.
- [28] V. L. Dalal, "Designed Considerations for a-Si Solar Cells," *IEEE Transactions on Electronic Devices*, vol. 27, pp. 662-671, 1980.
- [29] F. Anwar, "Numerical Modeling of  $\text{CdS}/\text{Zn}_{1-x}\text{Cd}_x$  Solar Cell," ETD Collection for University of Texas at El Paso. Paper AAI1533205. , El Paso, 2012.  
<http://digitalcommons.utep.edu/dissertations/AAI1533205>.
- [30] W. Cai, J. Li and S. Yip, "Molecular Dynamics," in *Comprehensive Nuclear Materials vol. 1*, Amsterdam, Elsevier, 2012, pp. 249-265.
- [31] D. Marx and J. Hutter, "Ab Initio Molecular Dynamics: Theory and Implementation,"

- Modern Methods and Algorithms of Quantum Chemistry*, vol. 1, pp. 301-449, 2000.
- [32] M. Born and R. Oppenheimer, *Ann. Phys.*, vol. 84, no. 20, pp. 457-484, 1927.
- [33] L. Verlet, *Phys. Rev.*, vol. 159, no. 1, pp. 98-103, 1967.
- [34] X. W. Zhou and et. al., "Stillinger-Weber potential for the II-IV elements Zn-Cd-Hg-S-Se-Te," *Physical Review B*, vol. 88, 2013.
- [35] S. Plimpton, "Fast Parallel Algorithms for Short-Range Molecular Dynamics," *Journal of Computational Physics*, pp. 1-19, 1995.
- [36] S. F. Almeida, E. Ochoa, J. J. Chavez, X. W. Zhou and D. Zubia, "Calculation of surface diffusivity and residence time by molecular dynamics with application to nanoscale selective-area growth," *Accepted for Publication to Journal of Crystal Growth*, 2015.
- [37] W. G. Hoover, "Canonical dynamics: Equilibrium phase-space distributions," *Physical Review A*, vol. 31, no. 3, p. 1695, 1985.
- [38] B. Aguirre and et. al., "Selective Growth of CdTe on Nano-patterned CdS via Close-Space Sublimation," *Journal of Electronic Materials*, 2014.
- [39] A. Stukowski, *Modelling Simil. Mater. Sci. Eng.*, vol. 18, no. 015012, 2012.
- [40] L. Duo, W. FengChao, Y. ZhenYu and Z. YaPu, "How to identify dislocations in molecular dynamics simulations?," *Science China Physics, Mechanics & Astronomy*, vol. 57, no. 12, pp. 2177-2187, 2014.
- [41] A. Stukowski, "Structure identification methods for atomistic simulations of crystalline materials," *Modelling and Simulation in Materials Science and Engineering*, vol. 20, no. 045021, p. 15, 2012.
- [42] A. Stukowski, *Crystal Analysis Tool User's Manual*, Darmstadt. Germany, 2014.
- [43] A. Stukowski, V. V. Bulatov and A. Arsenlis, "Automated identification and indexing of dislocations in crystal interfaces," *Modelling and Simulation in Materials Science and Engineering*, vol. 20, no. 085007, p. 16, 2012.
- [44] J. D. Honeycutt and H. C. Andersen, "Molecular Dynamics Study of Melting and Freezing of Small Lennard-Jones Clusters," *J. Phys. Chem.*, vol. 91, pp. 4950-4963, 1987.
- [45] N. Lummen and T. Kraska, "Common neighbor analysis for binary atomic systems," *Modelling and Simulation in Materials Science and Engineering*, vol. 15, pp. 319-334, 2007.
- [46] T. J. de Lyon, J. A. Roth and O. K. Wu, "Direct molecular-beam epitaxial growth of ZnTe(001) and CdZnTe(100)/ZnTe(100) on Si(100) substrates," *American Institute of Physics*, vol. 63, no. 6, pp. 818-820, 1993.
- [47] D. Hommel, S. Scholl, T. A. Kuhn, W. Ossau, A. Waag and G. Landwehr, "Efficient n-type doping of CdTe epitaxial layers grown by photo-assisted molecular beam epitaxy with the use of chlorine," *Materials Science and Engineering*, vol. 16, pp. 178-181, 1993.
- [48] G. Li, W. Jie, H. Hua and Z. Gu, "Cd<sub>1-x</sub>Zn<sub>x</sub>Te: Growth and Characterization of Crystals for X-ray and Gamma-ray Detectors," *Progress in Crystal Growth and Characterization of Materials*, pp. 85-104, 2003.
- [49] G. Li, X. Zhang, H. Hua and W. Jie, "A Modified Vertical Bridgman Method for Growth of High-Quality Cd<sub>1-x</sub>Zn<sub>x</sub>Te Crystals," *Journal of Electronic Materials*, vol. 34, no. 9, pp. 1215-1224, 2005.

- [50] J. Zhou, X. Wu, G. Teeter, B. To, Y. Yan, R. G. Dhere and T. A. Gessert, "CBD-Cd<sub>1-x</sub> Zn<sub>x</sub> S thin films and their application in CdTe solar cells," *Phys. Stat. Sol. (B)*, vol. 241, no. 3, pp. 775-778, 2004.

## Appendix

### Appendix A: Crystal Analysis Tool Dislocation Models

This appendix describes the structural models employed by the Crystal Analysis Tool to identify and index dislocations from within the atomistic file data. This appendix illustrates schematics of the diamond defect model templates found in the CAT and that were employed in this work for the detection of zinc blende defects. This section also discusses the models developed in this work for the analysis of wurtzite defects, as well as the methodology developed for testing its performance. Finally, Table A.1 and Figure A.6 describes the wurtzite dislocation types found using the developed models.

Figure A.1 illustrates the diamond defect model for a coherent twin and it consists of the blue atoms and their simulation box (solid black outline in the form of a vertical rectangle). The red atoms represent a periodic lattice that facilitate identifying the defect (periodic boundary conditions were used in the two dimensions of this page). The coherent twin in this case consists of three closed-packed plane layers and is enclosed by the dotted black rectangle. The green diagonal lines help to guide the eye towards the AaBbCc... layer stacking characteristic of the diamond lattice along the  $\langle 111 \rangle$ , which in this case is mirrored because of the coherent twin monolayers.

Figure A.2 illustrates the diamond defect model for an intrinsic stacking fault. The intrinsic stacking fault can be described in simple terms as a one closed-packed layer stacking fault. Three intrinsic stacking faults can be observed the figure and are enclosed by the dotted black rectangles. Figure A.3 illustrates the diamond defect model for an extrinsic stacking fault. The extrinsic stacking fault can be described in simple terms as a two closed-packed layers stacking fault. Two extrinsic stacking faults can be observed the figure and are enclosed by the dotted black rectangles. Figure A.4 illustrates the diamond defect model for a triple stacking fault. The triple stacking fault can be described as a three closed-packed layers stacking fault.

One triple stacking fault can be observed in the figure and is enclosed by the dotted black rectangles.

The coherent twin, intrinsic stacking fault, extrinsic stacking fault models for diamond structures depicted in Fig. A.1-3 were used together for the analysis of diamond structure based defects in the results reported in chapter 3.

The creation of hexagonal diamond models exploited the structural similarities between diamond and hexagonal diamond structures and their defects in order to effectively reuse the diamond defect models contained originally within the CAT, and redefine them as hexagonal diamond defects. Within the CAT source, the diamond defect models are defined as being surrounded by perfect diamond crystal lattice atoms. The new hexagonal diamond defect models were defined as being surrounded by hexagonal diamond lattice atoms. This modification created models that effectively detect dislocations inside hexagonal diamond (or wurtzite) atomistic data.

After the hexagonal diamond defect models were created, a series of performance tests were design to determine what combination of defect models would detect the largest number of defects within a set of data.

Fig. A.4 shows top view visualizations of the results obtained for four different analysis configurations. The data set used for these tests is the planar CdTe/CdS growth discussed in subsection 2.2.3. Test 1 included all three of the defect models. Test 2 included only the intrinsic stacking fault model, test 3 the extrinsic stacking fault model, and test 4 the triple stacking fault model. A comparison between the visualizations of test 2 and 3 reveals that these defect models detect the most defects and present almost identical results. This result was confirmed by comparing the quantitative data of the four different tests. The effectiveness of these defect models could be contributed to the few closed-packed layers needed to form each of them in either diamond or hexagonal diamond lattices, making these defect structures the most likely to occur inside a material structure that contains domains of both lattice structures. The intrinsic stacking fault model was the only model used for the hexagonal diamond defect analysis since this defect structure is the simplest defect structure.

Table A.1 lists the most numerous dislocation line types detected in a wurtzite (or hexagonal diamond) based analysis. The notation in this table can be used along with the wurtzite lattice schematic in Fig. A.5 in order to get a clear picture of each dislocation type Burgers vector geometry with respect to the wurtzite lattice structure. In general terms, the dislocation's Burgers vector can be parallel to the closed-packed plane (for example in a Shockley partial) or perpendicular to the closed-packed plane (as is the case for a Frank partial).



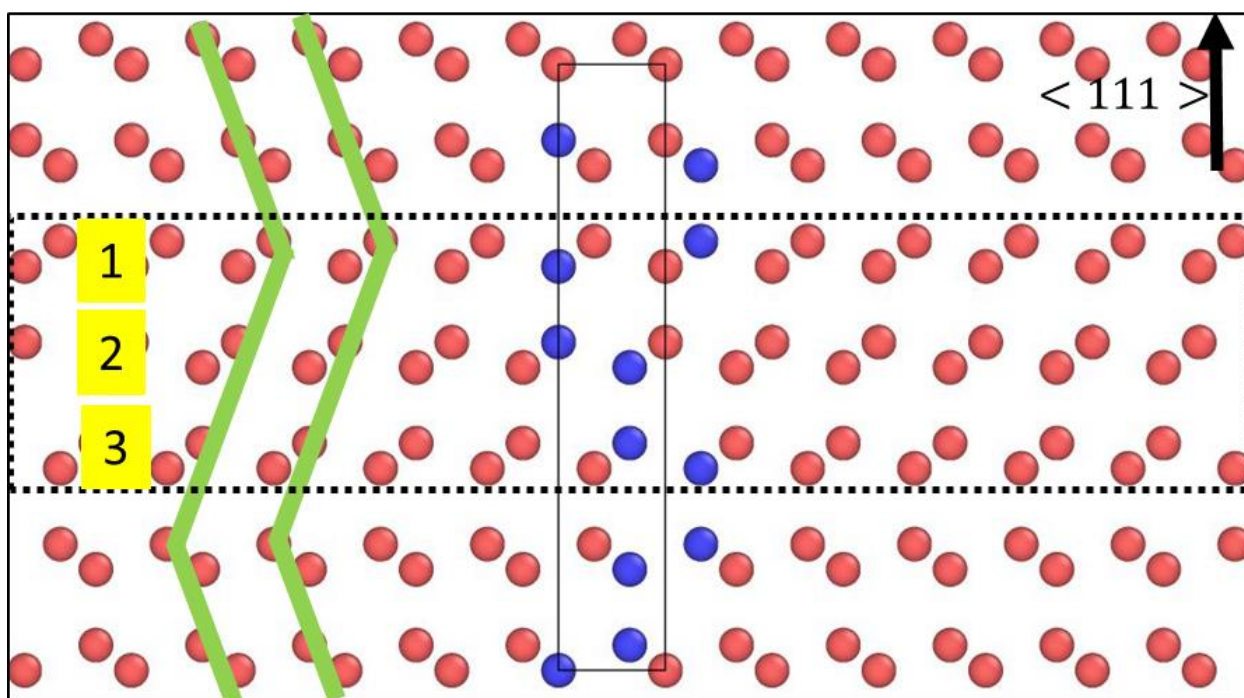


Figure A.1: Atomistic data visualization of a coherent twin model (blue atoms) with periodic images (red atoms) to aid structural identification.

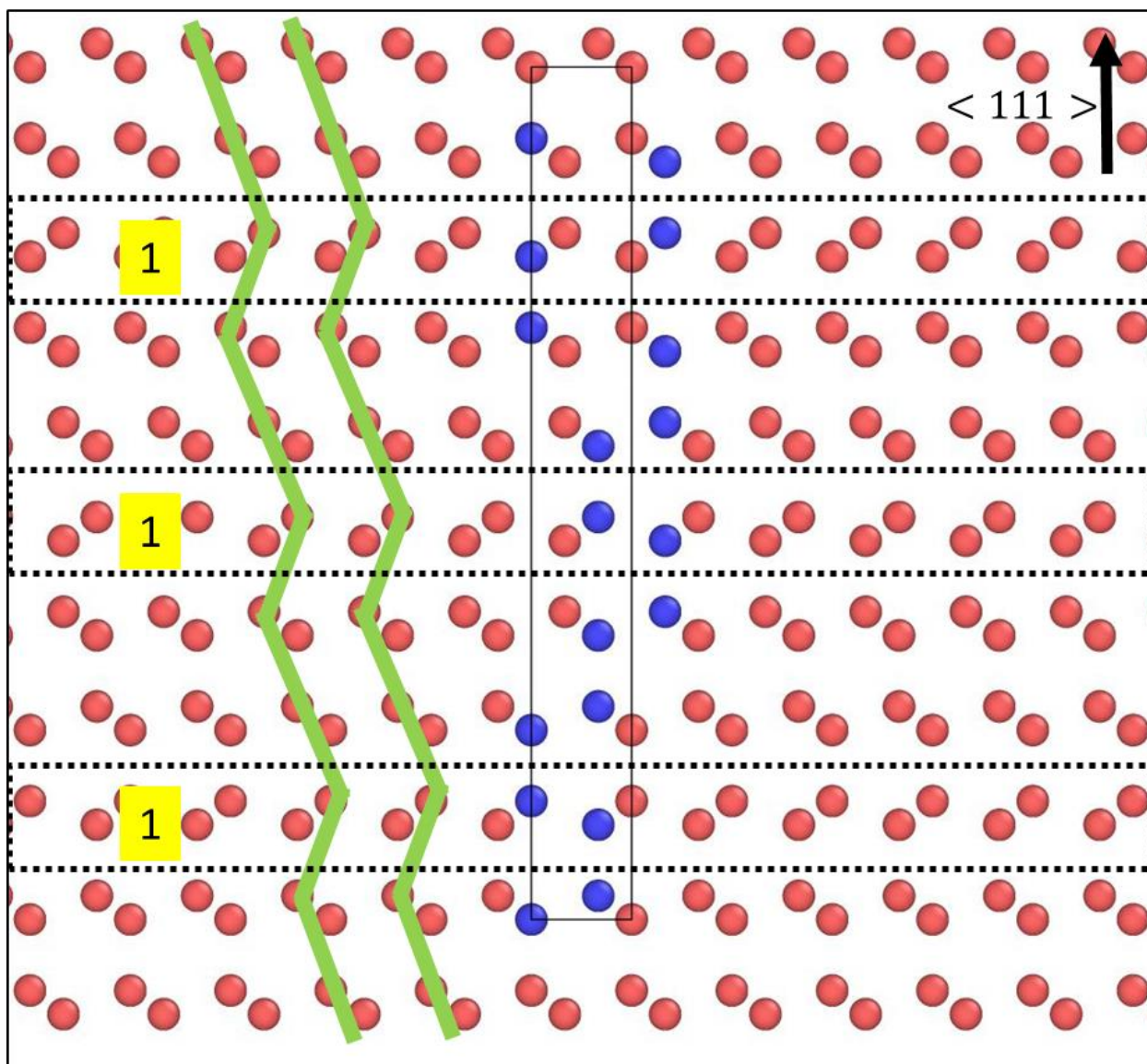


Figure A.2: Atomistic data visualization of an intrinsic stacking fault model (blue atoms) with periodic images (red atoms) to aid structural identification.

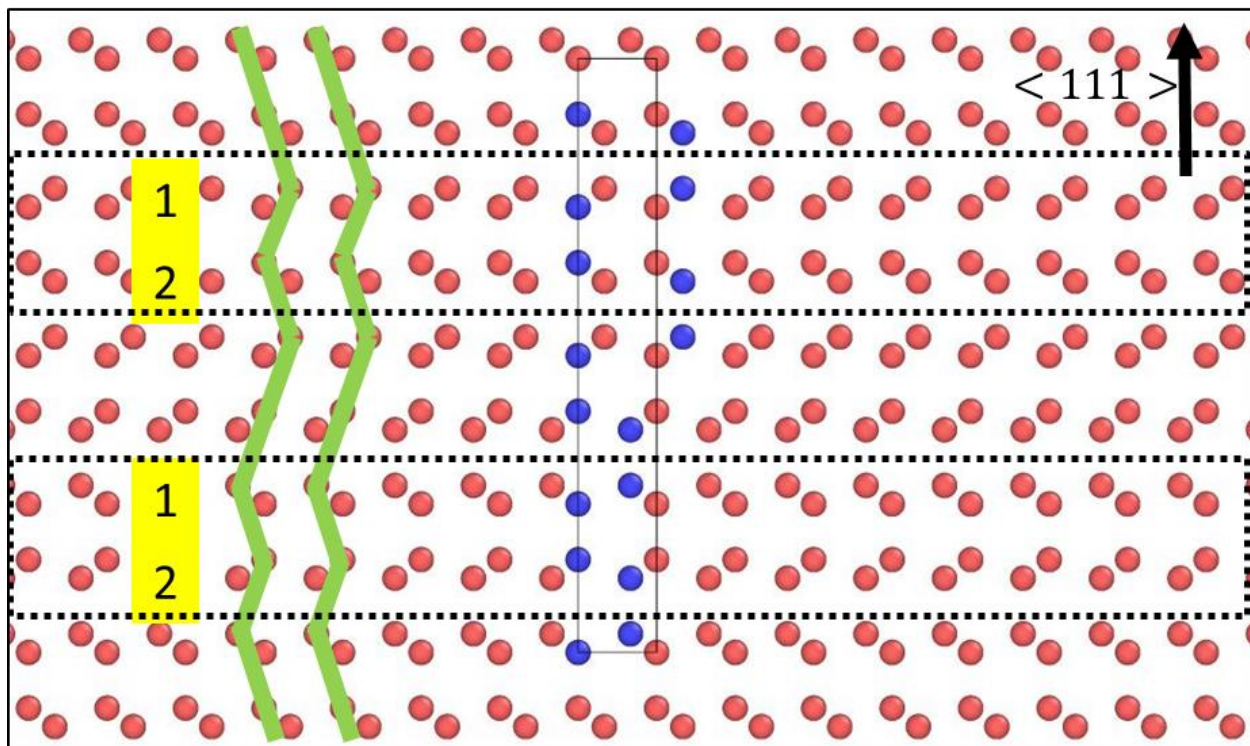


Figure A.3: Atomistic data visualization of an extrinsic stacking fault model (blue atoms) with periodic images (red atoms) to aid structural identification.



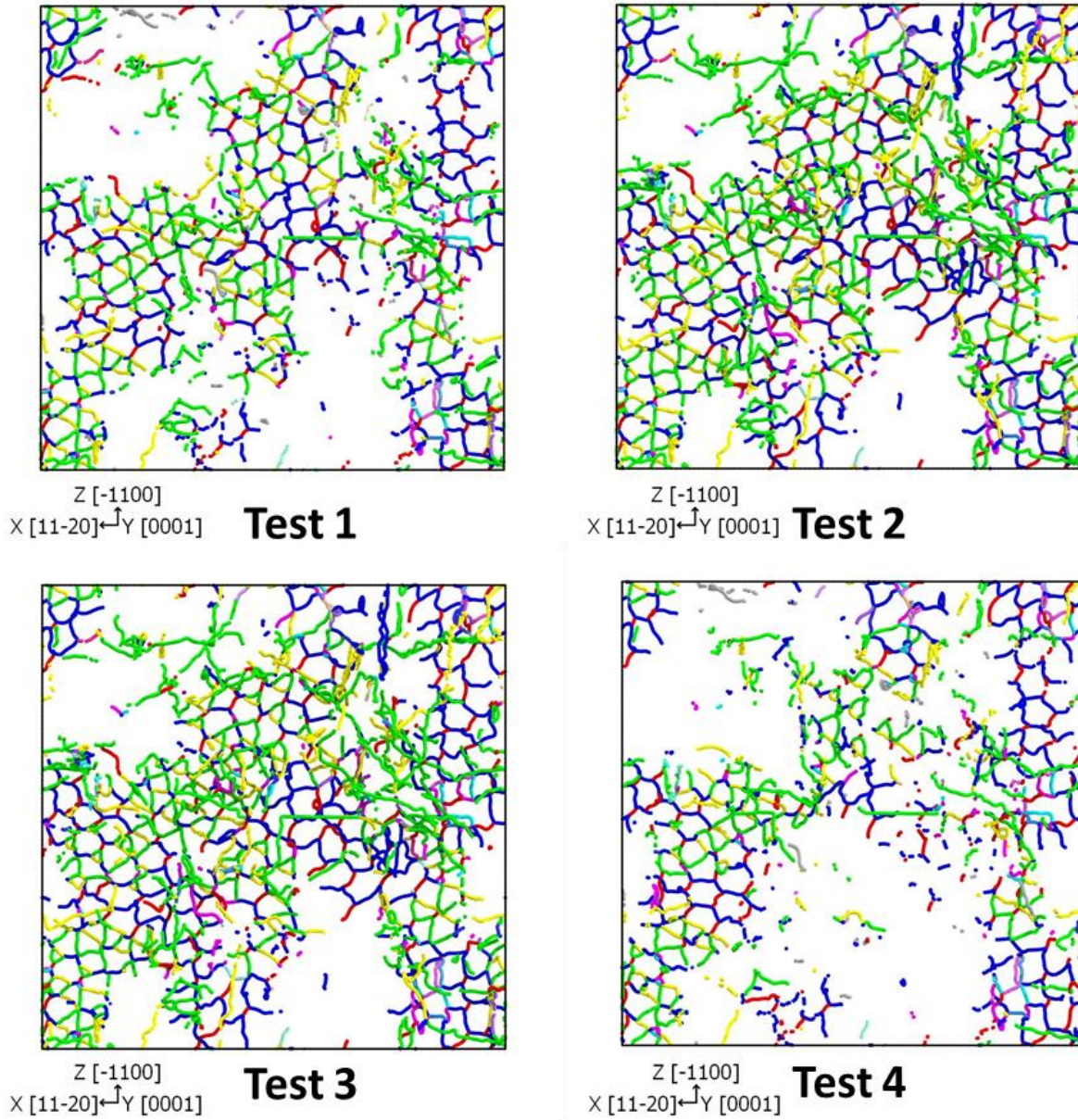


Figure A.4: Dislocation visualization of the results obtained for the four different tests designed to evaluate the performance of four different hexagonal diamond defect detection analysis configurations.

Table A.1: Wurtzite dislocation types detected by the Crystal Analysis Tool. The notation in this table refers to the schematic in Fig. A.6. \*The origin needs to be transferred to the position of  $\zeta$ . \*\*The origin needs to be transferred to the position of F. Points A-G,  $\alpha$ ,  $\beta$ ,  $\zeta$  are lie on the basal plane. Points  $\delta$  and  $\gamma$  lie on a plane above and parallel to the basal plane.

Notation	Wurtzite Burgers Vector Family
$F\alpha^{**}$	$1/3[\bar{1} 1 0 0]$ (Shockley Partial)
GE	$1/3[1 1 \bar{2} 0]$ (Full Dislocation)
$G\beta$	$1/3[0 1 \bar{1} 0]$ (Shockley Partial)
$G\epsilon$	$[0 0 0 1]$ (Full Dislocation)
$\zeta\delta^*$	$1/12[0 0 0 1]$ (Frank Partial)
$F\gamma^{**}$	$1/12[0 0 0 1]$ (Frank Partial)
$F\beta^{**}$	$2/3[\bar{1} 1 0 0]$ (Shockley Partial)



## Appendix B: Common Neighbor Analysis Algorithm

The Common Neighbor Analysis (CNA) is an algorithm that was developed in order to analyze atomistic simulation data and classify it into lattice structures [44]. The algorithm finds the neighbors of an atom within a spherical volume of a radius specified by the user, inside of which the atoms are considered bonded. Atoms found within this radius are known as first shell neighbors. The algorithm computes three values ( $ijk$ ) that describe the bonding topology for the first shell neighbors in order to create a CNA signature that represents a certain lattice structure. Within the CNA signature values,  $i$  is the number of common neighbors,  $j$  is the number of geometrical bonds found within the common neighbors, and  $k$  is the number of bonds in the longest bond chain [44]. The CNA signature for the FCC neighbors is 4-2-1 (for all twelve atoms), while in the case of HCP six neighbors have 4-2-1 and the other six have 4-2-2.

However, the conventional CNA is not adequate for the analysis of diamond and hexagonal diamond structures employed in this work. The reason is that the conventional method works well for finding first shell neighbor information, but diamond and hexagonal diamond structures require an analysis for two neighbor shells. In these two structures, the first shell atoms don't have any common neighbors (0-0-0 signature), therefore the second neighbor shell needs to be analyzed too. In order to address this challenge, Stukowski developed an expansion to the conventional CNA [39] that consists of a two-step process that effectively detects diamond and hexagonal diamond data. This new version of the CNA is included in both the Crystal Analysis Tool and OVITO.

The first step in the modified CNA consists on finding the nearest neighbors for a reference atom. For the diamond and hexagonal diamond structures, the number of first shell neighbor atoms is four. Next, a second analysis is done for each of the first shell neighbors in order to create a list of second shell neighbors. The number of second shell neighbors for these two structures is twelve. Once this is accomplished, the CNA signature of the second shell

neighbors is computed in order to determine what their lattice structure arrangement is. If the second shell neighbors have an FCC arrangement, then the central atom has a diamond lattice structure. If the second shell neighbors have a HCP arrangement the central atom has a hexagonal diamond structure.

The traditional and the modified CNA were developed for monatomic systems, therefore the algorithm doesn't take into account atom types when dealing with systems with two or more elements. A modified CNA for binary systems is available in literature [45], but has not been implemented into the CAT or OVITO yet. Therefore, information such as substitutional defects, dislocation core polarities, etc. can't be detected by using the CNA alone.



## **Curriculum Vita**

Jose J. Chavez earned his Bachelor of Science in Electrical and Computer Engineering degree from The University of Texas at El Paso in May, 2011. In August, 2011 he joined the doctoral program in Electrical and Computer Engineering at UTEP. Following graduation, he will become a post-doctoral researcher at UTEP.

Jose was the recipient of numerous honors and awards including the NSF Bridge to Doctorate Fellowship and the Solar Economy Integrative Graduate Education and Research Traineeship Fellowship. He was also a recipient of the Mexican American Engineering Society's Gran Estudiante Award.

While pursuing his degree, Jose worked as a research associate for the NanoMaterials Integration Laboratory at UTEP. He interned at Sandia National Laboratories in Livermore, CA the summers of 2011, 2012, and 2013.

Jose presented his research at international conference meetings and workshops including the 2014 Proceedings of the IEEE Photovoltaic Specialists Conference held in Denver, CO and the 2014 International High Performance Computing Summer School held in Budapest, Hungary.

Jose's dissertation entitled, "Molecular Dynamics Study on Defect Reduction Strategies towards the Fabrication of High Performance  $\text{Cd}_{1-x}\text{Zn}_x\text{Te/CdS}$  Solar Cells," was supervised by Dr. David Zubia.

Permanent address: 9558 Desert Ridge Dr.  
El Paso, TX 79925